Ph.D. DISSERTATION

Simulation and Mitigation of Screening Current in High-Temperature Superconductor Magnet for Magnetic Resonance Application

자기 공명 응용기기를 위한 고온 초전도 자석의 차폐 전류 해석 및 완화

BY

Jeseok Bang

AUGUST 2022

DEPARTMENT OF ELECTRICAL AND COMPUTER ENGINEERING
COLLEGE OF ENGINEERING
SEOUL NATIONAL UNIVERSITY

Ph.D. DISSERTATION

Simulation and Mitigation of Screening Current in High-Temperature Superconductor Magnet for Magnetic Resonance Application

자기 공명 응용기기를 위한 고온 초전도 자석의 차폐 전류 해석 및 완화

BY

Jeseok Bang

AUGUST 2022

DEPARTMENT OF ELECTRICAL AND COMPUTER ENGINEERING
COLLEGE OF ENGINEERING
SEOUL NATIONAL UNIVERSITY

Simulation and Mitigation of Screening Current in High-Temperature Superconductor Magnet for Magnetic Resonance Application

자기 공명 응용기기를 위한 고온 초전도 자석의
차폐 전류 해석 및 완화

지도교수 한승용
이 논문을 공학박사 학위논문으로 제출함

2022년 8월

서울대학교 대학원

전기 정보 공학부

방제석

방제석의 공학박사 학위 논문을 인준함

2022년 8월

위 원 장: 이 종 호
부위원장: 한 승 용
위 원: 정 현 교
위 원: 김 석 호
위 원: 안 민 철

Abstract

Superconductor magnets hold immense promises for strong magnets based on the fascinating nature that high current can flow with negligible Joule-heating loss dissipation. They have indeed enabled a disruptive technology in high-field and large-power applications. Among the applications, superconductor magnets have played an essential role in nuclear magnetic resonance (NMR) and magnetic resonance imaging (MRI) applications by providing higher magnetic field intensity and uniformity—it is well-known that higher fields created by superconductor magnets can guarantee the higher performance of NMR and MRI applications.

In the past years, low-temperature superconductor (LTS) magnets have played a key role in developing NMR and MRI applications. However, the practical limit of the maximum field intensity of LTS magnets has reached for NMR and MRI. Hence, recently, high-temperature superconductor (HTS) magnets have been positively reviewed to substitute the key role of LTS in magnetic resonance (MR) applications, i.e., NMR and MRI—it is identified that HTS conductors have a superior current-carrying capacity in high fields compared to their LTS counterparts.

Significant challenges in developing HTS magnets for NMR and MRI applications are detrimental effects caused by screening current: e.g., screening current-induced field (SCF) and screening current-induced stress (SCS). Multiple studies of electromagnetic and mechanical failures of high field HTS magnets due to screening current have been reported. SCF degrades the magnetic performances of an HTS magnet in terms of spatial magnetic field uniformity and temporal magnetic field stability. SCS degrades mechanical stability in the magnet operation. Accordingly, an in-depth understanding of screening current with numerical simulation and a practical technique to mitigate screening current and its consequential effects are urgently required in the HTS magnet discipline.

In this thesis, I thus aim to resolve selected screening current issues of detrimental effects on HTS magnets for MR applications. The lack of numerical simulation methods to explain screening current and the lack of practical techniques to mitigate screening current are defined as problems of the current HTS magnet technology. Then, two solutions are provided in the two aspects of numerical simulation and practical technique; each solution is demonstrated with experimental studies. The detailed descriptions for the two solutions are as follows.

Numerical simulation methods are studied to elucidate screening current and its consequential effects. As a result, multiple simulation methods are developed to explain screening current-induced effects: e.g., non-uniform current density, nonlinear inductive voltage behaviors, spatial and temporal magnetic field behaviors, and excessive mechanical stress distribution. Then, numerical studies of HTS NMR magnets analysis are performed to demonstrate the validity of the proposed simulation methods for describing screening current and its detrimental effects. In this study, 3 T and 9.4 T all-HTS magnets for NMR applications are adopted. Calculation results from nonlinear numerical simulation are compared to measured ones in terms of voltages, spatial magnetic fields, spatial field uniformity, temporal field stability, and mechanical stability in the magnet operation. Good agreements between calculation and measurement results are confirmed. Conclusively, comparison results suggest that the use of proposed numerical simulation methods may be valid in describing nonlinear electromagnetic behaviors induced by screening current in an HTS magnet.

A customized electric heater named “Thermal Eraser” is discussed as a practical solution to mitigate detrimental effects caused by screening current. The key concept of Thermal Eraser is the optimal temperature control to degrade spatially distributed critical current. In detail, the mitigation mechanism is implemented by the nature of screening current depending on the critical current’s magnitude. Here, Thermal Eraser intentionally lowers the magnitude of critical currents of individual windings in an

HTS coil by the optimal temperature control. A superconducting module, including an HTS coil and a Thermal Eraser, is designed, constructed, and tested in a conduction cooling facility. With this experimental study, SCF reduction is captured due to activation of the Thermal Eraser, which implies screening current is mitigated. The test results validate the feasibility of using the Thermal Eraser in mitigating screening current. A post-experiment analysis is performed with the numerical analysis methods. As a result, good agreements between calculation and measurement results are confirmed in terms of temperature gradient and SCF reduction.

In conclusion, this thesis defines issues of HTS magnet, which is a promising alternative to LTS magnet for NMR and MRI, and provides solutions in the aspect of numerical simulation methods and a practical mitigation technique. Numerical and experimental studies confirm the validity of the solutions. The key contributions of this thesis are summarized as follows. First, numerical simulation methods are proposed and demonstrated to "precisely" describe screening current, and they can address the selected screening current issues in a numerical way. Second, Thermal Eraser is proposed and demonstrated to "substantially" mitigate screening current in an HTS coil, and it can address the issues in a practical way. With the solutions, screening current issues caused by the lack of numerical simulation methods and practical techniques could be resolved. Therefore, I believe this thesis would pave the way to explore higher field intensity and uniformity. Finally, I hope this thesis opens a new horizon of high field HTS magnets for the next-generation NMR and MRI applications.

keywords: Finite element method, HTS magnet, MR application, numerical simulation, optimal temperature control, screening current

student number: 2017-26332

Contents

List of Tables

List of Figures

Nomenclature

$\bar{M}$	Magnetization quantity [T]
Δ	Energy gap to break Cooper pair [J]
$\epsilon_{i\in\{r,\theta,z\}}$	Mechanical strain [%]
γ	Gyro-magnetic ratio of magnetic resonance [MHz/T]
λ_i	Self coupled magnetic flux linkage of i^{th} conductor [Wb]
λ_L	London penetration depth [m]
μ	Permeability [H/m]
μ_0	Vacuum permeability [H/m]
ν	Radio frequency of magnetic resonance or Larmor frequency [Hz]
$\nu_{ij\in\{r,\theta,z\}}$	Poisson's ratio
Φ	Electric potential [V]
Φ_0	Quantum of magnetic flux [Wb]
ϕ_{ij}	Mutually coupled magnetic flux linkage between i^{th} and j^{th} conductors [Wb]
ρ	Electric resistivity [Ωm]
σ	Mechanical stress [N/m^2]

$\tau_{ij\in\{r,\theta,z\}}$ Shear stress [N/m^2]

B Magnetic flux density vector [T]

H Magnetic field vector [A/m]

J Current density vector [A/m^2]

M Magnetization vector [T]

W Vector shape function for edge element

T_1 Time constant of T1 process, spin-lattice relaxation time [s]

T_2 Time constant of T2 process [s]

ξ Coherence length [m]

B Magnetic flux density quantity [T]

B_0 Applied direct current magnetic field intensity to MR sample [T]

B_c Critical magnetic flux density [T]

E Electric field quantity [V/m]

E_m Magnetic stored energy [J]

$E_{i\in\{r,\theta,z\}}$ Young's modulus [GPa]

G Gibbs free energy [J]

G_n Gibbs free energy per volume of the normal state [J/m^3]

G_s Gibbs free energy per volume of the superconducting state [J/m^3]

G_x Gradient field intensity for MRI along x-axis [T/m]

G_y Gradient field intensity for MRI along y-axis [T/m]

G_z Gradient field intensity for MRI along z-axis [T/m]

$G_{ij\in\{r,\theta,z\}}$ Shear modulus [N/m^2]

H Magnetic field quantity [A/m]

H_a Applied magnetic field [A/m]

H_e External magnetic field [A/m]

H_p Full penetration magnetic field [A/m]

I Current quantity [A]

J Current density quantity [A/m^2]

J_c Critical current density [A/m^2]

J_{sc} Screening current density [A/m^2]

J_T Characteristic current scale set by thermal fluctuations [A/m^2]

J_t Transport current density [A/m^2]

L_i Self inductance of i$^{\text{th}}$ conductor [H]

m Magnetic moment [Am^2]

M_0 Net magnetization at equilibrium state [T]

M_z Longitudinal magnetization [T]

$M_{i,j}$ Mutual inductance between i$^{\text{th}}$ and j$^{\text{th}}$ conductors [H]

M_{xy} Transverse magnetization [T]

n Index number for the power law model of HTS

R Resistance [Ω]

R_{ct} Contact resistivity [Ωcm^2]

R_c Characteristic resistance [Ω]

R_{sc} Intrinsic resistance of superconductor [Ω]

$s(t_x, t_y)$ MR signal in time domain

S Entropy [J/K]

T Temperature [K]

T_c Critical temperature of superconductor [K]

T_g Vortex-glass critical temperature [K]

t_x Time duration for x-gradient coil operation [s]

t_y Time duration for y-gradient coil operation [s]

U Internal energy [J]

u Mechanical displacement [m]

V Volume [m^3]

Z_i The i$^{\text{th}}$ order zonal harmonic coefficient [T/m^i]

Chapter 1

Introduction

Over the last 100 years, low-temperature superconductor (LTS) magnet technology has prevailed in high-field and large power applications. Especially for magnetic resonance (MR) applications, i.e., nuclear magnetic resonance (NMR) and magnetic resonance imaging (MRI) applications, LTS magnet technology has produced tremendous achievements. As a result, LTS magnet technology has established itself as a standard technology for NMR and MRI main magnets.

Meanwhile, during the revolutions in NMR and MRI based on LTS magnet technology, an innovative technology, i.e., high-temperature superconductor (HTS) magnet technology, emerged. It has been widely agreed that HTS magnet technology has strong potential to lead to a new paradigm toward high field based on the superior current-carrying capacity compared to its LTS counterparts. However, HTS magnet technology has been hindered in penetrating NMR and MRI market mainly due to their inferior operation reliability and stability.

Revolutions in HTS magnet technology were initiated by a simple idea of eliminating the insulation layer of HTS wire, the so-called no-insulation (NI) winding technique. It indeed provoked prodigious ripple effects. As a result, it is now expected that HTS magnet technology can pave the way for high field and large power applications in situations where the practical limit of the performance of LTS magnets is identified.

This chapter thus reviews the historical overview of superconductor magnets, including LTS and HTS, for high magnetic fields. Next, it emphasizes the necessity of HTS magnet for MR applications. Then, recent issues of high field HTS magnet technology are discussed. The main topic of the issues is the intrinsic induced current of superconductor, i.e., screening current, that can cause detrimental effects on the magnetic performance of an HTS magnet for NMR and MRI applications.

1.1 Research Motivation

1.1.1 High field HTS magnet for the next generation NMR and MRI

Referring to the historical overview of NMR and MRI applications provided in Figure 1.1, the high magnetic field intensity is indeed a fascinating option in developing high-performance NMR and MRI applications [1–4]. This is based on the nature that

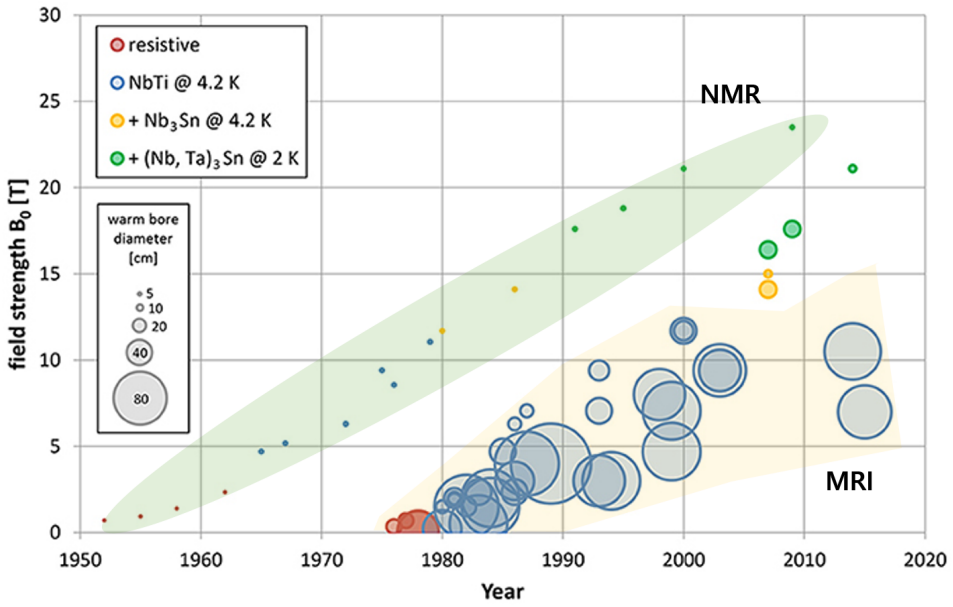

Figure 1.1: Historical overview of NMR and MRI applications development.

higher magnetic field intensity and uniformity in a target space for an MR sample can improve NMR and MRI performance. The fundamental principle is that the signal-to-noise ratio (SNR) is ameliorated as the field intensity increases; the field intensity improves the so-called resolution of MR signals. The SNR depending on the applied direct current magnetic field intensity (B_a) to an MR sample can be described with (1.1) for the NMR case and (1.2) for the MRI case [1]:

$$\mathrm{SNR}_{\mathrm{NMR}} \propto \sqrt{B_a^3}, \tag{1.1}$$

$$\mathrm{SNR}_{\mathrm{MRI}} \propto \frac{B_a^2}{\sqrt{\alpha B_a^{1/2} + \beta B_a^2}}. \tag{1.2}$$

The promising potential of high magnetic fields for NMR and MRI has been indeed demonstrated with experimental studies, as shown in Figures 1.2–1.3. For the NMR case, it is possible to analyze the structure of compounds with the use of 1200 MHz (corresponding to 28 T) NMR more precisely than with 500 MHz (corresponding to 12 T) NMR as providing far better resolution [5]. For the MRI case, as the field intensity increases, it becomes possible to capture even smaller tissues [6].

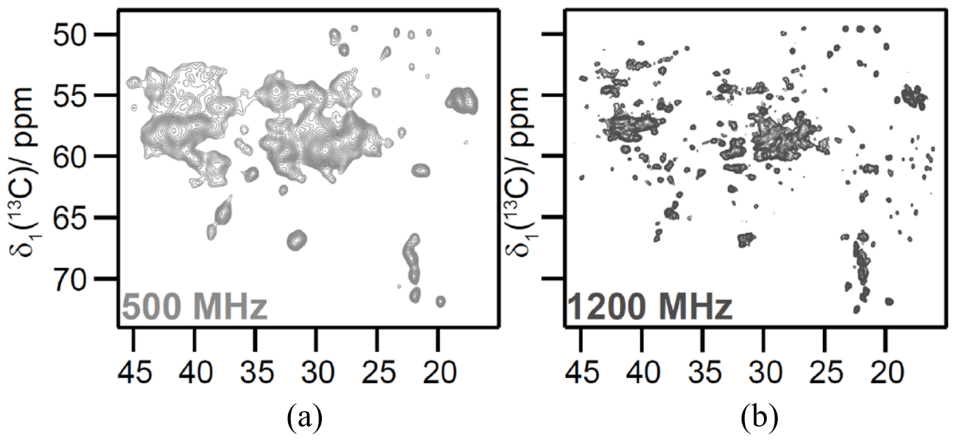

Figure 1.2: Comparison between NMR signals: (a) 500 MHz NMR (corresponding to 12 T) and (b) 1200 MHz (corresponding to 28 T).

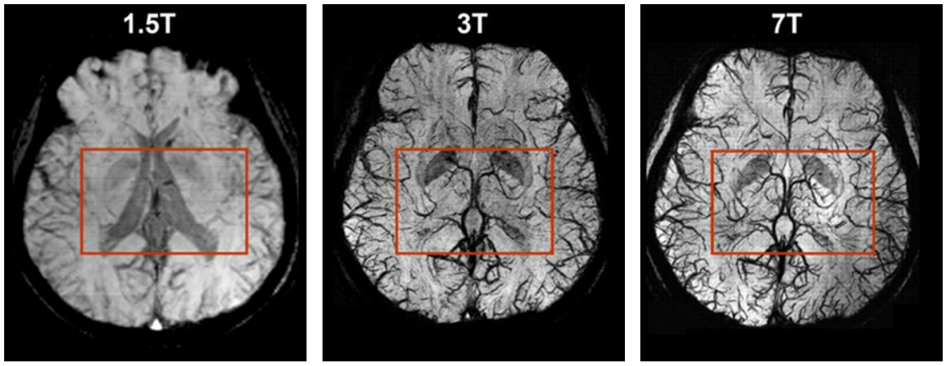

(a) (b) (c)

Figure 1.3: MR images depending on the field intensity: (a) 1.5 T; (b) 3 T; and (c) 7 T.

In the early stage, NMR and MRI applications were developed using permanent magnets and electromagnets (normal conductor based). However, their practical limit in the magnetic field strength was confirmed as 3 T for NMR and 0.2 T for MRI. Hence, LTS magnets were adopted as alternatives to them. Numerous research and development endeavors of using LTS magnets for NMR and MRI applications have been made. As a result, LTS magnets have brought several breakthroughs in the NMR and MRI applications by providing higher magnetic field intensity and stability.

Cutting-edge superconductor magnets for NMR and MRI applications are indeed remarkable. For NMR, a 22 T LTS magnet and a 26 T LTS/HTS hybrid magnet for the advanced GHz-level NMR applications have been reported. For MRI, a 7 T LTS magnet for clinical routine and an 11.7 T LTS magnet only for research have been reported. One thing to note here is that the magnetic performance of LTS magnets for NMR and MRI in terms of the field strength has reached its practical limit; for instance, $\sim$25 T for NMR and $\sim$12 T for MRI. Figure 1.4 may support the argument. It provides the comparison results of the current carrying capacity, also known as critical current (I_c), between LTS and HTS wires in high fields [7]. As shown in Figure 1.4, HTS shows imcomparable high I_c performance to LTS in high fields. Therefore, NMR and MRI manufacturers have reviewed the use of HTS magnet technology to create

higher fields compared to its LTS counterparts. As a result, they conclude that the utilization of HTS magnet is a promising option for the next generation NMR and MRI applications. Meanwhile, it is assessed that the practical limit of the main magnet with high field HTS magnet technology for NMR applications would be over 40 T, as shown in Figure 1.5 [8].

Recent progress in HTS magnet technology is remarkable. Based on the improvement of thermal stability and operation reliability by the NI HTS winding technique, HTS magnet technology has laid the foundation for exploring a high field realm. The achievement of a record-high 45.5 T using an HTS magnet [9], Figure 1.6(a), is indeed a milestone that shows the strong potential of HTS for the next-generation high field applications. The additional achievements of high magnetic fields beyond 30 T may be supplemental clues to sustain the argument, shown in Figures 1.6(b)–(d): a 32 T all

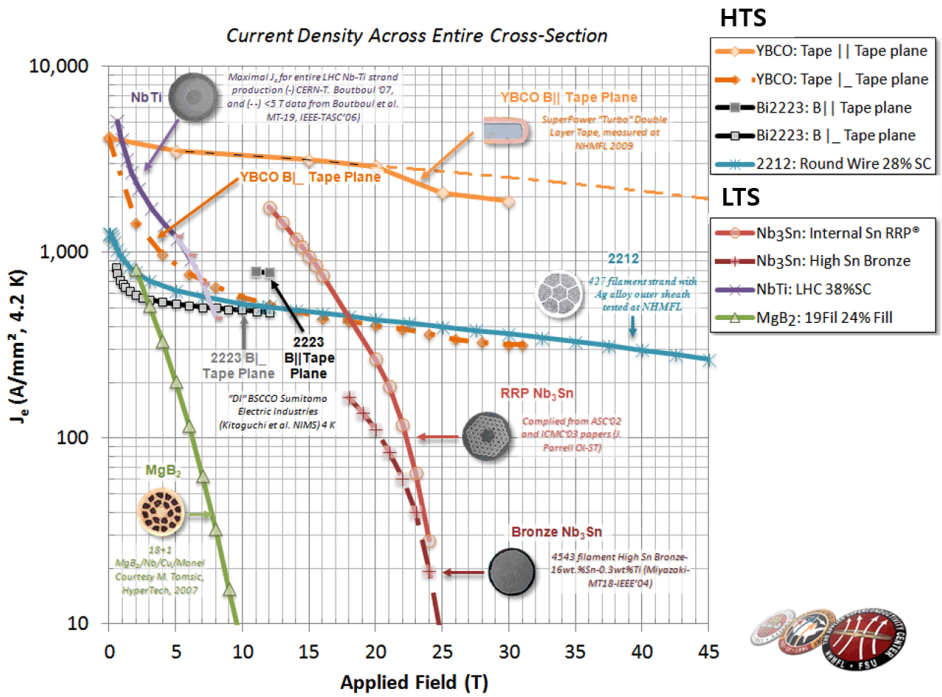

Figure 1.4: I_c performance of superconductors.

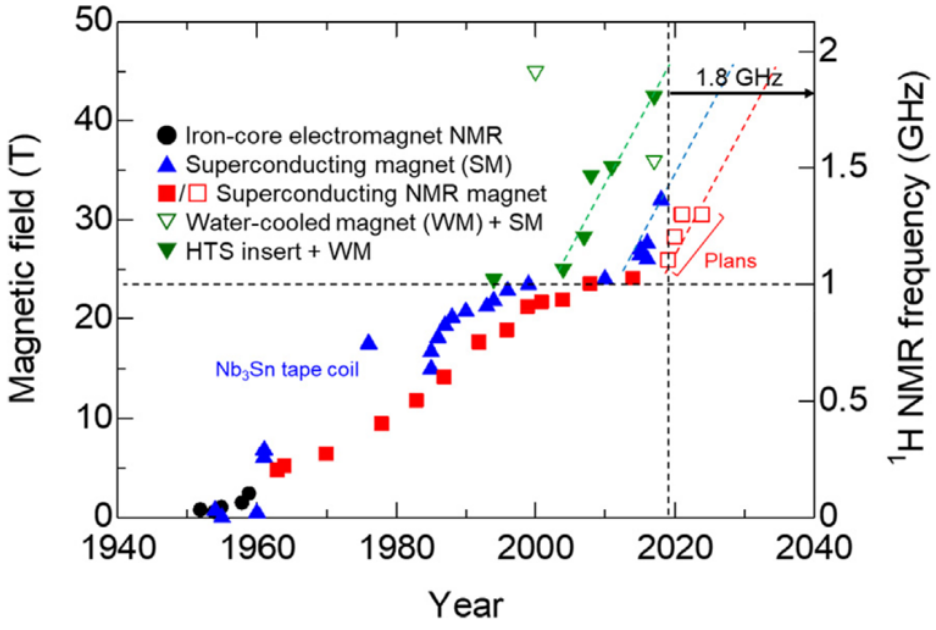

Figure 1.5: Historical overview and the expectation of NMR magnet.

superconductor (LTS and HTS) "user" magnet developed by National High Magnetic Field Laboratory (NHMFL); a 32.4 T all superconductor (LTS and HTS) magnet developed by Chinese Academy of Sciences (CAS); a 32.5 T hybrid (HTS and resistive) magnet developed by the HTS team at Laboratoire National des Champs Magnétiques Intenses [10–12].

These days, the HTS magnet has rapidly broadened into many fields based on better magnetic performance compared to its LTS counterparts. Many researchers have performed the feasibility study of using an HTS magnet to demonstrate its potential: medicine (magnetic resonance imaging, MRI), pharmacy (nuclear magnetic resonance, NMR), particle accelerators (such as the Large Hadron Collider), high energy physics (for example, axion detector), fusion devices (for example, the Soonest/Smallest Private-Funded Affordable Robust Compact, SPARC), and other diverse scientific as well as industrial uses [13–43], Figure 1.7.

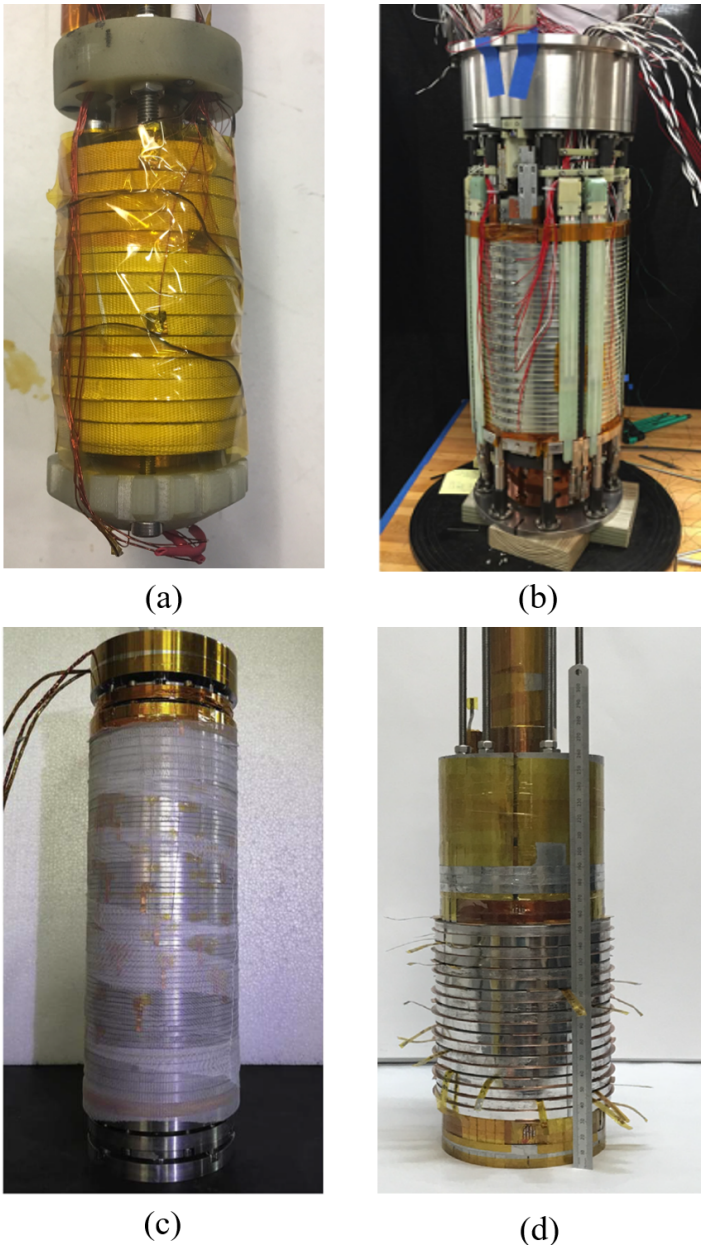

Figure 1.6: Ultra-high field magnets. (a) the HTS insert magnet of the record-high 45.5 T magnet; (b) a 32 T all-superconducting “user” magnet; (c) a 32.4 T all superconductor magnet; and (d) the HTS magnet of the 32.5 T hybrid magnet

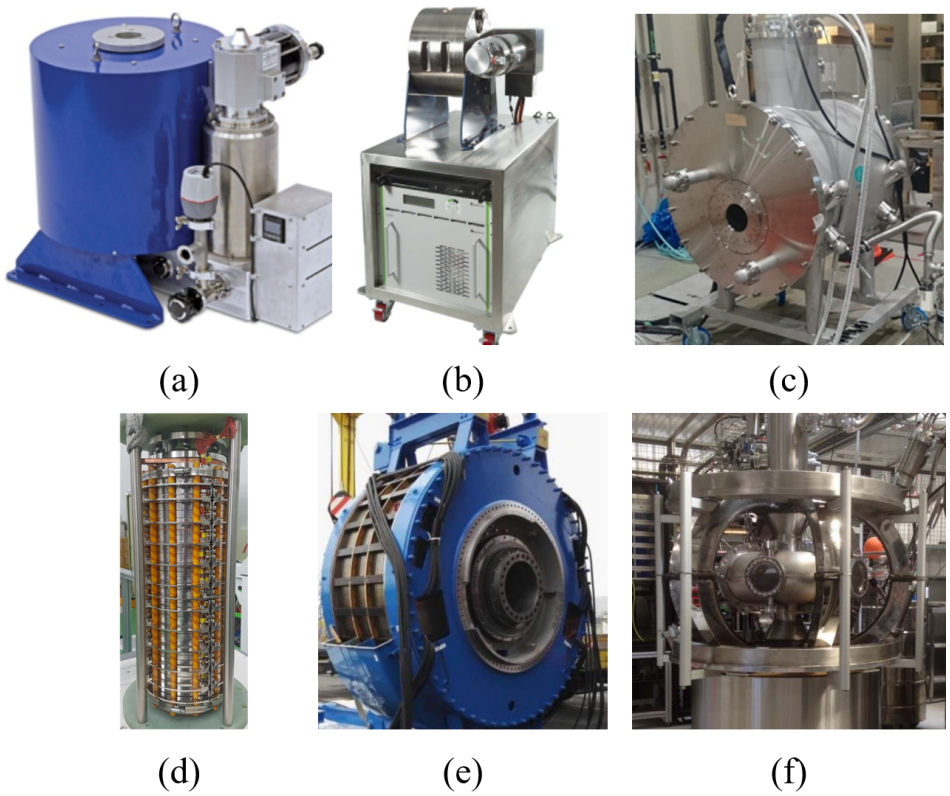

Figure 1.7: Remarkable achievements of HTS magnet: (a) a high field shielded NMR magnet; (b) a 3 T metrology magnet; (c) a 3 T magnet for MRI; (d) a 18 T axion detector magnet; (e) a magnet for wind power generator; and (f) a tokamak for fusion.

1.1.2 Key issues of high field HTS magnet: screening current

Screening current is an intrinsic current in superconductors induced to expel penetrating magnetic flux. Although screening current is induced in both LTS and HTS magnets, LTS magnets wound with multi-filament LTS wires endure marginal screening current-induced effects, while an HTS magnet wound with coated conductor type single filament wire experiences substantially larger screening current-induced effects.

Two issues on HTS magnet have been raised. Note that screening current can jeopardize the magnetic performance of an HTS magnet: screening current-induced field (SCF) and screening current-induced stress (SCS). SCF degrades the magnetic performance of an HTS magnet, e.g., the maximum field strength and the field uniformity at the magnet center. SCS causes mechanical damage on HTS tapes due to excessive mechanical stress and consequently limits the magnetic performance.

SCF causes so-called field error which is the difference between measured magnetic fields and designed ones. Accordingly, SCF issues become prominent in an HTS magnet for MR applications since they essentially require high field uniformity in MR samples. It is considered that an in-depth study on SCF at the HTS NMR magnet level has initiated by Hahn *et al.* [44] and Ahn *et al.* [45], as shown in Figure 1.8. They identified spatial and temporal SCF behaviors and their detrimental effects on NMR signals. Starting with the pioneering research, screening current of HTS and some detrimental effects of SCF on the magnetic performance of an HTS magnet have been actively studied. As a result, it has been confirmed that SCF can degrade three types of magnetic performances: the intensity of magnetic fields, the uniformity of spatial magnetic fields, and the stability of temporal magnetic fields. The second one may be the key challenge in developing an HTS magnet for MR applications; higher field uniformity is desirable for NMR and MRI to preserve better SNR of MR signals. The recent report on the HTS magnet technology for a GHz-level NMR application may support this argument. Hence, the magnetic performance degradation due to SCF is still one of the main concerns in developing HTS magnets for MR applications, Figure 1.9 [5].

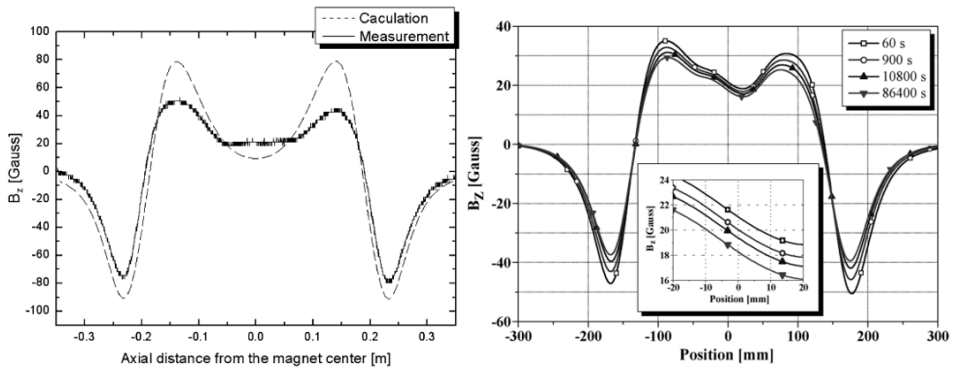

(a) (b)

Figure 1.8: (a) Comparison results between calculation and measurement of SCF. (b) Temporal behavior of SCF.

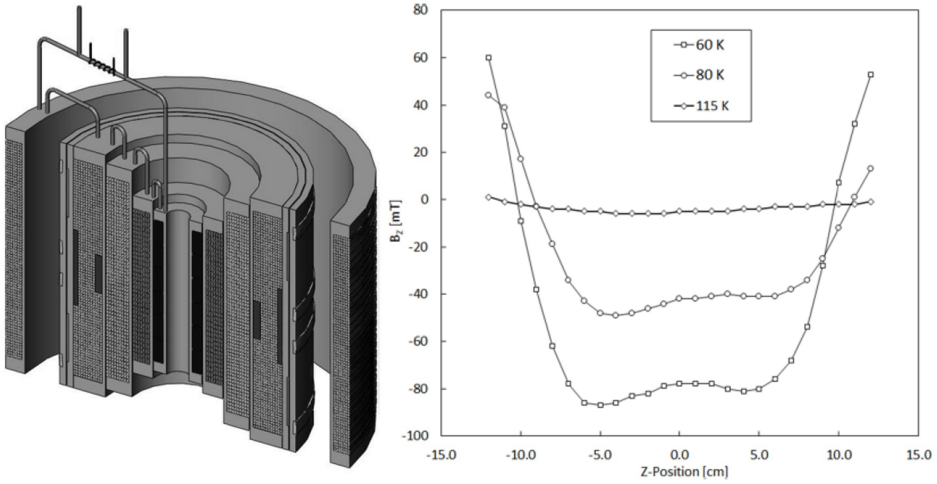

(a) (b)

Figure 1.9: (a) Commercial GHz-class NMR main magnet consisting of LTS and HTS magnets. (b) Magnetic field profile along the z-axis measured of the main magnet.

Meanwhile, the detrimental effect of SCS was firstly reported from an HTS insert magnet named 'Little Big Coil (LBC)' of the record-high direct-current 45.5 T high-temperature superconducting magnet. From the post-mortem analysis of unwinding all the HTS module coils in the magnet, the mechanical damage of wavy plastic deformation on HTS tapes was discovered (see Figure 1.10). The collaborative team developing the 45.5 T direct-current magnet led by National High Magnetic Field Laboratory concluded that SCS induced excessive mechanical stress concentration at the edge of HTS windings and consequently caused plastic deformation; the team suggested that excessive mechanical stress larger than 1 GPa was induced at edges of HTS module coils and it consequently caused plastic deformation. This conclusion has inspired multiple research groups and provoked them to perform numerous studies on SCS, as shown in Figure 1.11 [46,47]. The excessive mechanical stress distribution in a test coil exposed to a high field has been mainly studied. As a result, they have substantiated that HTS magnets can not create higher magnet fields due to the mechanical stress limit of HTS wires even if the current-carrying capacity of HTS tape in high fields is not reached up to its maximum value.

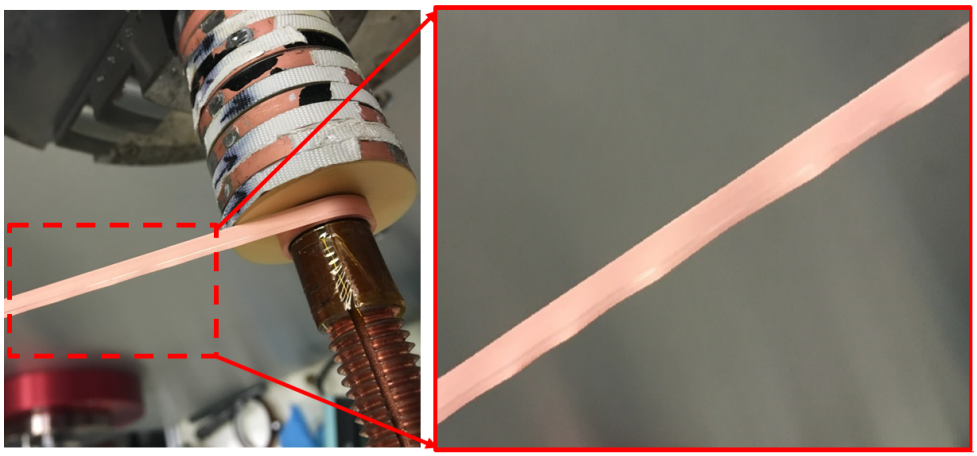

Figure 1.10: Post-mortem analysis result of the wavy plastic deformation discovered from an HTS insert magnet of the record-high 45.5 T magnet.

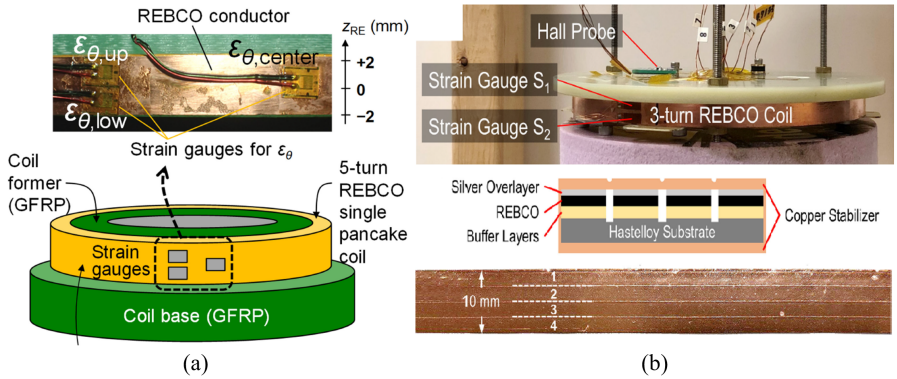

Figure 1.11: Experimental studies of SCS at the test coil level performed by (a) RIKEN in Japan and (b) Massachusetts Institute of Technology in USA.

1.2 Research Object

Fundamental studies have been performed by numerous researchers to simulate and mitigate detrimental effects caused by screening current. They have investigated electromagnetic behaviors induced by screening current and consequently developed numerical simulation models to describe the behaviors. The first trial was performed with an integral equation for a thin conductor. Brambilla *et al.* proposed a model calculating current density and field distribution in a superconducting thin conductor, e.g., HTS coated conductor, where electromagnetic constitutive law for the resistivity of superconductor is described with the so-called power-law $E - J$ model [48–50]. The fundamental research extended to analyzing the current distribution and AC loss in superconducting cable, coated conductor stacks, and coils—the well-known finite element method simulation with the H formulation of Maxwell's equation was frequently used. Furthermore, researchers have made a lot of endeavors to develop the finite element method-based highly nonlinear electromagnetic simulation. As a result, various numerical simulation models have been proposed to describe non-uniform current density due to screening current and the consequential effects: e.g., H–φ formulation, A–V formulation, and T–A formulation methods [51–64].

Numerical simulation for HTS have paved the way in elucidating electromagnetic behaviors induced by screening current [65–78]. However, the applicability has been "partially" demonstrated since studies have been widely performed that compare calculation results from each simulation model rather than experimental results. Especially, spatial magnetic fields and module coil voltages considering screening current have been insufficiently studied so far. Meanwhile, experimental studies on practical techniques to mitigate detrimental effects caused by screening current have been performed. As a result, multiple mitigation techniques have been proposed [79–83]. Among the techniques, the well-known current sweep reversal (CSR) technique [79] is applied to operate the HTS magnet, while other techniques are not currently used due to limitations in their feasibility and practicability—CSR is a current control technique charging an HTS magnet with an operating current larger than the target current and then discharging an HTS magnet current to the target current. It implies that practical techniques to mitigate screening current in an HTS magnet are insufficient.

This paper intends to supplement the lack of demonstration in terms of comparing simulation and experiment results at the HTS magnet level. In addition, it discusses the use of a customized electric heater to supplement the lack of practical techniques in mitigating detrimental effects caused by screening current. Ultimately, this thesis, therefore, aims to address the screening current issues of an HTS magnet by studying numerical simulation methods and a practical technique to mitigate detrimental effects induced by screening current. The details are provided below.

1.2.1 Review of fundamental superconductivity and MR physics

MR applications require high field intensity and uniformity. Accordingly, HTS magnets for NMR and MRI need to fulfill the requirements. However, screening current of HTS may hinder an HTS magnet from generating high field intensity and uniformity. To address the relevant issue, the nature of screening current in HTS magnet is studied as the first step of this thesis. The fundamental physics of superconductivity

is reviewed. Because screening current induction depends on the magnitude of critical current density, the primary theories are studied to investigate critical current of superconductors. Then, the screening current induction mechanism is scrutinized by Bean's theory assuming an ideal superconductor. Second, MR physics is studied in terms of why high field intensity and uniformity are desirable for MR applications.

1.2.2 Numerical methods to simulate screening current

The lack of in-depth understanding of non-uniform current density in an HTS magnet due to screening current has become a significant issue in the design and operation of HTS magnets. This thesis thus studies numerical simulation methods for screening current analysis. First, a current density simulation based on the finite element method is studied. This simulation method is utilized to obtain non-uniform current density, including transport current and screening current. Then, additional simulation methods are studied to describe nonlinear electromagnetic behaviors. Here I aim to analyze measurable electromagnetic quantities: for instance, coil terminal voltages, spatial magnetic field uniformity, and temporal magnetic field stability. In addition, a mechanical stress analysis method, including SCS, is studied. The method can be used to qualitatively estimate the magnet operation reliability and stability.

The nonlinear numerical simulation methods are validated with comparative studies. A 9.4 T 100 mm all HTS magnet for a 400 MHz NMR application and its demonstration 3 T magnet are adopted for the validation. Nonlinear numerical analysis of the given HTS NMR magnets is performed. The simulation results are compared to measurement ones in terms of coil voltages, spatial magnetic field uniformity, temporal magnetic field stability, and mechanical reliability. The significance of this study is that the discrepancy of magnetic fields between the design and measurement results may be reduced with numerical simulation methods. So far, the effects of screening current have not been considered in the design stage of an HTS magnet for NMR and MRI applications. As a result, a significant discrepancy has been widely reported

in terms of field uniformity and field mapping results. Although the discrepancy can be alleviated by using various magnetic field compensation techniques, i.e., passive and active shimming techniques, their usage may be limited when the discrepancy increases as the field intensity created by an HTS magnet increases. It implies that the nonlinear numerical analysis methods of screening current would be essential for the "integrated" design, considering screening current and SCF effects on field uniformity. Ultimately, it is believed that the analysis methods would be used to design an HTS magnet for the next generation NMR and MRI applications.

1.2.3 Optimal temperature control to mitigate screening current

A customized electric heater, "Thermal Eraser," is discussed an option to mitigate screening current in an HTS coil. The key concept of the Thermal Eraser is an optimal control of temperature gradient in an HTS coil to suppress screening current. An experimental study is performed to demonstrate its feasibility. A superconducting coil module, including an HTS coil and a Thermal Eraser, is designed, constructed, and tested in a conduction cooling environment. Through this study, it is confirmed that the Thermal Eraser activation can mitigate screening current.

Few techniques to mitigate screening current have been reported. However, the hardware-based techniques, e.g., field shaking coils, need additional space to be applied to an HTS magnet system. This may weaken the key advantage of HTS magnets in the aspect of compactness and high energy density. Thus, they have been barely integrated into HTS magnets so far. Meanwhile, a software-based current driving technique, i.e., so-called current sweep reversal (CSR), was proposed, tested, and validated. However, it has a deficiency that CSR utilization is ineffective when the peak current of CSR is less than about 80% I_c of an HTS magnet, which implies that the quench issue remains for the effective use of CSR. In conclusion, the Thermal Eraser may be a practical solution. With the Thermal Eraser, it is expected that both SCS and SCF issues would be addressed by substantial mitigation of screening current.

1.3 Thesis structure

The main goals of this thesis are to achieve a better knowledge of screening current behaviors, and develop a hardware-based device to mitigate screening current for an HTS magnet for addressing selected screening current issues. This thesis may promise disruptive technology of a high field magnet for the next generation NMR and MRI applications. The thesis is structured as follows:

Chapter 1 introduces the research background and purpose.

Chapter 2 provides introductory elements of screening current and magnetic resonance physics.

Chapter 3 presents numerical simulation methods of screening current and its detrimental effects on HTS magnet. The methods contain non-uniform current density simulation, current and voltage behavior simulation, nonlinear inductance simulation, harmonic coefficient simulation, and mechanical stress simulation.

Chapter 4 provides analysis results of HTS NMR magnets. Measurement results are compared with numerical simulation results. This chapter may verify the proposed numerical simulation methods in elucidating nonlinear electromagnetic behaviors that detrimentally affect HTS magnets.

Chapter 5 discusses a practical technique to mitigate screening current and its detrimental effects on an HTS magnet using a customized electric heater, “Thermal eraser.” The key idea is the optimal temperature control to degrade spatially-distributed critical current. Design, construction, and operation results of a superconducting module, including an HTS coil and a Thermal Eraser, were performed. Consequently, the feasibility was validated.

Chapter 6 summarizes the conclusions. This chapter emphasizes the significance of this thesis. Major issues of high field HTS magnets for NMR and MRI applications are addressed with the Thermal Eraser and nonlinear numerical simulation methods. It is believed that this thesis would help pave the way for the next generation NMR and MRI applications.

Chapter 2

Theoretical Background

2.1 Fundamental Physics of Superconductors

Superconductivity is an extraordinary physical property which can be observed only in certain materials where electrical resistance and magnetic field abruptly vanish. This phenomenon was discovered in 1911 by Dutch physicst Heike Kamerlingh Onnes when he was inverstigating electrical resistance of various metals at low temperatures [84]. Conventional approach to electrical resistance of metals at low temperatures was smooth convergence to residual resistance due to the impurity scattering in metals [85]. So as to study the relation between the purity and the residual resistance of pure metals, Onnes carried out experiments with mercury, the most purest metal at that time, which was the first discovery of superconductivity. Note that whether a material exhibits superconductivity can not be determined only by zero electrical resistance at low temperatures. What characterize superconductor from perfect electric conductor is expulsion of magnetic flux from the interior of the superconductor. The expulsion of magnetic flux, known as Meissner effect, can not be happen in a perfect electric conductor where the magnetic flux must remain as it was when the electrical resistance became zero. Thus, a superconductor can be said to exhibit perfect diamagnetism since there is no magnetic flux inside. Magnetic behavior of a superconductor

is shown in Fig. 2.1 In order to construct a constitutive equations of electrodynamics, Fritz and Heinz London conceived London equations to describe expulsion of magnetic flux from the interior of superconductors in 1935 [84]. Meissner effect implies that magnetic flux is always zero inside superconductors and magnetic flux should be dispelled away rapidly along the surface of superconductors. By introducing minor change to Maxwell's equation, one can obtain a differential equation of magnetic flux **B** as follows:

$$\nabla^2 \mathbf{B} = \frac{1}{\lambda_L^2} \mathbf{B}, \tag{2.1}$$

where λ_L is London penetration depth. By solving the differential equation, **B** decreases exponentially as the distance inside a superconductor. λ_L is known to change as the temperature T changes as $\lambda_L \propto 1/\sqrt{1-(T/T_c)^4}$ where T_c is the critical temperature of a superconductor [86]. Note that the London equations can not explain all the electrodynamics in superconductors since the equations are oversimplified.

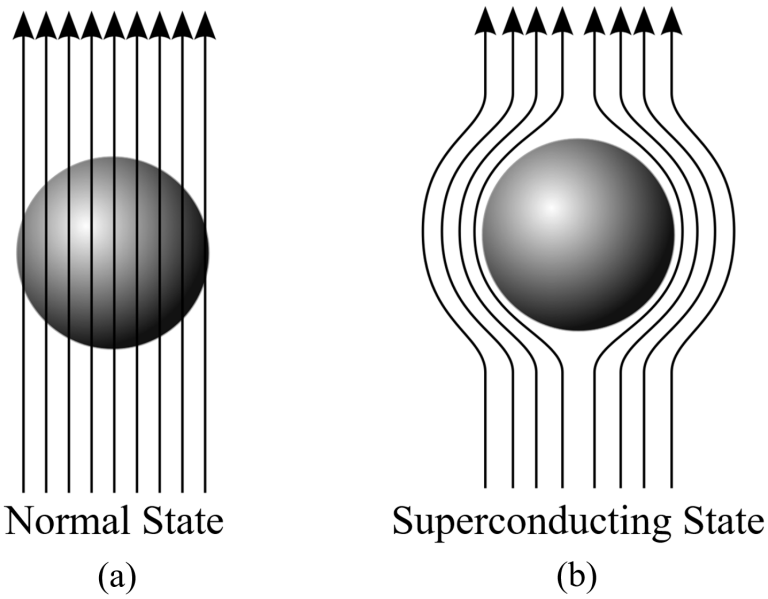

Figure 2.1: Magnetic behavior of a superconductor when the metal is (a) normal state and (b) supercnoducting state. Here arrows indicate applied magnetic flux lines.

After the discovery of superconductivity, many physicists had been trying to explain the superconductivity and its physical behaviors [87–89]. In 1957, John Bardeen, Leon Cooper, and John Robert Schrieffer proposed the first microscopic theory of superconductivity called BCS theory [90]. According to BCS theory, superconducting current can be explained as a superfluid of Cooper pairs which are pairs of two electrons interacting through phonons. Here, Cooper pair is boson whose spin quantum number (0,1,2,...) has an integer while an electron is fermion whose spin quantum number has odd half-integer (1/2, 3/2, 5/2...). Though there exists Coulomb repulsion, electrons experience stronger attration between the electrons due to the electron-phonon interaction. Once the pairs are constructed, one has to add large energy to break the pairs whereas small amount of energy is enough to change the state of an electron in normal metal. The required energy to break Cooper pair is gap energy Δ which can be observed in tunneling experiments and the value at temperature T can be predicted by BCS theory as follows [91]:

$$\Delta(T) = \Delta(0)\sqrt{\cos\left(\frac{\pi}{2}\left(\frac{T}{T_c}\right)^2\right)}, \tag{2.2}$$

where $\Delta(0)$ and T_c are gap energy at absolute 0 K and critical temperature of the superconductor respectively.

Soon after discovery of superconductivity, physicists including Onnes believed that superconductors were able to carry almost “infinite” currents and attempted to make a superconductor magnet. However, physicsts found that superconductivity were destroyed when certain level of magnetic fields were applied to the material. A certain level of magnetic field which can destroy superconductivity is now known as critical magnetic field B_c. Phase transition from the superconducting state to the normal state with an applied magnetic field, and vice versa, can be described in thermodynamics. Considering the Gibbs free energy G of a superconductor in the absence of applied magnetic fields, let the Gibbs free energy per volume of the superconducting state is G_s and that of the normal state is G_n. If a superconductor is cooled below its critical

temperature, $G_n > G_s$ must be satisfied to maintain superconducting state. Suppose a body of volume V is uniformly magnetized by an applied magneitc field H_a and the corresponding magnetic moment is m, the given work energy is [92]

$$dW = Vd\left(\frac{1}{2}\mu_0 H_a^2\right) + \mu_0 H_a dm, \tag{2.3}$$

where μ_0 is vacuum permeability. With the definitions of change in the magnetic moment energy $dW_m = \mu_0 H_a dm$ and the classical work done by pressure $dW_v = -pdV$, the Gibbs free energy can be defined with an applied magnetic field as follows:

$$G = U - TS + pV - \mu_0 H_a m, \tag{2.4}$$

where U and S are internal energy and entropy respectively. If H_a and m are changed while T and p are kept constant($dT = dp = 0$), infinitesimal change in G can be expressed as

$$dG = dU - TdS + pdV - \mu_0 H_a dm - \mu_0 m dH_a. \tag{2.5}$$

With the definition of U with an applied magnetic field, $dU = TdS - pdV + \mu_0 H_a dm$ is satisfied by the first law of thermodynamics. Thus, the change in Gibbs free energy with an applied field H_a and the corresponding magnetic moment m can be simplified as $dG = -\mu_0 m dH_a$. If phase transition between the superconducting state and the normal state occurs when $G_s(T, H) = G_n(T, 0)$, the B_c can be given as

$$B_c(T) = \sqrt{2[G_n(T,0) - G_s(T,0)]}. \tag{2.6}$$

Superconductors can be classified into type-I and type-II based on their physical properties. A criteria to tell type-I from type-II superconductor is to check the Ginzburg-Landau dimensionless parameter $\kappa = \lambda_L/\xi$, which is defined as the ratio of the two characteristic lengths of London penetration depth λ_L and coherence length ξ [93]. Here, ξ is a minimum distance for superconducting electron density to be changed [94]. Since λ_L is related to superconducting electron density and ξ is related to Fermi velocity and the gap energy of the material, λ_L as well as ξ are the

characteristic physical parameters which determine the sign of surface free energy of the superconductor. Type of a superconductor can be determined by following criteria

$$\begin{aligned} \kappa &< \frac{1}{\sqrt{2}} \quad \text{(Type-I superconductor)} \\ \kappa &> \frac{1}{\sqrt{2}} \quad \text{(Type-II superconductor)}. \end{aligned} \tag{2.7}$$

The estimation of critical magnetic field can be derived from Ginzburg-Landau theory [86]. The fluxoids are packed as far as the coherence length allows at the critical magnetic field. Each fluxoid core is carrying a flux of the order of $\pi\xi^2 B_{c,2}$ which has the same value to the quantum of magnetic flux Φ_0. Thus,

$$B_{c,2} = \frac{\Phi_0}{2\pi\xi^2}, \tag{2.8}$$

where Φ_0 is quantum of magnetic flux ($\Phi_0 = 2.067 \times 10^{-15}$ Wb). Key parameters of various superconductors which are widely used in industries are shown in Table. 2.1 [85, 95–97].

Table 2.1: Critical temperature, critical magnetic field, intrinsic coherence length, and London penetration depth of superconductors at 0 K

Material	T_c [K]	B_c [T]	ξ [nm]	λ_L [nm]	κ	Type
Tin	3.7	0.031	230	34	0.16	Type-I
Aluminum	1.2	0.010	1,600	16	0.010	Type-I
Niobium	9.5	0.20	38	39	1.02	Type-II
YBCO	92	140*	1.5	103	68	Type-II

Note that $B_{c,2}$ of YBCO in Table. 2.1 is calculated with (2.8) and the type of a superconductor is determined using (2.7).

Another criteria to categorize superconductors is the critical temperature T_c. Usually, low temperature superconductors (LTSs) are materials that show superconductivity below 30 K while high temperature superconductors (HTSs) are materials that show superconductivity at temperatures above 30 K. Nowadays some of superconductor magnet engineers who research HTS application think that HTS should have its T_c above 77 K which is the boiling point of liquid nitrogen. Most of metallic superconductors show superconductivity far below 77 K so they are classified as LTS while majority of ceramic based superconductors are classified as HTS. Conventional theory on superconductivity such as BCS theory expected that superconductivity can not be shown above about 30 K [90]. However, Karl Alexander Müller and Johannes Georg Bednorz succeeded in fabricating the first HTS in lanthanum-barium-copper-oxide (LBCO) at 35 K in 1986 [98]. Since HTS in cuprates including LBCO and YBCO can not be explained fully by BCS theory [99], there are Lawrence-Doniach model and anisotropic Ginzburg-Landau model for the analysis of layered structure in HTS [100]. In the models, layered superconductors can be seen as a stacked array of 2 D superconductors which are coupled together by Josephson tunneling effects. With the anisotropic Ginzburg-Landau model, the equation of critical magnetic field as shown in (2.8) should be calculated along with the direction of lattice. By setting ab-axis as parallel to a plane while c-axis as perpendicular to a plane, the critical magnetic field along the direction can be expressed as follows [86]

$$\begin{aligned} B_{c,2||ab} &= \Phi_0/2\pi\xi_{ab}^2 \\ B_{c,2||c} &= \Phi_0/2\pi\xi_c^2, \end{aligned} \tag{2.9}$$

where $B_{c,2||ab}$ and $B_{c,2||c}$ are the upper critical magnetic fields along the parallel and perpendicular direction respectively. One can easily infer that the maximum strength of magnetic field that HTS can maintain superconductivity is different along the direction of the magnetic field from (2.9). Last key parameter of superconductors used for manufacturing high field magnets is the critical current density J_c. According to London theory, J_c of a bulk superconductor can be easily derived as $J_c = B_c/\mu_0\lambda_L$ [84].

Unlike this simple method to calculate the critical current density, J_c of HTS especially in cuprates is known to be dependent on λ_L and ξ [86]. HTS in cuprates such as REBCO has an orthorhomic crystal lattice structure, where the a and b axis in the plane are not exactly same. Since point defects and impurities accumulate along such a twin boundary, more vorticies can be attracted. There have been a number of studies on the artificial defects and the critical current densities of HTS in cuprates [101–104]. As mentioned, there are analytic equations of the J_c estimation for HTS in cuprates. However, the equations are derived from Ginzburg-Landau theory with an assumption that uniform shear strains are applied to the crystal lattice by triangular flux lines lying in an HTS with $\kappa \gg 1$ and the applied magnetic field B is much lower than the upper critical magnetic field $B_{c,2} \gg B$ [105]. Thus, in this literature, the critical current density of HTS in cuprates as a function of applied magnetic field strength $|B|$ and angle between the plane and the applied magnetic field θ is calculated using the curve-fitting approach from the measured data similar to [106]. Details on the calculation method for J_c of HTS are introduced in chapter 3.

In order to build high field magnets, it is desirable that more currents should flow to conductors without electrical resistance. It is plausible for engineers to use HTS for magnet construction since HTS has high J_c and B_c compared to other materials. However, HTS shows nonlinear resistance in the mixed state where a superconductor is no longer able to maintain perfect diamagnetism [86]. This nonlinear property has been one of the most important challenges to be addressed and physicists have attempted to describe the phenomenon using microscopic theory. Meanwhile, mixed state of a typical type-II superconductor can be further divided into vortex-glass state and vortex-fluid state when describing HTS in cuprates. When HTS is in the vortex-glass state, there is Lorentz force between the currents and the normal state cores carrying quantized magnetic flux. Here, the normal state core, known as vortex, is generated by the circulating currents. According to the Abrikosov vortex lattice theory, a superconductor without imperfections will show a nonzero resistivity since the

vortices are tend to be pinned at imperfections in the material if the applied Lorentz force is not too great. However, as the transport current density J_t and the temperature are increased, so that the Lorentz force with thermal fluctuation exceeds the average pinning force between the pinned vortices, the vortices are not able to resist moving through the material. Here, unlike LTS, thermal fluctuations to vortices become important for HTS because the critical temperature is high while the energies to create and move vortices are small [105]. This microscopic picture of vortex flow is known as vortex-fluid state while the vortex-glass critical temperature T_g is also known as glass-melting temperature. D. Fisher *et al.* approached the vortex-glass phase analysis by using the scaling analysis [105]. According to the studies, in the vortex-glass phase below T_g, the nonlinear electric field E as a function of the current density J can be approximated as:

$$E/J \simeq e^{-(J_T/J)^{\alpha}}, \tag{2.10}$$

where α is a constant and J_T is the characteristic current scale set by these thermal fluctuations. With strong thermal fluctuations in HTS, $J_c \simeq J_T$ can be satisfied [107]. The fundamental research on the nonlinear electromagnetic constitutive law between E and J of HTS was rapidly expanded to in-depth research on the current distribution J in HTS wires. Many researchers have made numerous efforts to calculate non-uniform current density, including transport current density J_t and screening current density J_{sc}. As a result, multiple engineered models have been reported. Finally, the so-called power law E–J constitutive law has been established as a "standard" model for the current density analysis of HTS [105]:

$$E = \frac{E_c}{J_c}\left|\frac{J}{J_c}\right|^{n-1} J, \tag{2.11}$$

where n is the index number for the power law E–J constitutive equation.

Bean proposed a critical state model assuming an ideal superconductor to describe non-uniform current distribution; the critical state model can be expressed with (2.11) assuming $n = \infty$. From multiple experimental studies, the plausibility of Bean's crit-

ical state model was validated with pure metal superconductors (type-I superconductors). For HTS, the critical state model is indeed invalid for describing the exact current distribution mechanism since the index value of HTS is finite. Nevertheless, this thesis revisits Bean's critical state model because it intuitively explains the magnetization and the corresponding highly non-uniform current distribution in a superconductor—Bean's theory is revisited with the textbook written by Y. Iwasa *et al.* [108].

Bean assumes that an HTS wire is defined as a slab of width $2a$ (in the x-direction) and infinite lengths in the y- and z-direction. He describes the current distribution inside a slab using the magnetic field quantities stated as follows: field itself H, flux density B, and magnetization $\bar{M}$ in y-direction. The corresponding electric current quantities are current I and current density J flowing in the z-direction. Additionally, he essentially supposes that J is equal to J_c. Two classic examples of Bean's model are discussed: an HTS slab exposed to an external magnetic field and an HTS slab excited by a transport current.

For the first example, Figure 2.2 illustrates the magnetization mechanism of an HTS slab exposed to an external magnetic field without transport current and the corresponding current distribution. The electric field penetrates from both edges of the slab. It is the key feature of the current distribution induction mechanism in superconductors. Note that the induced current by the penetration magnetic field against the slab is screening current. Ampére's law of Maxwell's equations ($\nabla \times \mathbf{H} = \mathbf{J} = [0, 0, J_c]$) can describe the magnetic field distribution inside the HTS slab. The result of internal magnetic field distribution when external magnetic field is applied, shown in Figure 2.2, is provided with $H_s(x)$:

$$H_s(x) = \begin{cases} 0 & (x^* \leq x \leq x^+) \\ H_e - J_c x & (0 \leq x \leq x^*) \\ H_e + J_c(x - 2a) & (x^+ \leq x \leq 2a) \end{cases} \tag{2.12}$$

where H_e is applied external magnetic field. x^* and $2a - x^+$ are the field penetration

depth in the slab and they are presented with:

$$x^* = \frac{H_e}{J_c}. \tag{2.13}$$

If the H_e becomes over the full penetration field of $H_p \equiv J_c a$, the entire slab is in the critical state. The average magnetic induction with the slab, $\bar{B}_s$, and the average magnetization $\bar{M}$ can be described with:

$$\bar{B}_s = \begin{cases} \frac{\mu_0 H_e^2}{2H_p} & (0 \le H_e \le H_p), \\ H_e - \frac{H_p}{2} & (H_e \ge H_p), \end{cases} \tag{2.14}$$

$$\bar{M} = \begin{cases} \frac{H_e^2}{2H_p} - H_e & (0 \le H_e \le H_p), \\ -\frac{1}{2}H_p = -\frac{1}{2}J_c a & (H_e \ge H_p). \end{cases} \tag{2.15}$$

For the second example, Figure 2.3 provides magnetic field distribution and the corresponding current distribution inside an HTS slab excited by a transport current (I_t). As shown in Figure 2.3, when a transport current I_t flows in the slab, the current charges from the both edges due to screening current. The field distribution $H_s(x)$

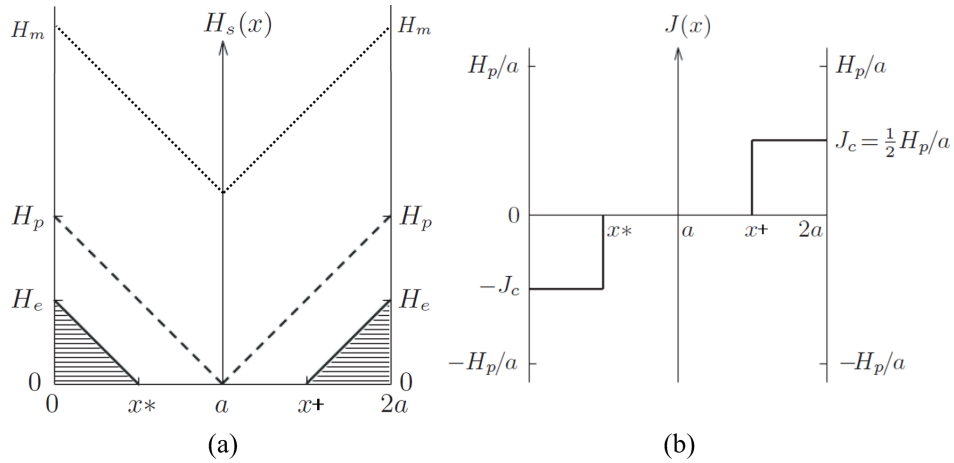

Figure 2.2: Magnetic field and current density distribution in the HTS slab when it is exposed to an external magnetic field; the slope magnitude of $\frac{\partial H_s(x)}{\partial x}$ is J_c.

within the slab is also induced from both edges of the HTS slab. In the Figure 2.3, x^* and x^+ are derived with assuming $I_t \leq I_c$:

$$-\frac{1}{2}I_t + J_c x^* = 0, \tag{2.16}$$

$$J_c(x^+ - 2a) + \frac{1}{2}I_t = 0, \tag{2.17}$$

$$x^* = \frac{I_t}{2J_c}, \tag{2.18}$$

$$x^+ = 2a - \frac{I_t}{2J_c}. \tag{2.19}$$

If $I_t \geq I_c$, $x^* = x^+ = a$. This case is also called a critical state. Let's assume that I_t is less than I_c of the given HTS slab, then magnetic field inside the slab $H_s(x)$ is described with:

$$H_s(x) = \begin{cases} 0 & (x^* \leq x \leq x^+) \\ J_c(x - x^*) & (0 \leq x \leq x^*) \\ J_c(x - x^+) & (x^+ \leq x \leq 2a) \end{cases}. \tag{2.20}$$

Note that the corresponding average magnetic induction and magentization by self-induced field are zero.

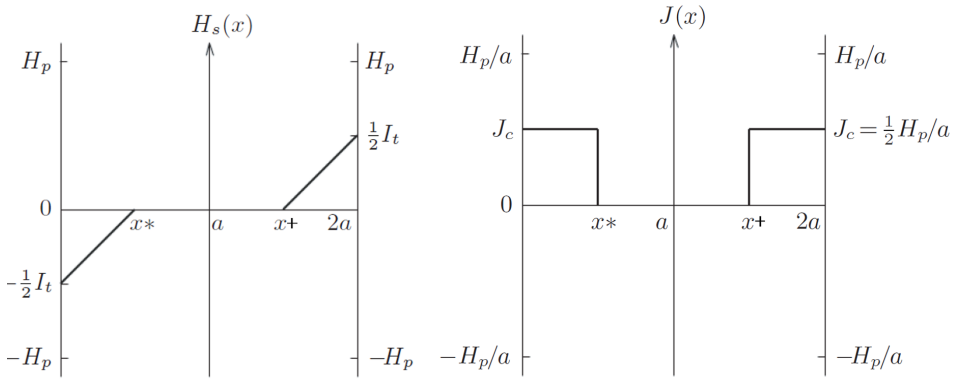

Figure 2.3: Effect of transport current on magnetization: the magnetic field distribution with I_t in the slab, and the corresponding current distribution.

So far, fundamental physics has been provided. The fascinating nature of superconductivity provoked in-depth studies of how much current can flow in superconductor without Joule heating loss, and the ability was defined by using critical electromagnetic quantities. After primary theories of superconductivity were established, researchers have aimed to investigate the current distribution. As a result, they have revealed that screening current and the consequent non-uniform current distribution are induced by the nature of superconductivity and proposed effective electromagnetic constitutive law to describe the electric conductivity. As a result, the power-law model, also known as the 'index' model, has become the standard model for superconductors. In this thesis, ideal assumptions for the power-law model were adopted to intuitively elucidate the current induction mechanism, including screening current. However, the ideal power-law model, Bean's critical state model, is inapplicable for an HTS magnet analysis practically since the assumption of J=J_c is invalid. Valuable studies considering field dependency on I_c have been performed in analytic manners. However, an apparent limit in deriving analytic solutions exists mainly due to the highly nonlinear nature of superconductivity. Thus, recently, numerical approaches to calculate current density in HTS were used. Details of the relevant studies are provided in the chapter 3.

2.2 The Basics of Spin Physics and Magnetic Resonance

The nature of spin is attractive. One of the fascinating phenomena relevant to spins in a particle is that the spin state can be changed by the absorption or emission of electromagnetic energy. Magnetic resonance is based on a consequential phenomenon caused by the energy absorption and emission of a particle having spins. Note that all the particles have their inherent spin quantity, while the net can be zero or non-zero.

If a particle whose net spin quantity is not zero is placed in magnetic field strength of B_0, it can absorb an energy corresponding to a particular radio frequency (RF). Here the RF quantity ν—it is commonly called the resonance frequency or the Larmor

frequency in NMR and MRI discipline—is determined by two factors: the type of particles and B_0. It can be described with:

$$\nu = \gamma B_0, \tag{2.21}$$

where γ is the gyromagnetic ratio of its magnetic moment to its angular momentum of a particle. Note that γ varies by the type of particles, as shown in Table 2.2.

The spin vector of a particle aligns itself to the direction of the applied direct-current magnetic field. The alignment can be changed by absorbing electromagnetic energy. The change can be described by adopting two definitions of the energy states of spin; one is named a low energy state where the vector is aligned according to the nature that the north pole (N) faces the south pole (S), and the other is named a high or upper energy state where the alignment is opposite, Figure 2.4. For example, a particle in the lower energy state can experience the state transition to an upper energy state as it absorbs the specific electromagnetic energy corresponding to a particular RF quantity ν_0. Here the required energy for the state transition is the energy difference E_{tr} between the energy quantities in two states, and the relation between E_{tr} and ν_0 can be described with Planck's constant (h=6.626 $\times$ 10^{-34}, [unit: Js]):

$$E_{tr} = h\nu_0 = h\gamma B_0. \tag{2.22}$$

Table 2.2: The list of most common nuclei showing MR and their gyromagnetic ratios

Nucleus	Gryoratio [MHz·T^{-1}]	Net spin
^{1}H	42.58	1/2
^{13}C	10.71	1/2
^{14}N	3.08	1
^{19}F	40.08	1/2
^{23}Na	11.27	3/2
^{31}P	17.25	1/2

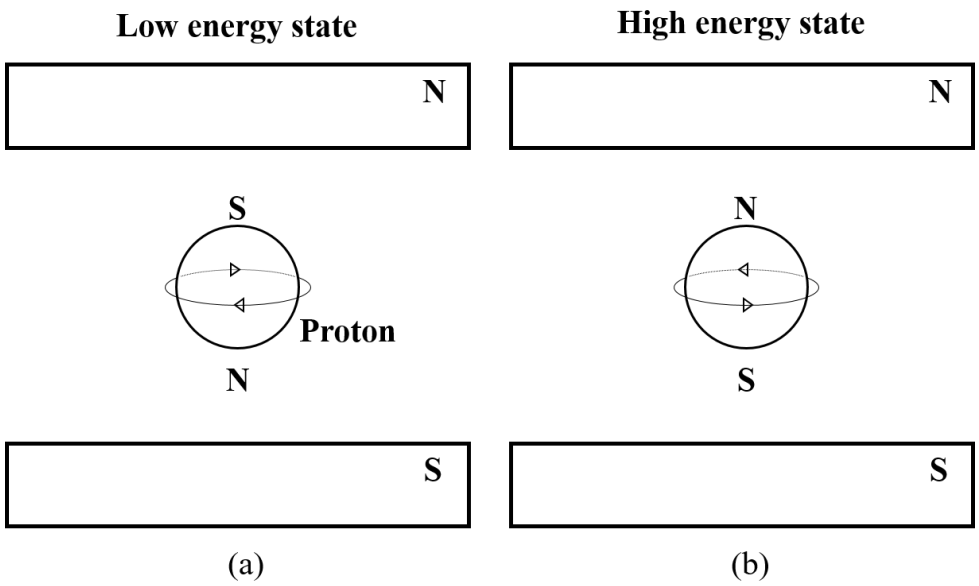

Figure 2.4: Two energy states of a particle, including spins, exposed to an external direct-current magnetic field: (a) low energy state and (b) high energy states.

So far, the microscopic view of spin dynamics has been reviewed. However, it can be limited in understanding MR physics since MR samples contain an enormous number of particles and spins. Thus, a simple but practical concept of "spin packet" was proposed. The spin packet is defined as a group of spins enduring the same magnetic field. For instance, four spins within each grid section (a box with black dotted lines) can be considered as a spin packet, as provided in Figure 2.5. Then, the sum of the magnetization vectors of spins of individual particles in a packet can be transformed into the net magnetization of a packet. The net magnetization vector of spin packets M_0 tends to be aligned to the direction of the applied direct-current magnetic field B_0 at the equilibrium state of spins. Here it can be found why the main magnets for NMR and MRI applications require uniform magnetic fields in MR samples at a glance; the primary purpose of uniform magnetic fields from the main magnet may be to consider an NMR or MRI sample a continuum body in terms of MR.

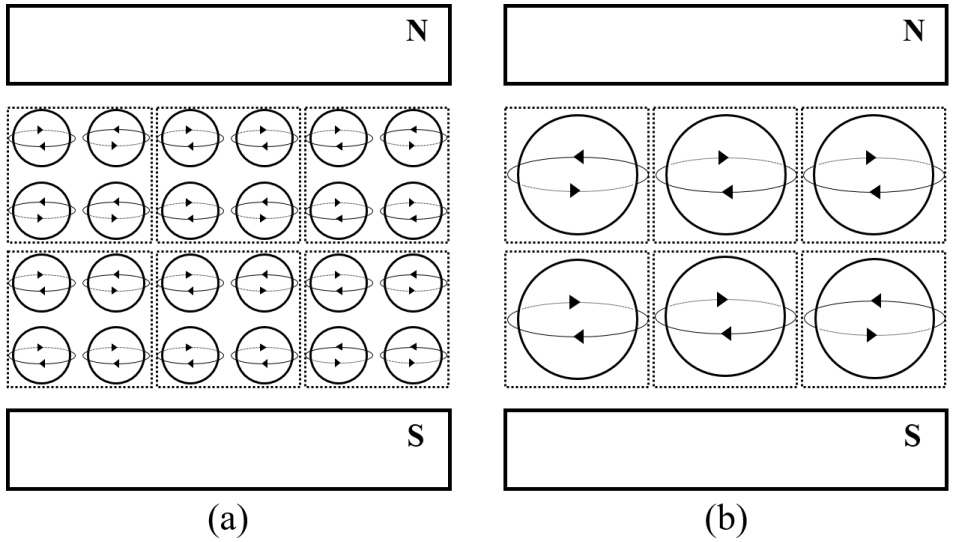

Figure 2.5: Example of a spin packet: (a) individual spins and (b) spin packets.

When a group of spins is exposed to B_0, all the spins may not be aligned to B_0. In this situation, the ratio between the number of spins in the lower energy level N^+ and the number of spins in the upper level N^- can be defined with Boltzmann statistics:

$$N^-/N^+ = e^{-E/kT}, \tag{2.23}$$

where k is Boltzmann's constant (1.3805×10^{-23}, [unit: J/K]). With (2.23), it is expected that as the temperature increase, the ratio gradually closes to 1, which implies the net magnetization vector becomes 0. In this situation, the MR phenomenon for NMR and MRI might be inapplicable. On the other hand, as the temperature decrease, the ratio becomes 0, so only one state for individual spins exists. It may be an ideal condition for MR applications. Meanwhile, assuming that an MR sample is located in a room temperature bore of NMR and MRI applications, the ratio is any value between 0 to 1. It implies that N^+ is larger than N^-. However, one can notice that the N^- can become larger than N^+ if the electromagnetic energy is absorbed, and N^- can become its original value after the emission of absorbed electromagnetic energy.

Figure 2.6 provides an example of MR phenomena in the cartesian coordinate (x,y,z). In the figure, it is assumed that the net magnetization vector along the z axis (M_z), called the longitudinal magnetization, equals M_0, and there are no transverse components of the magnetization (M_x and M_y). The net magnetization can be changed as shown in Figure 2.6(b) when spins are suffered from the particular RF magnetic field excitation. Assuming that enough energy is applied to the spin system, the net magnetization of the given spin system can be $M_z = 0$ or even $M_z = -M_0$. After the RF excitation is end, the net magnetization gradually return to its original state where M_z=M_0. This phenomenon is called T1 process of MR. The time constant, which describes the relaxation process of M_z, is called the spin-lattice relaxation time T_1. It is defined as the time required to change the longitudinal component of the net magnetization by a factor of e. A function of M_z for the spin-lattice relaxation can be governed by:

$$M_z = M_0(1 - e^{-t/\mathrm{T}_1}), \tag{2.24}$$

or

$$M_z = M_0(1 - 2e^{-t/\mathrm{T}_1}), \tag{2.25}$$

where $M_z = 0$ and $M_z = -M_0$, respectively.

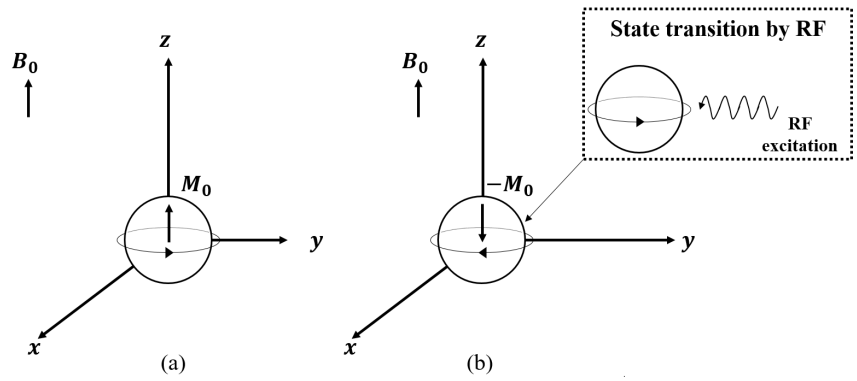

Figure 2.6: The net magnetization of a spin system at (a) equilibrium state and (b) a excited state.

Suppose that the net magnetization is placed in the $x - y$ plane, then it will rotate on the surface as shown in Figure 2.7—this case is slightly different from the previous case. It is called precession. Additionally, the net magnetization starts to dephase since each spin packet is exposed to a slightly different magnetic field and rotates at its Larmor frequency. As a result, the phase difference between spin packets becomes bigger when the longer the elapsed time. Let's assume that the net magnetization vector M_0 at the equilibrium state is initially aligned to y-axis. Then, the dephasing process of each spin packet can be superposed on the $x - y$ plane, as shown the shaded region in Figure 2.7(b). Here the time constant of M_{xy} that describes the return to equilibrium of the transverse magnetization, can be defined with:

$$M_{xy} = M_0 e^{-t/\mathrm{T}_2}.$$

This phenomena is called the spin-to-spin relaxation and known as "T2" process. Meanwhile, it is easily found that T_2 is less than or equal to T_1.

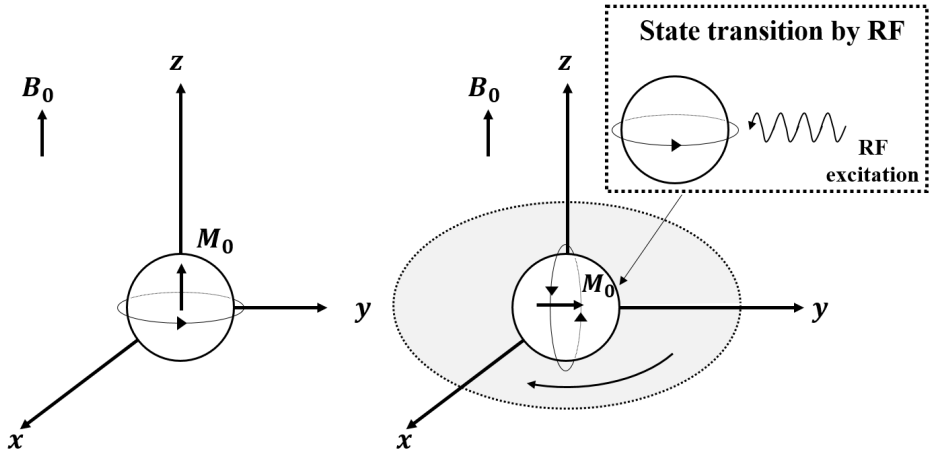

Figure 2.7: Electromagnetic behaivors of the net magnetization when it is placed in the $x - y$ plane: (a) the net magnetization at equilibrium state and (b) an example of the precession due to the alignment of the net magnetization on the $x - y$ surface.

The net magnetization in the $x-y$ plane is relaxed to zero and then the longitudinal magnetization becomes M_0 along z. Any transverse magnetization M_{xy} undergos the same precession, as shown in Figure 2.8. M_{xy} rotates about the direction of applied magnetization and dephases. One thing note here is that T_1 is the dominant to determine the rate of recovery of M_z. Meanwhile, a rotating frame for investigating the T1 and T2 processes is commonly adopted. It assumes that the frame rotates at the Larmor frequency. Then, the descriptions of the dephasing process become resolved mathematically. Consequently, it becomes possible to consider only the z-component magnetization in the analysis.

In general, the basic spin physics for MR can be governed by the Bloch equations:

$$\begin{aligned}
\frac{dM'_x}{dt} &= (\omega_0-\omega)M'_y - \frac{M'_x}{\mathrm{T}_2},\\
\frac{dM'_y}{dt} &= -(\omega_0-\omega)M'_x + 2\pi\gamma B_1 M_z - \frac{M'_y}{\mathrm{T}_2},\\
\frac{dM_z}{dt} &= -2\pi\gamma B_1 M'_y - \frac{M_z - M_{zo}}{\mathrm{T}_1},
\end{aligned} \tag{2.26}$$

where $\omega_0 = \gamma B_0$, and ω is the frequency of the rotating frame. The Bloch equations are a set of coupled differential equations that can be used to describe the behavior of a magnetization vector under any conditions. When properly integrated, the Bloch equations will yield the x', y', and z components of magnetization as a function of time, where x' and y' is a rotating frame of reference—it is sometimes convenient to define a rotating frame of reference which rotates about the z axis at the Larmor frequency since a magnetization vector rotating at the Larmor frequency in the laboratory frame appears stationary in a frame of reference rotating about the z-axis.

So far, the basics of MR have been reviewed. The fundamental physics can emphasize the need for high field superconductor magnets for MR applications. In addition, it may suggest the importance of spatial field uniformity and temporal field stability of a superconductor magnet for MR applications. In these aspects, one can conclude that detrimental SCF effects on spatial field uniformity of an HTS magnet may be a critical issue of HTS magnet technology for NMR and MRI applications.

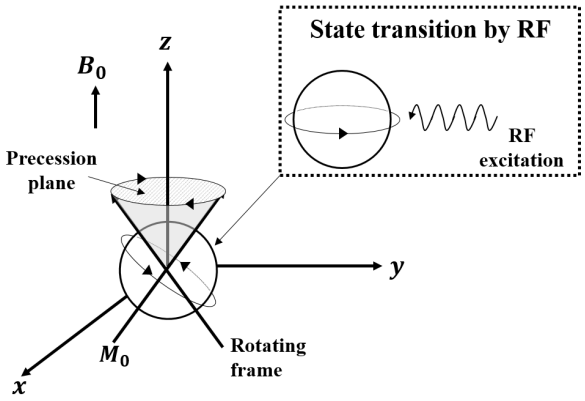

Figure 2.8: Example of the precession of the transverse magnetization of M_{xy}.

NMR spectroscopy for biochemistry

The principle of NMR spectroscopy consists of three sequential steps. First, externmal magnetic field is applied to spins in an NMR sample. Second, an RF magnetic field is excited to perturb the alignment of spins. Third, the relaxations of spins, i.e., T1 and T2 relaxations, are detected by measuring the electromagnetic waves emitted from spins of nuclei in the NMR sample.

In order to understand NMR spectroscopy, additional properties should be studied: the so-called chemical shift and free induction decay of time-domain NMR signal. As explained above, when spins are exposed to an external magnetic field, they are aligned to the field. Here the spin alignment can cause a small magnetic field as acting a small magnetic dipole. As a result, the magnetic field at a nucleus in an NMR sample slightly differs from the applied field in general. This phenomena of local magnetic field at a nucleus (B_{NMR}) can be described with a fraction (σ_{NMR}):

$$B_{NMR} = B_0(1 - \sigma_{NMR}). \tag{2.27}$$

In some cases, the circulation of the electrons can induce a small magnetic field perturbation, and the consequent the enhancement of B_0, as shown in Figure 2.9. This phenomenon is called deshielding, and it causes chemical shift in NMR spectroscopy.

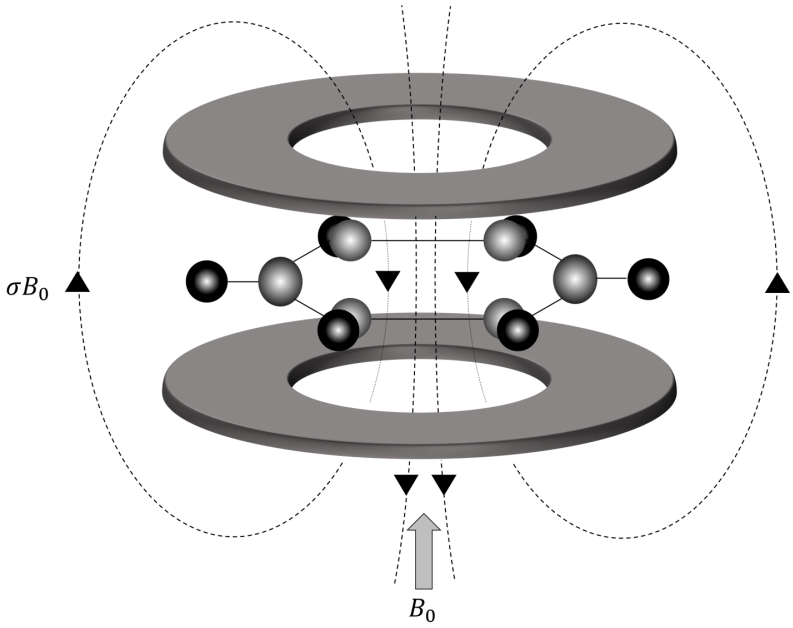

Figure 2.9: Example of deshielding: a variation of the benzen modelcule

Second, an NMR sample contains many different magnetization components. It implies that different magnetization components are associated with the nuclear spin configurations with each transition according to the energy level diagram. Then, an NMR spectrum from the given sample is captured with many different frequency lines. For instance, in pulsed an NMR spectroscopy, an NMR signal is detected after these magnetization vectors are aligned on the $x-y$ plane. Once a magnetization vector is in the $x-y$ plane it rotates about the direction of the z axis and it thus generate a current in a coil of wire located around the x axis for the signal detection with a probe. Plotting current as a function of time gives a sine wave. This wave will, of course, decay with time constant T2* due to dephasing of the spin packets. This signal is called a free induction decay (FID).

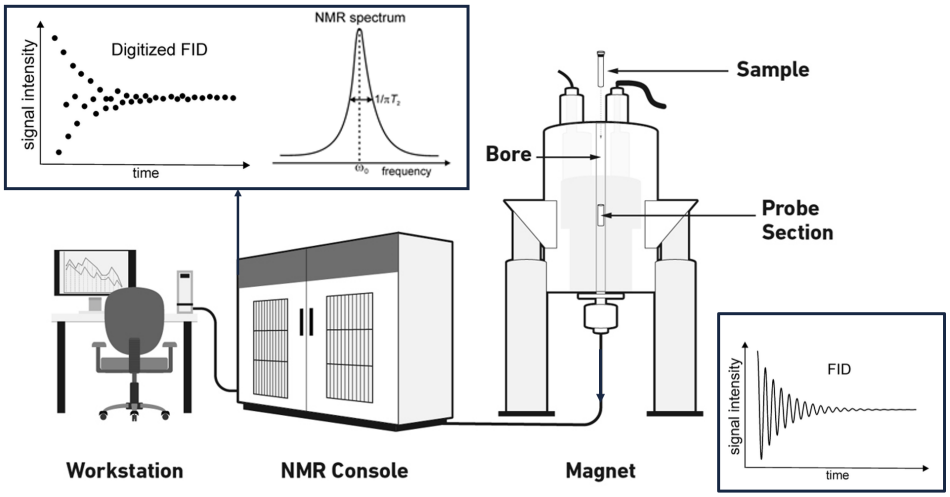

Figure 2.10: Schematic drawing of an NMR spectrometer with its key components.

MRI scanncer for medicine

For MRI, unlike NMR, a spatial encoding process is needed to clarify the location of each net magnetization. Linear gradient magnetic field in the direction of x, y, and z of a cartesian coordinate frame is adopted for the spatial encoding for MR imaging; the gradient field intensities are defined as G_x, G_y, and G_z, respectively. For example, in the presence of G_x, the resonance frequency, also called Larmor frequency, of the spins in a sample, e.g., human body or brain, can be described with a function of x:

$$\omega(x) = \gamma(B_0 + G_x x),$$

where B_0 is an external magnetic field that is aligned to the z axis. Therefore, the signal from the spins can be spatially encoded in the frequency domain. In MR physics, the two-dimensional Fourier domain is commonly called "k-space." It is derived from the RF signal induced by the relaxation of magnetization vector from spins in an MRI sample, which is encoded by gradient fields. Considering 2D-imaging with encoding gradient G_x and G_y, sampling 2D k-space— it is the digitization of analog data space– is performed by modulating the time interval of G_x and G_y. Then, the signal in a time

domain of the spins, $s(t_x, t_y)$, can be desribed as follows:

$$s(t_x, t_y) = \int_x \int_y m(x, y) e^{-i\gamma(G_x x t_x + G_y y t_y)} dx dy = \mathcal{F}\Big[\Big[m(x, y)\Big]\Big]$$

where t_x and t_y are time interval of G_x and G_y, m is a reconstructed image, and $\mathcal{F}\Big[\Big[f(x, y)\Big]\Big]$ is a 2D Fourier transform operation.

Meanwhile, the signals in MRI are measured by the relaxation of the spins, so two independent relaxations occur, which are named as T1 and T2 relaxation. Each relaxation has different physical mechanism with different time constant. This T1 and T2 relaxation behavior is phenomenologically described with the Bloch equation:

$$\frac{d\mathbf{M}}{dt} = \mathbf{M} \times \gamma\mathbf{B} - \frac{M_x \hat{x} + M_y \hat{y}}{\mathrm{T}_2} - \frac{(M_z - M_0)\hat{z}}{\mathrm{T}_1},$$

where $\mathbf{M}$ consists of (M_x, M_y, M_z), and M_0 is an initial magnetization. Therefore, the measured signal from MRI can be determined by T1 and T2 relaxations of the tissue (sample). Each tissue of the organism has its own T1 and T2 constants. As a result, in the MRI discipline, there are two weighted images, T1-weighted and T2-weighted, as shown in Figure 2.12.

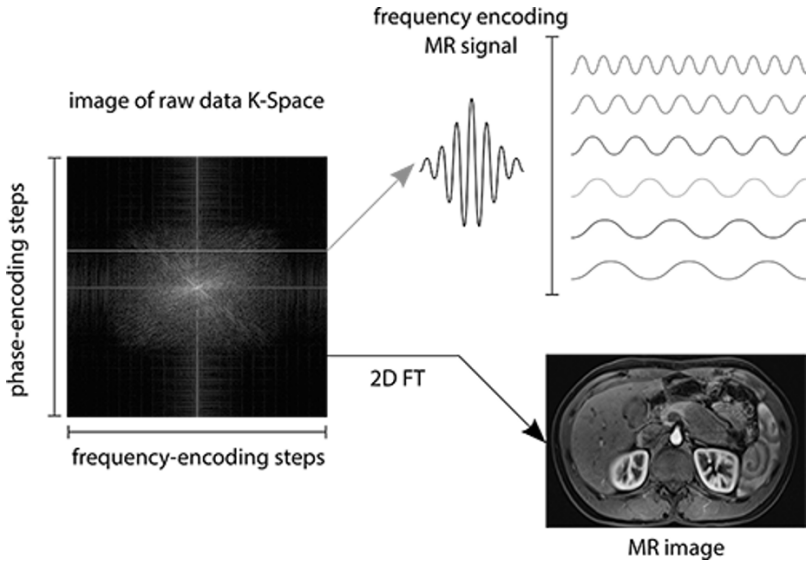

Figure 2.11: Conceptual drawing of an MRI principle.

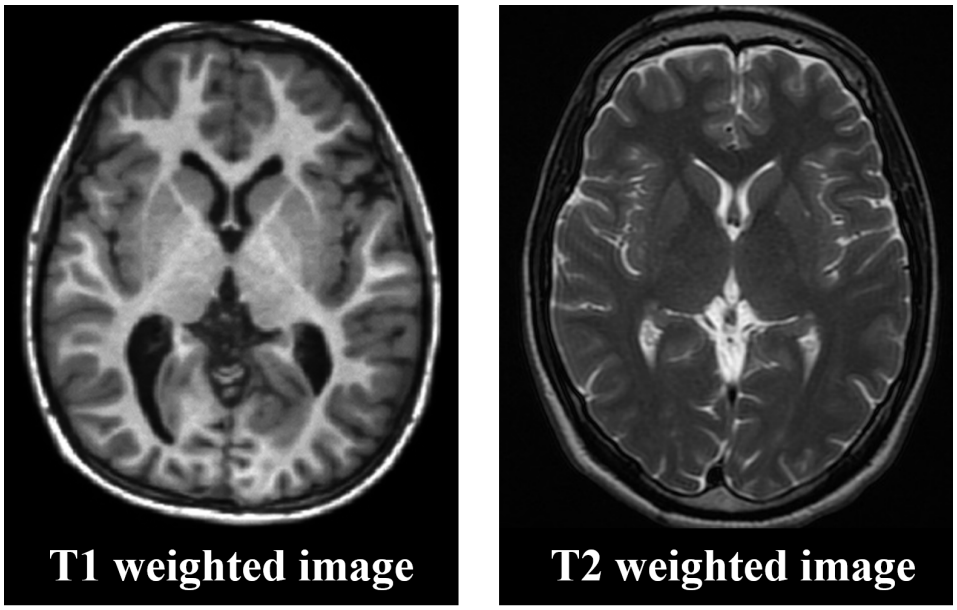

(a) (b)

Figure 2.12: Examples of brain MRI images: (a) T1-weighted image and (b) T2-weighted image.

Chapter 3

Numerical Methods to Simulate Screening Current and Its Detrimental Effects on HTS Magnet

3.1 Non-uniform Current Distribution Simulation Method

Numerical analysis of non-uniform current distribution due to screening current in an HTS magnet is challenging with conventional electromagnetic simulation. The key difficulty is that the conventional simultion based on the finite element method (FEM) can not deal with the nonlinear conductivity of HTS. Numerous efforts have been made to address the relevant issues. As a result, novel simulation approaches are suggested as shown in Table 3.1 [109]. They enable the analysis of non-uniform current distribution, including transport and screening current. The table summarizes governing equations for E field formulation, H field formulation, A-ϕ formulation, and T-ϕ formulation methods. Among the formulation methods, H formulation method is known for its calculation accuracy when it is adopted as the governing equation for FEM simulation.

A FEM-based numerical simulation method adopting H formulation is thus studied in this thesis. In addition, a numerical simulation technique, called the domain homogenization technique, is investigated. An integrated nonlinear numerical simulation method is developed to analyze screening current, including the H formulation

method and domain homogenization technique. The results are described below.

Table 3.1: Differential formulations of Maxwell's equations used to simulate electromagnetic behaviors of HTS magnet

Formulation	Equation	Definitions
A-ϕ	$\nabla^2\mathbf{A} = \mu\sigma(\frac{\partial\mathbf{A}}{\partial t} + \nabla\phi)$	$\mathbf{B} = \nabla \times \mathbf{A}$
	$\nabla \cdot (\sigma\frac{\mathbf{A}}{t} + \sigma\nabla\phi) = 0$	$\mathbf{E} = -\frac{\partial\mathbf{A}}{\partial t} - \nabla\phi$
		$\sigma = \sigma(E)$
T-ϕ	$\nabla \times \rho\nabla \times \mathbf{T} = -\mu\frac{\partial(\mathbf{T}-\nabla\phi)}{\partial t}$	$\mathbf{J} = \nabla \times \mathbf{T}$
	$\nabla^2\phi = 0$	$\mathbf{H} = \mathbf{T} - \nabla\phi$
		$\rho = \rho(J)$
E field	$\nabla \times \nabla \times \mathbf{E} = -\mu\frac{\partial(\sigma\mathbf{E})}{\partial t}$	$\frac{\partial\mathbf{B}}{\partial t} = -\nabla \times \mathbf{E}$
		$\sigma = \sigma(E)$
H field	$\nabla \times \rho\nabla \times \mathbf{H} = -\mu\frac{\partial\mathbf{H}}{\partial t}$	$\mathbf{J} = \nabla \times \mathbf{H}$
		$\rho = \rho(J)$

1: **E**, **H**, **J**, **A**, and **T** are the vectors of electric field, magnetic field, current density, magnetic potential, current potential, respectively

2: ϕ is the scalar potential of electric field

3: ρ, σ, and μ stand for, respectively, the resistivity, conductivity, and permeability

3.1.1 H formulation of Maxwell's equations for governing equation

The H formulation-based FEM simulation method can directly calculate magnetic field vector **H** without using electromagnetics potentials [109]. One thing to note here is that the direct calculation of **H** is available when a unique element with particular vector shape functions incorporated is employed for FEM simulation. Unlike conventional methods using nodal elements for FEM simulation of electromagnetics, the H formulation method thus utilizes the so-called edge elements, also known as curl elements, shown in Figure 3.1. These particular elements satisfy divergence rules of Maxwell's equations, i.e., Gauss's law. Consequently, the first-order point form of Maxwell's equations is applicable as the governing equation for the finite element analysis (FEA), and enables the direct calculation of magnetic field quantities. The governing equations of the FEA with H formulation method are summarized with (3.1)–(3.2):

$$\mu \frac{\partial \mathbf{H}}{\partial t} + \nabla \times \mathbf{E} = 0, \tag{3.1}$$

$$\mathbf{E} = \rho \nabla \times \mathbf{H}. \tag{3.2}$$

The key strength of using the H formulation method with the edge element is that it can address the main difficulty of conventional analysis approaches. Note that they

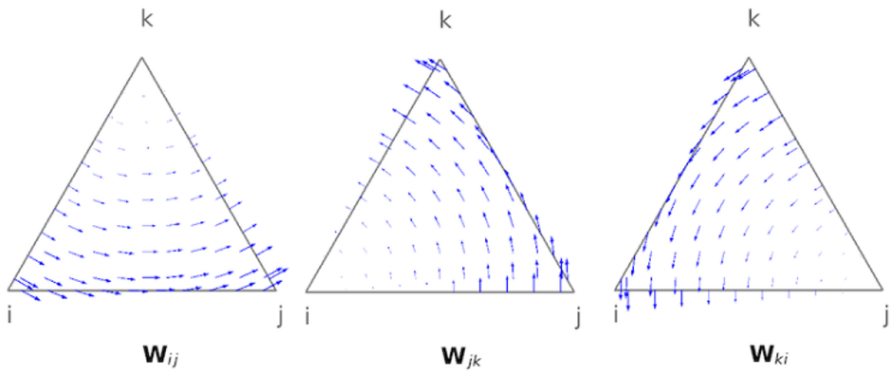

Figure 3.1: Shape functions of the first-order triangular edge element; $\mathbf{W}_{ij}$, $\mathbf{W}_{jk}$, and $\mathbf{W}_{ki}$ are the Whitney 1-form basis functions for the shape functions.

have suffered from analyzing non-uniform current distribution mainly due to the highly nonlinear material property of HTS. In detail, the second-order differential operator, i.e., $\nabla \times \nabla\times$, compels ill-condition and discontinuity problems, and it hinders the simulation as providing an unstable system matrix of FEA. As a result, the iterative process of finding a solution by minimizing the so-called "functional" of FEM slowly converges or even sometimes diverges. Meanwhile, these issues can be addressed by using the edge element since the second-order differential operator is not required.

Provided that appropriate assumptions are needed to conduct the FEA with H formulation. **H** and **E** have only two transverse and one longitudinal component, respectively. For instance, [H_r,0,H_z] and [0,E_ϕ,0] should be set to be electromagnetic quantities for the nonlinear FEA of an HTS magnet in a cylindrical coordinate (r,ϕ,z). Then, the governing equations can be given with (3.3)–(3.11) considering the general form of partial derivative equations in a cylindrical coordinate:

$$e_a \frac{\partial^2 \mathbf{u}}{\partial t^2} + d_a \frac{\partial \mathbf{u}}{\partial t} + \nabla \cdot \Gamma = f, \tag{3.3}$$

$$\mathbf{u} = \begin{bmatrix} H_r \\ H_z \end{bmatrix}, \tag{3.4}$$

$$\Gamma = \begin{bmatrix} 0 & -E_\phi\, r \\ E_\phi\, r & 0 \end{bmatrix}, \tag{3.5}$$

$$d_a = \begin{bmatrix} \mu\, r & 0 \\ 0 & \mu\, r \end{bmatrix}, \tag{3.6}$$

$$e_a = 0, \tag{3.7}$$

$$f = 0, \tag{3.8}$$

$$E_\phi = -\rho_\phi(J_\phi) J_\phi, \tag{3.9}$$

$$J_\phi = \frac{\partial H_z}{\partial r} - \frac{\partial H_r}{\partial z}, \tag{3.10}$$

$$\rho_\phi = \frac{E_c}{J_c} \left| \frac{J_\phi}{J_c} \right|^{n-1} J_\phi, \tag{3.11}$$

where E_c, J_c, and n are, respectively, the critical current, critical current density, and the index number for the power-law model. One thing to note here is that the resistivity of HTS, which is electromagnetic material property of HTS, depends on current density. The resistivity is described with the so-called power-law model of the E–J constitutive law of HTS (see Figure 3.2) [110].

3.1.2 The domain homogenization technique for integral contraint

The FEA utilizing H formulation requires integral constraints in order to gratify that the integral of the current density quantity in each HTS winding is equal to a transport current (I_t). Note that the integral of current density induced by screening current is always zero. The primitive H formulation method [109] imposes a certain boundary condition named point-wise integral constraint for the required integral constraints.

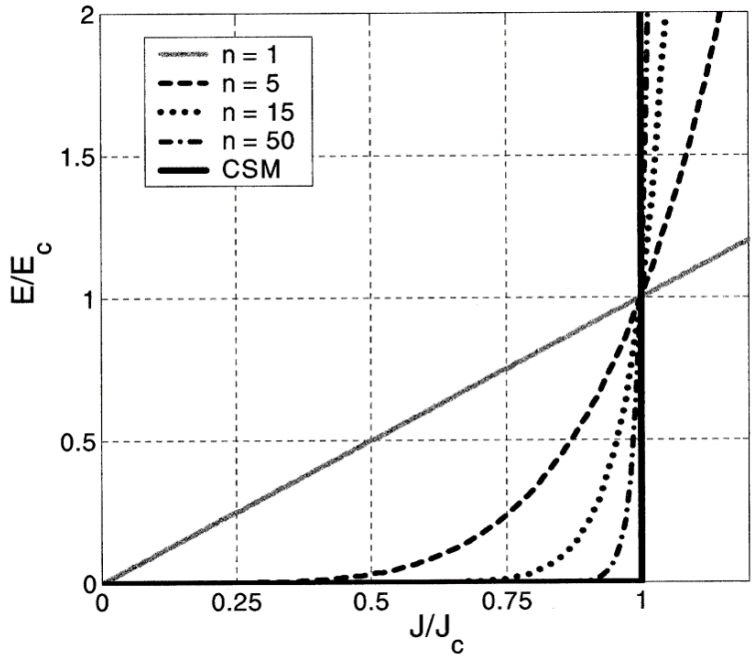

Figure 3.2: The power-law E-J model of an HTS tape. CSM indicates the critical state model of Bean's theory.

Figure 3.3(a) presents individual windings in an HTS coil. There are n_C windings (C_1–C_{n_C}). The point-wise integral constraint of each winding is dictated by:

$$I_t = \int_{C_i} \mathbf{J}_i \cdot d\mathbf{s}_i = \int_{C_i} J_\phi \, drdz, \tag{3.12}$$

where $\mathbf{J}_i$ and $\mathbf{s}_i$ are the current density quantity vector in C_i and the cross-section vector of C_i. It implies that if there are hundreds of windings in an HTS magnet, the corresponding integral constraints are needed for as many as the number of windings. The gigantic computation load is thus required at an actual magnet level with thousands of windings, which is undesirable in the FEA for investigating non-uniform current distribution in an HTS magnet. Hence, the use of the primitive H formulation method using the point form integral constraint was limited to the HTS cable analysis.

To address the computation load issue, Zermeno *et al.* proposed the numerical technique named domain homogenization in 2013 [111]. The key philosophy of the homogenization technique is to consider a stack of HTS tapes or windings as an anisotropic bulk equivalent domain. Figure 3.3(b) presents a schematic drawing of an HTS solenoid coil in a cylindrical coordinate (r,ϕ,z) to describe the domain homogenization. For the domain homogenization technique, the integral constraints of (3.12) can be transformed into (3.13):

$$\frac{I_t}{D} = \int_S J_\phi \, dz, \tag{3.13}$$

where D and S indicate the width of each HTS winding, equivalent to the coil width, and the cross-section of C_{homo}. For instance, there is an HTS magnet that has n_m coils where each coil is wound with m_w windings. For H formulation-based FEA model with the domain homogenization, it requires n_m integral constraints, while that without the homogenization requires $n_m \times m_w$. In conclusion, the domain homogenization technique can substantially ameliorate computation speed by reducing computation load for the FEM simulation utilizing the H formulation.

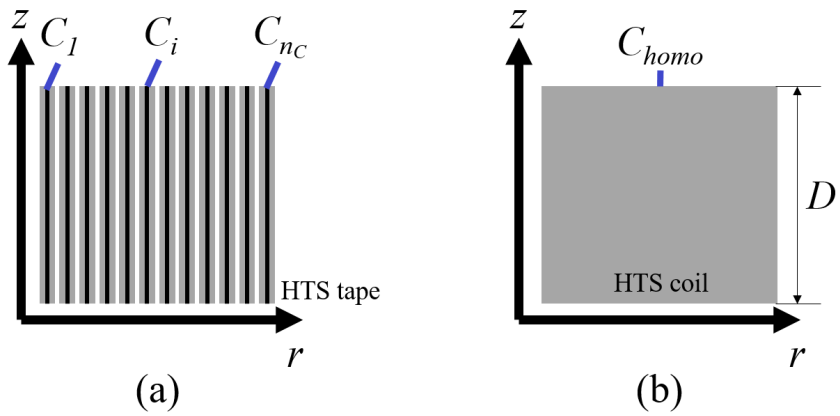

Figure 3.3: Schematic drawing of the domain homogenization technique: (a) the stack of HTS tapes, i.e., an inhomogeneous medium where C_i presents individual conductors; and (b) the homogenized domain, i.e., a homogeneous medium.

3.2 Current and Voltage Behavior Simulation Method

Since an NI HTS coil presents different voltage-current characteristics, which are caused by turn-to-turn bypassing current, various circuit model approaches have been adopted to explain the electromagnetic behaviors of the coil. These circuit models add the bypassing current path to the conventional insulated HTS coil's circuit model that only consists of the inductance and 'index' resistance following the power-law of the superconductivity. In order to characterize this bypassing current path, the contact resistivity R_{ct} of the REBCO conductor is considered. Still, many researchers are trying to figure out which parameters affect contact resistivity or how this value can be controlled. From the contact resistivity, the resistive circuit element named characteristic resistance R_c (or contact resistance) can be calculated as follows:

$$R_c = \frac{R_{ct}}{S_{ct}}, \tag{3.14}$$

where R_c and S_{ct} represent characteristic resistance and contacted surface's area, respectively.

The circuit models for an NI HTS coil can be classified into two models: lumped-circuit model and distributed-circuit model. Each model consists of the inductive element and resistive element. Both models have been experimentally validated by many research groups and applied to the electromagnetic analysis of the coils according to the purpose of analysis.

3.2.1 Lumped-circuit model

The lumped-circuit model for an NI HTS magnet consists of the self-inductance, the 'index' resistance, and the characteristic resistance representing the resistive element of the current path for bypassing current. If the NI HTS magnet including multiple NI HTS coils, the mutual inductances between two particular coils are also considered. Since this model can be constructed with a small number of circuit elements, the fast and accurate analysis can be performed with respect to the terminal voltage of the coil and the central magnetic field. This model has been widely used from the single-pancake coil level to the large-scale magnet level and from normally operating situation to the quench situation. However, the local electromagnetic behaviors cannot be analyzed by this model.

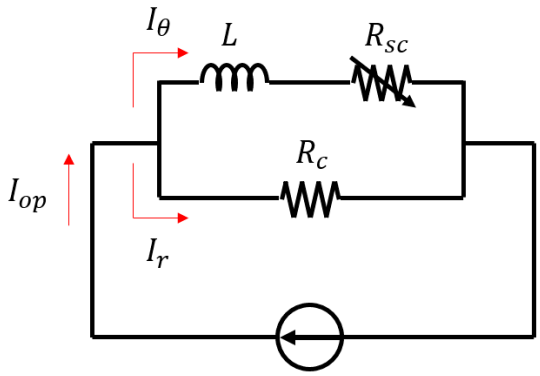

Figure 3.4: Equivalent circuit of an HTS coil or magnet: lumped-circuit model

The governing equation for this circuit model can be calculated as follows:

$$V = L\frac{dI_\theta}{dt} + R_{sc}I_\theta = R_c I_r, \tag{3.15}$$

$$I_{op} = I_\theta + I_r, \tag{3.16}$$

$$\therefore L\frac{dI_\theta}{dI} + (R_{sc} + R_c)I_\theta = R_c I_{op}, \tag{3.17}$$

where L, R_{sc}, V, I_θ, and I_r represent the self-inductance, the 'index' resistance, the terminal voltage, the azimuthal current, and the bypassing current, respectively. By solving this nonlinear ordinary differential equations (ODE), the voltage-current characteristics can be calculated. Since the nonlinearity caused by the 'index' resistance, the solution can be obtained by numerical method such as the backward differentiation formula (BDF) or the Runge-Kutta method.

3.2.2 Distributed-circuit model

The distributed-circuit model subdivides a single coil into smaller elements. Using this model, the local current and voltage behaviors of an HTS coil can be investigated because each element is characterized by the circuit elements. This distributed-circuit network consists of the self-inductances of each element, the mutual inductances between two particular elements, the 'index' resistance, and the characteristic resistance of each bypassing current path. Although this model requires a lot more calculation time than the lumped-circuit model due to the increased number of circuit elements, this model is widely adopted for specific purposes, such as analyzing the local electromagnetic behaviors of the coil with defects, the local electromagnetic behaviors caused by the quench, or non-uniform current density due to screening current.

The so-called turn distributed-circuit model shown in Figure 3.5 is one of commonly used distributed-circuit models It assumes that each turn of the NI HTS coil is defined as a single circuit element in this model. The number of azimuthal current path and bypassing current path are respectively identical to the number of turns. The

governing equation for this circuit model can be presented as follows:

$$\mathbf{I}_\theta = (I_{\theta,1}, I_{\theta,2}, ..., I_{\theta,N})^{tr}, \tag{3.18}$$

$$\mathbf{I}_r = (I_{r,1}, I_{r,2}, ..., I_{r,N})^{tr}, \tag{3.19}$$

$$\mathbf{M} = \begin{pmatrix} L_{1,1} & M_{1,2} & \cdots & M_{1,N} \\ M_{2,1} & L_2 & \cdots & M_{2,N} \\ \vdots & \vdots & \ddots & \vdots \\ M_{N,1} & M_{N,2} & \cdots & L_{N,N} \end{pmatrix}, \tag{3.20}$$

$$\mathbf{R}_{sc} = \begin{pmatrix} R_{sc,1} & 0 & \cdots & 0 \\ 0 & R_{sc,2} & \cdots & 0 \\ \vdots & \vdots & \ddots & \vdots \\ 0 & 0 & \cdots & R_{sc,N} \end{pmatrix}, \tag{3.21}$$

$$\mathbf{R}_c = \begin{pmatrix} R_{c,1} & 0 & \cdots & 0 \\ 0 & R_{c,2} & \cdots & 0 \\ \vdots & \vdots & \ddots & \vdots \\ 0 & 0 & \cdots & R_{c,N} \end{pmatrix}, \tag{3.22}$$

$$\mathbf{M}\frac{d\mathbf{I}_\theta}{dt} + \mathbf{R}_{sc}\mathbf{I}_\theta = \mathbf{R}_c\mathbf{I}_r, \tag{3.23}$$

$$\therefore \mathbf{M}\frac{d\mathbf{I}_\theta}{dt} + (\mathbf{R}_{sc} + \mathbf{R}_c)\mathbf{I}_\theta = \mathbf{R}_c(1, 1, ..., 1)^{tr} I_{op}, \tag{3.24}$$

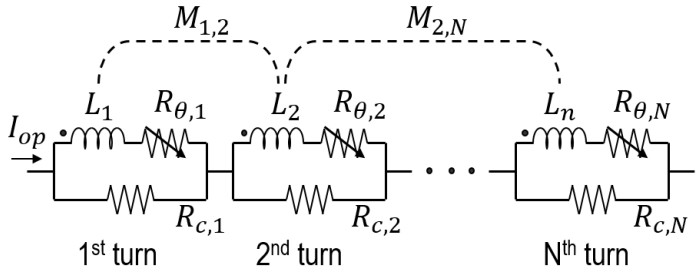

Figure 3.5: Example of the distributed-circuit network model of an HTS coil

where $I_{\theta,i}$, $I_{r,i}$, L_i, $M_{i,j}$, $R_{sc,i}$, $R_{c,i}$, and the superscript tr represent the azimuthal current of the ith turn, the bypassing current of the ithturn, the self-inductance of the ith turn, the mutual inductance between the ith turn and the jth turn, the 'index' resistance of the ith turn, the characteristic resistance of the ith turn, and the transposition, respectively. The solution of these ODE series can be calculated by the numerical method.

Partial equivalent element circuit (PEEC) network model shown in Figure 3.6 may be the most complex circuit model for current and voltage behaviors analysis of an HTS magnet. The model enables the investigation of "microscopic" electromagnetic behaviors, e.g., time-dependent non-uniform current distribution behaviors due to screening current, local current behaviors during quench. However, it is a costly simulation approach to investigate "macroscopic" current and voltage behaviors at the magnet level. In this thesis, details on PEEC model are not provided. Please refer to the following studies [112–114] for details.

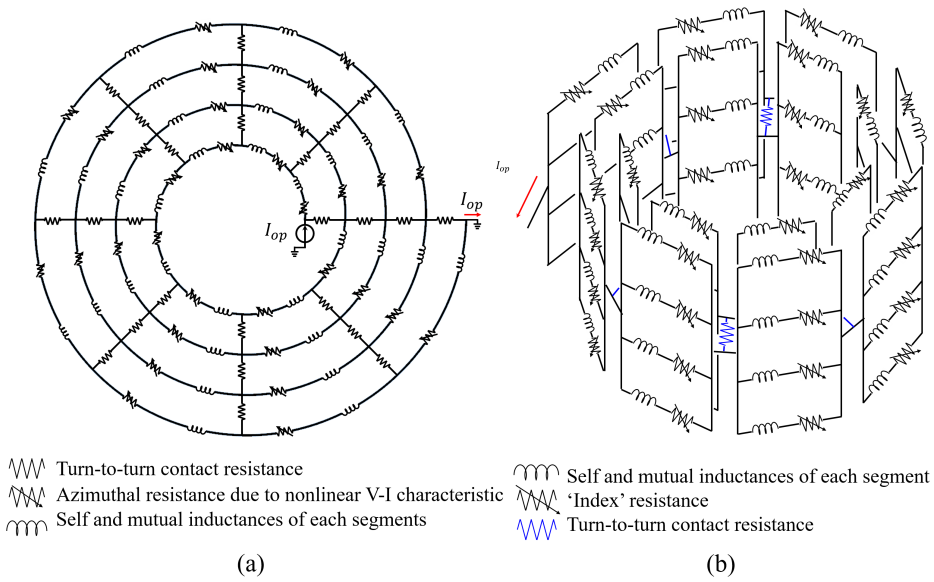

Figure 3.6: Equivalent circuits of an HTS coil with individual partial elements: (a) a two-dimensional model of a partial equivalent element circuit network; (b) a three-dimensional model.

3.3 Nonlinear Inductance Variation Simulation Method

The study on inductance variation can pave the way to assess screening current behaviors, i.e., induction and relaxation, in an HTS magnet. Although many inductance analysis methods have been introduced so far [115–117], it may be assured that they are invalid in analyzing the inductance variation of an HTS coil. The limit of conventional methods is that they essentially assume uniform current distribution in a conductor, which is the inappropriate assumption for an HTS magnet due to screening current. Therefore, nonlinear numerical analysis methods to simulate the inductance variation of an HTS magnet were studied. First, the conventional methods are revisited [115–117] that assume uniform current distribution. Second, two nonlinear inductance calculation methods are discussed.

3.3.1 Garrett's method and energy method

Garrett's inductance calculation method [116] using numerical techniques, i.e., quadrature rules and elliptic integrals, has been widely employed in the inductance analysis of HTS magnet, including self and mutual inductances. The method basically inaugurates calculating mutual inductance between two circular filament conductors assuming uniform current distribution; it may be said as the inductance calculation in the aspect of a "microscopic" view of electromagnetics. The results are summarized below:

$$\mathcal{M}(\mathcal{S},\mathcal{S}) = z\mathcal{M}(\mathcal{S},\mathcal{L}) + \frac{8}{3}\pi \times 10^{-7}\alpha\rho_0 r_1\Big[K - \Big(\frac{2}{\kappa^2} - 1\Big)(K-E)\Big], \tag{3.25}$$

$$\mathcal{M}(\mathcal{S},\mathcal{L}) = 2\pi \times z\Big[r_1(K-E) - \frac{(\alpha-\rho_0)^2}{r_1}(\Pi - K)\Big], \tag{3.26}$$

$$r_2^2 = (\alpha-\rho_0)^2 + z^2, \tag{3.27}$$

$$r_1^2 = (\alpha+\rho_0)^2 + z^2, \tag{3.28}$$

$$\kappa^2 = 4\alpha\rho_0/r_1^2, \tag{3.29}$$

where r_1, r_2, α, and ρ_0 present the maximum and minimum distance from a point on the source ring of radius a to a point on the field ring of radius ρ_0, respectively.

K, E, and Π stand for the complete elliptic integrals of the first, second, and third kinds. $\mathcal{M}$, $\mathcal{S}$, and $\mathcal{L}$ present, respectively, mutual inductance, the shape of solenoid, and the shape of loop. The equations suggest that the inductance is not a function of current but a function of geometry. However, this method is deficient in calculating inductances between coils in an HTS magnet (a stack of HTS coils) since non-uniform current density due to screening current can not be considered.

Meanwhile, in the aspect of "macroscopic" view, the inductance can be calculated by the so-called energy method. For instance, let's assumed that there are two coils (Coil1 and Coil2). Then, if they are close to each other, they interact inductively. Their mutual coupling can be described by means of mutual inductance and self coupling with self inductance. Assuming the linear current system or uniform current distribution in each coil, then self and mutual indutances between two coils can be defined with:

$$L_1 = \frac{\lambda_1}{I_1}, \tag{3.30}$$

$$L_2 = \frac{\lambda_2}{I_2}, \tag{3.31}$$

$$M_{12} = \frac{\phi_{12}}{I_2}, \tag{3.32}$$

$$M_{21} = \frac{\phi_{21}}{I_1}, \tag{3.33}$$

where L_1 and L_2, M_{12} and M_{21}, λ_1 and λ_2, ϕ_{12} and ϕ_{21}, and I_1 and I_2 stand for, respectively, the self inductance of Coil1 and Coil2, the mutual inductance of between two coils, the self coupling of each coil, the mutual coupling between two coils, and the current in Coil and Coil2. Total magnetic energy E_m is given by:

$$\begin{aligned} E_m &= E_{m1}(I_1, I_2) + E_{m2}(I_1, I_2) + E_{m1,2}(I_1, I_2), \\ &= \frac{1}{2}L_1 I_1^2 + \frac{1}{2}L_2 I_2^2 + (\frac{1}{2}M_{12}I_2 I_1 + \frac{1}{2}M_{21}I_1 I_2), \\ &= \frac{1}{2}L_1 I_1^2 + \frac{1}{2}L_2 I_2^2 + M_{21}(\equiv M_{21})I_1 I_2, \end{aligned} \tag{3.34}$$

where E_{m1}, E_{m2}, and $E_{m1,2}$ are magnetic stored energy of Coil1 self coupling, Coil2 self coupling, and Coil1$\leftrightarrow$Coil2 mutual coupling. By using FEM simulation tools,

$E_{m1}(I_1, I_2 = 0)$, $E_{m2}(I_1 = 0, I_2)$, $E_{m1}(I_1, I_2)$, and $E_{m1}(I_1, -I_2)$ can be calculated, then each inductance quantity can be derived with:

$$E_{m1}(I_1, I_2 = 0) = \frac{\mu_0}{2} \int_V \mathbf{H}_1 \cdot \mathbf{H}_1 \, dv, \tag{3.35}$$

$$E_{m2}(I_1 = 0, I_2) = \frac{\mu_0}{2} \int_V \mathbf{H}_2 \cdot \mathbf{H}_2 \, dv, \tag{3.36}$$

$$E_{m1,2}(I_1, I_2) = \frac{\mu_0}{2} \int_V (\mathbf{H}_1 + \mathbf{H}_2) \cdot (\mathbf{H}_1 + \mathbf{H}_2) \, dv, \tag{3.37}$$

$$E_{m1,2}(I_1, -I_2) = \frac{\mu_0}{2} \int_V (\mathbf{H}_1 - \mathbf{H}_2) \cdot (\mathbf{H}_1 - \mathbf{H}_2) \, dv, \tag{3.38}$$

$$L_1 = \frac{2E_{m1}(I_1, I_2 = 0)}{I_1^2}, \tag{3.39}$$

$$L_2 = \frac{2E_{m2}(I_1 = 0, I_2)}{I_2^2}, \tag{3.40}$$

$$M_{12} = \frac{E_{m1,2}(I_1, I_2) - E_{m1,2}(I_1, -I_2)}{2I_1 I_2}, \tag{3.41}$$

where $\mathbf{H}_1$ and $\mathbf{H}_2$ are the magnetic field induction by I_1 and I_2 in each coil, and $\int_V dv$ is a volume integral. Note that $\mathbf{H}_1$ and $\mathbf{H}_2$ are independent on I_2 and I_1.

3.3.2 Modified inductance calculation methods

The conventionally used methods provided above are invalid for an HTS magnet since an HTS magnet is a nonlinear current system and has non-uniform current distribution. Thus, I studied modified methods to calculate inductance with non-uniform current density and a nonlinear system taken into account. The detailed results are provided as follows.

"Microscopic" inductance calculation approach based on Neumann formula

Neumann formula (3.42)–(3.43) is the fundamental formula used for both self and mutual inductances calculation between two conductors in free space that they carry

electric current I_1, and I_2 respectively:

$$M = \frac{1}{I_1 I_2} \int_{A_1} \int_{A_2} m_{12} J_1 J_2 dA_1 dA_2, , \tag{3.42}$$

$$m_{12} = \frac{\mu_0}{4\pi} \int_{C_1} \int_{C_2} \frac{d\vec{l}_1 \cdot d\vec{l}_2}{R}, , \tag{3.43}$$

where $J_1 dA_1$ and $J_2 dA_2$ are a filament carrying current in the first conductor and that in the second conductor. M, μ_0, C_1, C_2, $d\vec{l}_1$, $d\vec{l}_2$, and R stand for, respectively, mutual inductance between two conductors, absolute permeability, the contour of the first conductor, and that of the second conductor, displacement of line vector of the first conductor, displacement of line vector of the second conductor, and the distance between the differential lengths $d\vec{l}_1$ and $d\vec{l}_2$. The direct integration approach of Neumann formula may open a window to the "microscopic" inductance calculation methods, considering non-uniform current distribution with the help of FEA results and a proper discretization procedure.

Figure 3.7 presents: (a) an example of a current density simulation results of an HTS coil; and (b) two arbitrary elements in a cylindrical space. As shown in Figure 3.7(a), it can be derived that non-uniform current density is distributed in one turn of an HTS coil. In addition, with the calculation results of current density, it can be determined that there are n_l finite elements in an arbitrary turn of an HTS magnet and "equivalent" uniform current density in each element as J_i. Then, the inductance of a selected turn can be transformed into (3.44)–(3.45):

$$\begin{aligned} L &= \sum_i \frac{1}{I_i^2} \int_{A_i} \int_{A_i} m_{i,i} J_i J_i dA_i dA_i + \sum_i \sum_{j(\neq i)} \frac{1}{I_i I_j} \int_{A_i} \int_{A_j} m_{i,j} J_i J_j dA_i dA_j \\ &= \sum_i L_i + \sum_i \sum_{j(\neq i)} M_{i,j}, , \end{aligned} \tag{3.44}$$

$$m_{i,j} = \frac{\mu_0}{4\pi} \int_{C_i} \int_{C_j} \frac{d\vec{l}_i \cdot d\vec{l}_j}{R}, \tag{3.45}$$

where A_i, A, ΔA, L_i, and $M_{i,j}$ stand for, respectively, the cross-sectional area of i$^{\text{th}}$ element of a conductor, total area of a conductor, and the area of each element, the self-inductance of i$^{\text{th}}$ element, and the mutual inductance between i$^{\text{th}}$ and j$^{\text{th}}$ and elements.

Meanwhile, in consideration of thin tape configuration of HTS tape, $M_{i,j}$ can be expressed with (3.46)–(3.47) [112]:

$$M_{ij} = \frac{\mu_0 r_i r_j}{4\pi w_i w_j} \int_{d\lambda}^{d\lambda+w_j} \int_{\Theta_j}^{\Theta_j+\Delta\Theta} \int_{0}^{w_i} \int_{\theta_i}^{\theta_i+\Delta\theta} \frac{\cos(\theta-\Theta)}{R_{ij}(z,Z)} d\theta dz d\Theta dZ, \quad (3.46)$$

$$R_{ij}(z,Z) = \sqrt{r_i^2 + r_j^2 - 2r_i r_j \cos(\theta-\Theta) + (z-Z)^2}, \quad (3.47)$$

where M_{ij}, $d\lambda$, w_i, w_j, θ_i, $\Delta\theta_i$, Θ_j, $\Delta\Theta_j$, r_i, r_j, and R_{ij} stand for, respectively, the mutual inductance between two partial elements, the axial distance between bottom of two partial elements, the width of the first partial element, that of the second partial element, the initial angular position of the first partial element, the angular interval in the first partial element, the initial angular position of the second partial element, the angular interval in the second partial element, the radial position of the first partial

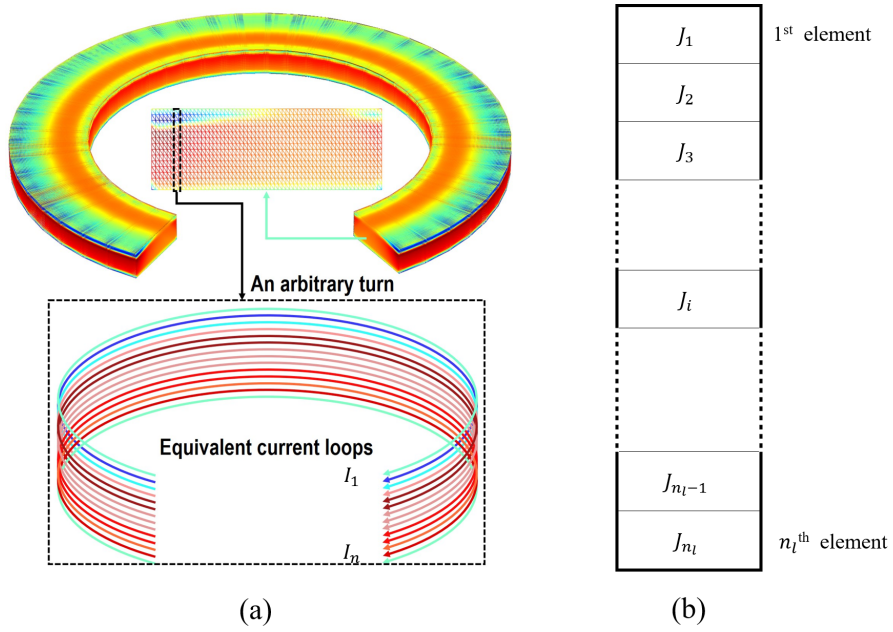

Figure 3.7: (a) Example of a current density simulation results of an HTS coil. (b) Schematic drawing of an arbitrary turn which are segmented by n_l elements and the corresponding current density.

element, that of the second partial element, and the distance between two elements, Figure 3.8. The discretization process is needed to compute (3.46)–(3.47) with following quantities: the number of discretization of angular variables, and the number of discretization of axial variables. Then, (3.46) becomes (3.48) with (3.49)–(3.50):

$$M_{ij} = \sum_{n_Z=1}^{Nz} \sum_{n_z=1}^{Nz} \sum_{n_\theta=1}^{N_\theta} \sum_{n_\Theta=1}^{N_\theta} \kappa_{ij}(n_z, n_Z, n_\theta, n_\Theta)\delta_{ij}, \tag{3.48}$$

$$\kappa_{ij}(n_z, n_Z, n_\theta, n_\Theta) = \frac{\mu_0 r_i r_j}{4\pi w_i w_j} \frac{\cos(\theta[n_\theta] - \Theta[n_\Theta])}{R_{ij}(z[n_z], Z[n_Z])}, \tag{3.49}$$

$$\delta_{ij} = \frac{w_i \cdot w_j \cdot \Delta\theta_i \cdot \Delta\Theta_j}{N_z \cdot N_z \cdot N_\theta \cdot N_\theta}, \tag{3.50}$$

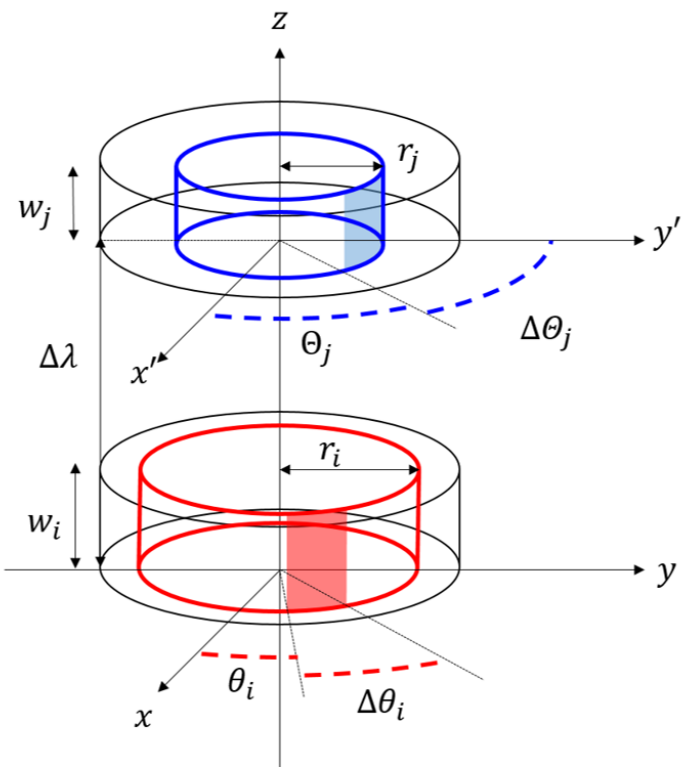

Figure 3.8: Schematic drawing two elements placed in a space. Two elements (shaded areas with blue and red) are the target to calculate mutual inductance.

where $z[n_z]$, $Z[n_Z]$, $\theta[n_\theta]$, and $\Theta[n_\Theta]$ are, respectively, the n_z^{th} discretized axial position value on interval $[0, w_i]$, the n_Z^{th} discretized axial position value on interval $[d\lambda, d\lambda + w_j]$, the n_θ^{th} discretized angular position value on interval $[\theta_i, \theta_i + \Delta\theta]$, and the n_Θ^{th} discretized angular position value on interval $[\Theta_j, \Theta_j + \Delta\Theta]$.

With this numerical computation method transformed from quadruple integral, one can expect there are two things to be discussed. First, the discretization process has a truncation error, which is inevitable. Second, this approach requires an immense computation load due to the complexity of the high order loop computation algorithm. Here this thesis thus proposes the basic idea to develop an improved method for a fast computation as well as truncation error mitigation.

It is possible to conduct analytic integral with respect to axial variables, z and Z—it is simple but no one has made an effort to develop this integral to our best knowledge. The consequent results of the first one is as follows:

$$M_{ij}^* = \frac{\mu_0 r_i r_j}{4\pi w_i w_j} \int_{\Theta_j}^{\Theta_j+\Delta\Theta} \int_{\theta_i}^{\theta_i+\Delta\theta} \cos(\theta - \Theta) \left[\left[f(z, Z) \right]_{q_2^i}^{q_1^i} \right]_{s_2^j}^{s_1^j} d\theta d\Theta, \tag{3.51}$$

$$f(z, Z) = R_{ij}(z, Z) + (Z - z)\ln(R_{ij}(z, Z)) + z - Z, \tag{3.52}$$

$$\left[\left[f(z, Z) \right]_{q_2}^{q_1} \right]_{s_2}^{s_1} \equiv \sum_{a=1}^{2} \sum_{b=1}^{2} (-1)^{a+b} f(q_a, s_b), \tag{3.53}$$

where q_1^i, q_2^i, s_1^j, and s_2^j are, respectively, w_i, 0, $\Delta\lambda + w_j$, and $\Delta\lambda$. The order of integral of (3.51) becomes half compared to that of (3.48). With these results, (3.51) is able to be transformed into digital form of (3.54) with (3.55)–(3.57),

$$M_{ij}^* = \sum_{n_\theta=1}^{N_\theta} \sum_{n_\Theta=1}^{N_\theta} \kappa_{ij}^*(n_\theta, n_\Theta) \delta_{ij}^*, \tag{3.54}$$

$$\kappa_{ij}^*(n_\theta, n_\Theta) = \frac{\mu_0 r_i r_j}{4\pi w_i w_j} \cos(\theta[n_\theta] - \Theta[n_\Theta]) \left[f(z, Z) \right]_{q_2^i}^{q_1^i}, \tag{3.55}$$

$$\delta_{ij}^* = \frac{\Delta\theta_i \cdot \Delta\Theta_j}{N_\theta \cdot N_\theta}, \tag{3.56}$$

$$\left[f(z, Z) \right]_{q_2}^{q_1} \equiv \sum_{a=1}^{2} (-1)^a f(q_a). \tag{3.57}$$

There are a few singularities of (3.54) when $R_{ij}(z-Z)$ becomes zero. It means that two partial elements become identical one element, which means that $r_i = r_j$, $w_i = w_j$, $\theta_i = \Theta_j$, $\Delta\theta_i = \Delta\Theta_j$, and $d\lambda = 0$, but this singularity is able to be manipulated by adding a particular "correction" value with:

$$\begin{aligned}\Delta L &= \frac{\mu_0}{6\pi a^2}\left[3a^2 l \ln\left(\frac{l+\sqrt{l^2+a^2}}{a}\right) - (l^2+a^2)^{\frac{3}{2}}\right. \\ &\quad \left. +3l^2 a \ln\left(\frac{a+\sqrt{l^2+a^2}}{l}\right) + l^3 + a^3\right], \end{aligned} \tag{3.58}$$

where $a = w_i = w_j$, and $l = r_i\Delta\theta_i/N_\theta$. This value is excatly same with a self inductance of a partial element. Then, with the results of (3.54)–(3.57), both self and mutual inductances are able to be fastly calculated. There are two advantages with this double loops computation method of (3.54). First, calculation accuracy can be improved since the analytic integration is performed. This is based on the fact that the issue of truncation errors from discretization for the numerical approach becomes resolved. Second, the complexity is drastically ameliorated by half. It obviously addresses the issue of the conventional numerical integral approach requiring immense computation load. Meanwhile, one can expect that additional integral with respect to angular position, θ and Θ, but it is, unfortunately, unavailable. It might be possible when one discovers a method to apply the use of quadrature rules, e.g., the Gaussian-Legendre quadrature rule, for calculation of M_{ij} with an assumption that the formulation inside double integral is well-approximated to an analytic combination of "series". However, note that if one complete turn is the target of inductance calculation, the use of the quadrature rule proposed by Garrett is still valid.

"Macroscopic" inductance calculation approach based on energy method

The HTS magnet system is not a linear system but a nonlinear system since there are magnetic hysteresis and screening current. Hence, "equivalent" quantities of self and mutual inductances should be re-defined, and the result can be described with (3.59)–(3.62) when assuming that there are two HTS coils (let's say HTS-Coil1 and

HTS-Coil2)—here the asterisk symbol (*) is used to indicate nonlinear current system:

$$L_1^*(I_1, I_2) = \frac{\partial \lambda_1^*}{\partial I_1}, \tag{3.59}$$

$$L_2^*(I_1, I_2) = \frac{\partial \lambda_2^*}{\partial I_2}, \tag{3.60}$$

$$M_{21}^*(I_1, I_2) = \frac{\partial \phi_{21}^*}{\partial I_1}, \tag{3.61}$$

$$M_{12}^*(I_1, I_2) = \frac{\partial \phi_{12}^*}{\partial I_2}, \tag{3.62}$$

where L_1^* and L_2^*, M_{12}^* and M_{21}^*, λ_1^* and λ_2^*, ϕ_{12}^* and ϕ_{21}^*, and I_1 and I_2 stand for, respectively, the equivalent self inductance of HTS-Coil1 and HTS-Coil2, the equivalent mutual inductance of between HTS-Coil1 and HTS-Coil2, the equivalent self coupling of each HTS coil, the equivalent mutual coupling between two HTS coils, and the current flowing in HTS-Coil1 and HTS-Coil2. Then, the total energy of two HTS coils system, E_m^*, is described with (3.63):

$$E_m^* = E_{m1}^*(I_1, I_2) + E_{m2}^*(I_1, I_2) + E_{m1,2}^*(I_1, I_2) \tag{3.63}$$

Assuming that the simulation results of two HTS coils are given, the integration of magnetic stored energy density in a FEA program can be used to obtain E_{m1}^*, E_{m2}^*, and $E_{m1,2}^*$. Figure 3.9 presents an example of simulated current density in two HTS coils. With the calculation results, E_{m1}^*, E_{m2}^*, and $E_{m1,2}^*$ are described with (3.64)–(3.68) assuming that $\mathbf{H}_1^*(J_1, J_2)$ and $\mathbf{H}_2^*(I_1, I_2)$ are induced by the current density in HTS-Coil1 (J_1) and HTS-Coil2 (J_2) when I_1 flows in the HTS-Coil1 and I_2 flows in the HTS-Coil2:

$$E_{m1}^*(I_1, I_2) = \frac{\mu_0}{2} \int_V \mathbf{H}_1^* \cdot \mathbf{H}_1^* \, dv, \tag{3.64}$$

$$E_{m2}^*(I_1, I_2) = \frac{\mu_0}{2} \int_V \mathbf{H}_2^* \cdot \mathbf{H}_2^* \, dv, \tag{3.65}$$

$$E_{1,2}^*(I_1, I_2) = \frac{\mu_0}{2} \int_V (\mathbf{H}_1^* + \mathbf{H}_2^*) \cdot (\mathbf{H}_1^* + \mathbf{H}_2^*) \, dv, \tag{3.66}$$

$$E_{1,2}^*(-I_1, I_2) = \frac{\mu_0}{2} \int_V (-\mathbf{H}_1^* + \mathbf{H}_2^*) \cdot (-\mathbf{H}_1^* + \mathbf{H}_2^*) \, dv, \tag{3.67}$$

$$E^*_{m1,2}(I_1, I_2) = \frac{E^*_{1,2}(I_1, I_2) - E^*_{1,2}(-I_1, I_2)}{2}, \tag{3.68}$$

Here Figure 3.9(a) and (d) shows the calculation results from (3.68), while Figure 3.9(b) from (3.65) and Figure 3.9(c) from (3.66).

With (3.64)–(3.68), the effective flux linkage, including the self and mutual coupling, can be derived. As shown in Figure 3.10, there are two HTS coils, and the current distribution in the coils are given when (a) t and (b) $t + \Delta t$. Then, the linkage between two coils can be calculated with the following equations (3.69)–(3.71):

$$\lambda^*_1 = \lim_{\Delta t \to 0} \frac{E^*_{m1}(I_1 + \Delta I_1, I_2) - E^*_{m1}(I_1, I_2)}{\Delta I_1} = \frac{\partial E^*_{m1}(I_1, I_2)}{\partial I_1}, \tag{3.69}$$

$$\lambda^*_2 = \lim_{\Delta t \to 0} \frac{E^*_{m2}(I_1, I_2 + \Delta I_2) - E^*_{m2}(I_1, I_2)}{\Delta I_2} = \frac{\partial E^*_{m2}(I_1, I_2)}{\partial I_2}, \tag{3.70}$$

$$\begin{aligned}
\phi^*_{12} &= \lim_{\Delta t \to 0} \frac{E^*_{m1,2}(I_1, I_2 + \Delta I_2) - E^*_{m1,2}(I_1, I_2)}{\Delta I_2} = \frac{\partial E_{m1,2}(I_1, I_2)}{\partial I_2}, \\
&= \lim_{\Delta t \to 0} \frac{E^*_{m1,2}(I_1 + \Delta I_1, I_2) - E^*_{m1,2}(I_1, I_2)}{\Delta I_1} = \frac{\partial E_{m1,2}(I_1, I_2)}{\partial I_1}, \\
&= M^*_{21}(I_1, I_2) I_1 = M^*_{12}(I_1, I_2) I_2,
\end{aligned} \tag{3.71}$$

where ΔI_1 and ΔI_2 stand for $I_1(t + \Delta t) - I_1(t)$ and $I_2(t + \Delta t) - I_2(t)$. By using (3.69)–(3.71), it can be concluded that the inductance can be derived. This inductance calculation method based on the energy method can be expanded to multi-coil system. The equivalent inductances are also calculated with (3.72)–(3.74) [118]:

$$\frac{dE^*_{m1}(I_1, I_2)}{dt} = \frac{d\lambda^*_1}{dt} I_1 = L^*_1 \frac{dI_1}{dt} I_1 = \frac{1}{2} L^*_1 \frac{d(I_1^2)}{dt}, \tag{3.72}$$

$$\frac{dE^*_{m2}(I_1, I_2)}{dt} = \frac{d\lambda^*_2}{dt} I_2 = L^*_2 \frac{dI_2}{dt} I_2 = \frac{1}{2} L^*_2 \frac{d(I_2^2)}{dt}, \tag{3.73}$$

$$\frac{dE^*_{m1,2}(I_1, I_2)}{dt} = \frac{d\phi^*_{12}}{dt} I_1 = \frac{d\phi^*_{12}}{dt} I_2 = M^*_{12} \frac{d(I_1 I_2)}{dt}. \tag{3.74}$$

In consideration of the independency between I_1 and I_2, (3.72)–(3.74) can be transformed into (3.75)–(3.77):

$$L^*_1 = \frac{2dE^*_m}{d(I_1^2)}, \tag{3.75}$$

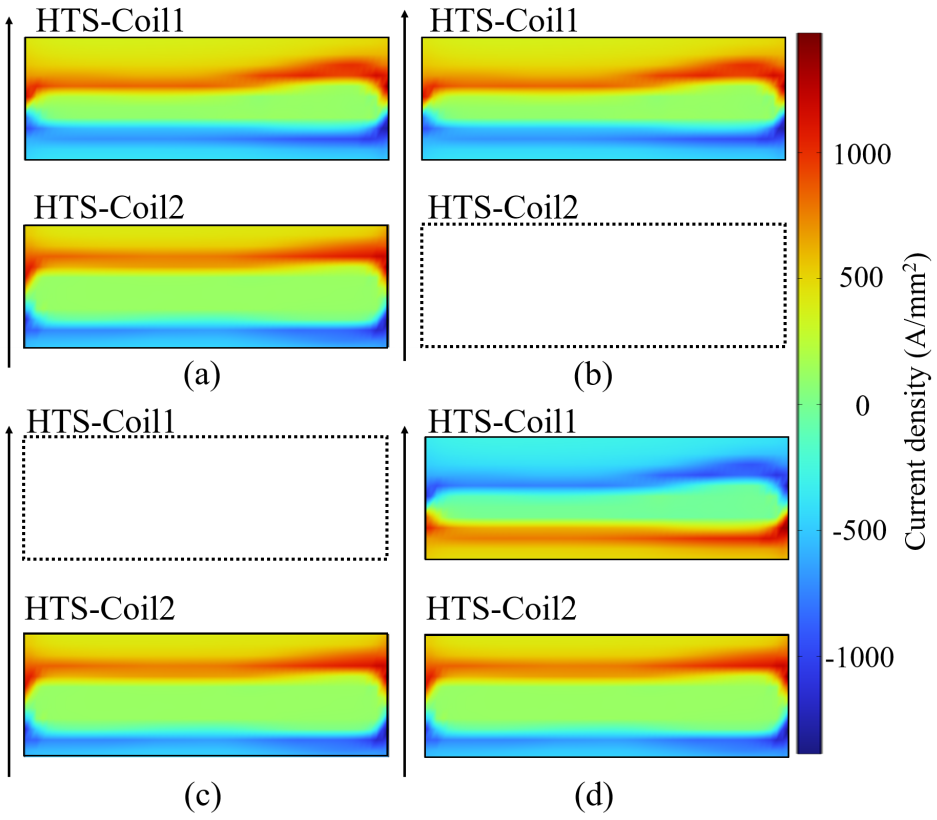

Figure 3.9: Simulation results of current density in two HTS-Coils for calculating M_{12}^* with (a) and (d), L_1^* with (b), and L_2^* with (c).

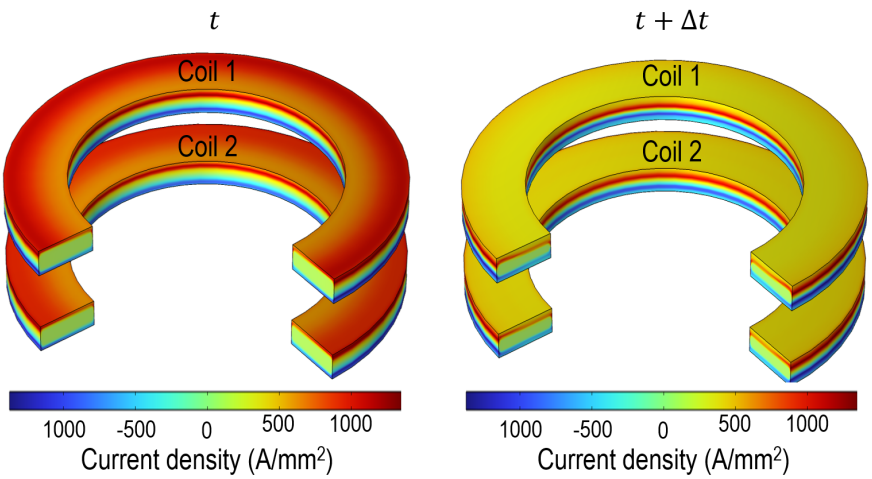

(a) (b)

Figure 3.10: Example of two coil systems with non-uniform current density. (a) presents the non-uniform current distribution at t and (b) at $t + \Delta t$.

$$L_2^* = \frac{2dE_m^*}{d(I_2^2)}, \tag{3.76}$$

$$M_{12}^* = \frac{dE_m^*}{d(I_1 I_2)}. \tag{3.77}$$

To sum up, the current-derivative stored energy implies the consequential effects caused by screening current relaxation in principle. Therefore, measuring and analyzing inductive voltage change due to the relaxation may be an appropriate approach for predicting screening current behaviors induced by an HTS magnet.

3.4 Spatial Harmonic Coefficients Simulation Method

Field quality is an important magnetic performance of an HTS magnet for NMR and MRI applications since it determines the resolution of their signals (see chapter 2). If the field quality does not satisfy the required specifications of the main magnets for NMR and MRI applications, compensation techniques, e.g., passive and active shimming techniques, are essentially utilized. The main aim of using the compensation

technique is to reduce the magnitude of all the harmonic coefficients of spatial magnetic fields in a bore of NMR and MRI applications. Accordingly, the estimation of field uniformity created by an HTS magnet in the design stage may be a necessary analysis for NMR and MRI applications. The harmonic analysis has been widely used to estimate the field quality of spatial magnetic fields in a magnet bore. However, conventional methods have assumed uniform current distribution in the main magnet for NMR and MRI applications. Hence, they are limited to analyzing spatial magnetic fields created by an HTS magnet due to non-uniform current density by screening current. This thesis thus provides nonlinear numerical analysis methods to estimate harmonic coefficients with non-uniform current density taken into account. The conventional analysis method is revisited [108], then the details of the nonlinear numerical analysis method named "Segmentation method" are presented in this thesis.

3.4.1 Legendre expansion to describe spatial magnetic fields

The Maxwell equations suggest an idea to define the uniformity of the spatial magnetic field in a mathematical manner. Let's assume that there are no electromagnetic sources, i.e., charge, current, and time-varying electromagnetic field quantities. Then, the equation of magnetic fields can be simplified with the second-order partial differential equations in the form of Laplace's equation:

$$\nabla^2 \mathbf{H} = 0. \tag{3.78}$$

Fortunately, the equation can be resolved with analytic solutions within common coordinate systems, e.g., cartesian, cylindrical, and spherical coordinate systems. Especially for the spherical coordinate system (r, θ, ϕ), the Laplace's equation of magnetic field quantity is decomposed with:

$$\nabla^2 H = \frac{1}{r}\frac{\partial}{\partial r}\left(r\frac{\partial H}{\partial r}\right) + \frac{1}{r^2 \sin\theta}\frac{\partial}{\partial \theta}\left(\sin\theta \frac{\partial H}{\partial \theta}\right) + \frac{1}{\sin^2\theta}\frac{\partial^2 H}{\partial \phi^2}. \tag{3.79}$$

By using the separation of variables, each magnetic field quantity can be defined by the product of corresponding basis function to each coordinate variable, e.g., $H(r, \theta, \phi) =$

$R(r)\Theta(\theta)\Phi(\phi)$. Note that, in mathematics, the solutions of Laplace's equation within a spherical coordinate are commonly called spherical harmonics, while those within a cylindrical coordinate are cylindrical harmonics. Traditionally, analysis of superconductor magnets for MR applications has been based on spherical harmonics. The target field of the analysis is only the z-component of magnetic field quantity, i.e., H_z or B_z.

In this thesis, the so-called closed-form expression is useful for analyzing field uniformity of spatial magnetic fields created by a superconductor magnet. Figure 3.11 presents a cross-sectional view of a solenoid magnet [108]. In spherical coordinates (r,θ,ϕ), where θ is polar angle and ϕ is azimuthal angle, the magnetic field in the

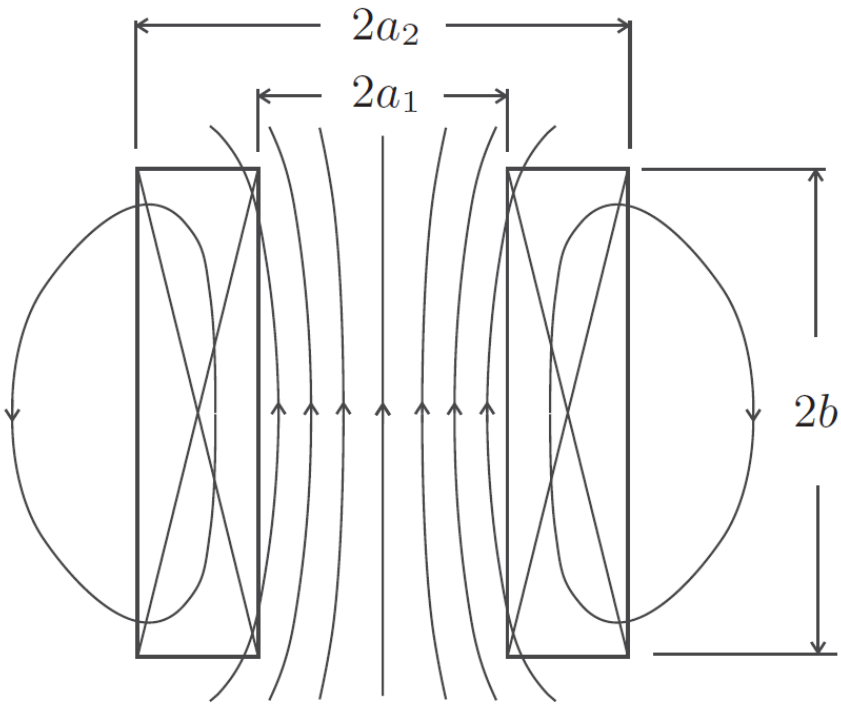

Figure 3.11: Cross-sectional view of a solenoidal coil; $2a_1$, $2a_2$, and $2b$ present, respectively, winding inner diameter, outer diameter, and total height.

axial (z) direction, $H_z(r,\theta,\phi)$ in a free space without any electromagnetic sources, i.e., currents and charges, is expressed by:

$$H_z(r,\theta,\phi) = \sum_{n=0}^{\infty}\sum_{m=0}^{n} r^n(n+m-1)P_n^m(u)\big(A_n^m\cos(m\phi)+B_n^m\sin(m\phi)\big), \quad (3.80)$$

where $P_n^m(u)$ is the set of Legend polynomials (for m=0) and associated Legendre functions (for m>0), and $u = \cos(\theta)$. A_n^m and B_n^m are constants. Especially for the solenoidal systems, the expanded expression of magnetic fields is simplified for $H_z(z)$ in a cylindrical coordinate (r,ϕ,z) to:

$$H_z(z) = \sum_{n=0}^{\infty} z^n(n+1)A_n^0 \quad (3.81)$$

while $H_z(r)$ to:

$$H_z(r) = \sum_{n=0}^{\infty}\sum_{m=0}^{n} r^n(n+m-1)P_n^m(0)A_n^m. \quad (3.82)$$

With this analytic approach for describing the spatial magnetic fields created by a solenoid magnet, the so-called "Garrett" method was first reported by M. W. Garrett in the early 1960s to calculate the harmonic coefficients of spatial magnetic fields [119]; it is one of the well-defined approaches to calculate spatial harmonic coefficients of magnetic fields generated by an "ideal" solenoid, i.e., a magnet having a uniform current density within its winding [120–127].

In this method, the n^{th} order zonal harmonic coefficient of axial magnetic fields (B_z) generated by a solenoid magnet with uniform current density can be expressed as (3.83):

$$\frac{\partial^m B_z}{\partial z^m} = \frac{0.2\pi}{r_0^{m+1}}\sum_{n=0}^{\infty}\frac{(n+m)!}{n!}q_{n+m+1}r^n P_n(\cos\theta), \quad (3.83)$$

where r, r_0, q_{n+m+1}, and P_n stand for, respectively, radial distance in spherical coordinate (r, ϕ, θ), a reference length to be adopted for domain normalization, a numerical coefficient which is related to source current distribution in space, and the Legendre polynomial of order n. More details on this approach may be available in his other papers. As demonstrated in his earlier paper, Garrett's method is well-known for its

accurate calculation of even high order harmonic coefficients defined at the origin of magnetic fields. However, this approach has the critical issue that the non-uniform current density in a magnet can not be considered, which implies that the use of the harmonic analysis is limited to an HTS magnet.

3.4.2 "Segmentation" method to consider non-uniform current density

For HTS solenoid magnets, the uniform current density assumption is invalid due to screening current, as expected. However, to our best knowledge, few studies have been addressed the impact of screening current on spatial magnetic fields. Although a numerical analysis has been widely performed through a virtual field mapping of spatial magnetic fields created by screening current, a numerical method with a direct way to calculate harmonic coefficients created by current sources in an HTS magnet, including uniform transport current and non-uniform screening current, has not been studied yet so far. As a result, a numerical method to calculate spatial harmonic coefficients of magnetic fields generated by given spatially distributed currents, e.g., both transport and screening currents, of an HTS magnet in cylindrical coordinate (r,ϕ,z) was thus proposed; it is named "segmentation" method. Now, this thesis provides, first, the key philosophy of the segmentation method and then a case study to validate its effectiveness.

The segmentation method consists of two steps. First, it is needed to obtain equivalent loop currents from given current densities in an analysis domain. Second, with the loop currents, it is possible to calculate harmonic coefficients of spatial magnetic fields from the equivalent loop currents. Figure 3.12 shows a schematic drawing of a 2D axisymmetric "domain", where current distributions are calculated. In Figure 3.12, the domain consists of a total of $2 \times p \times q$ "segments". Each triangular segment has three nodes, a, b, and c, at which the respective current densities, J_a, J_b, and J_c, can be obtained from given current densities. Then, the equivalent current (I_ϕ^{equiv}) flowing

at the center of mass of each segment, G, may be obtained by (3.84):

$$I_{\phi}^{equiv} = J_a S_a + J_b S_b + J_c S_c, \tag{3.84}$$

where the subscripts a, b, and c are three nodes of a triangle segment, J is current density, and S is area of the sub-triangle in Figure 3.12.

Harmonic gradients of axial magnetic fields (B_z^{loop}) from an ideal "loop" current can be calculated using associated Legendre polynomials in spherical coordinates (r, θ, ϕ) by (3.85):

$$B_z^{loop}(\mathbf{r}) = \sum_{n=0}^{\infty} \left[I_{\phi} \frac{\mu_0 \sin\alpha}{2 r_0^{n+1}} P_{n+1}^1(\cos\alpha) \right] r^n P_n^0(\cos\theta), \tag{3.85}$$

where $\boldsymbol{r}$, P_n^m, μ_0, I_{ϕ}, r_0, and α are, respectively, position vector in spherical coordinate, associated Legendre polynomial of degree n and order m, permeability of free space, magnitude of loop current, radius r_0 of the loop current , and polar angle of the field

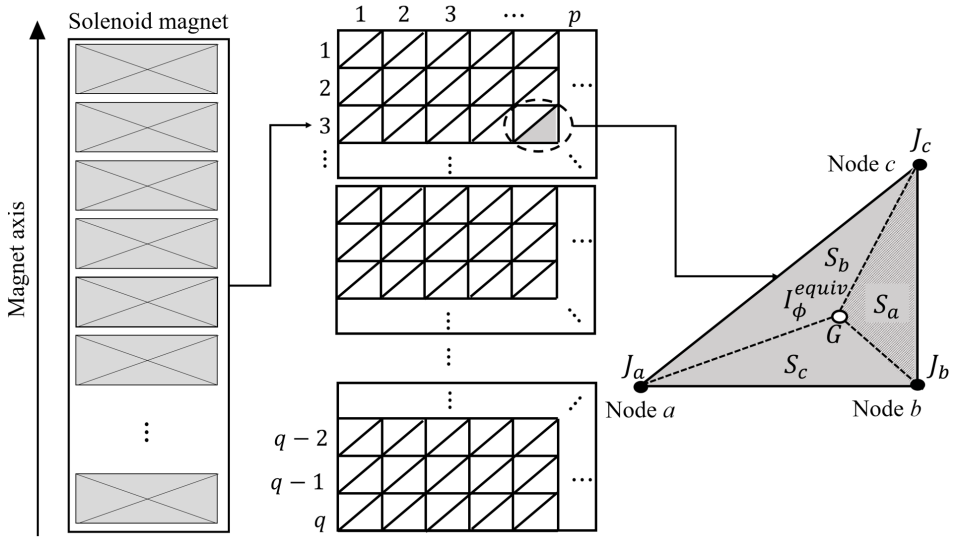

Figure 3.12: Schematic diagram to present "segmentation" method for an HTS magnet.

mapping point. Especially, on the z axis, (3.33) becomes:

$$B_z^{loop}(z) = \sum_{n=0}^{\infty} \Big[\frac{\mu_0 I_\phi \sin\alpha}{2r_0^{n+1}} P_{n+1}^1(\cos\alpha) \Big] z^n = \sum_{n=0}^{\infty} \frac{Zn}{n!}\, z^n, \tag{3.86}$$

where Zn indicates the n$^{\text{th}}$ order zonal harmonic coefficient. Finally, the total harmonic coefficients of axial magnetic fields from all the equivalent loop currents can be obtained by superposition as presented in (3.87):

$$\begin{aligned} B_z^{loops}(z) &= \sum_{seg=0}^{2\times p\times q} \sum_{n=0}^{\infty} (\frac{Zn_{seg}}{n!})\, z^n, \\ &= \sum_{seg=0}^{2\times p\times q} \sum_{n=0}^{\infty} \Big[\frac{\mu_0 I_{seg} \sin\alpha_{seg}}{2r_{seg}^{n+1}} P_{n+1}^1(\cos\alpha_{seg}) \Big] z^n, \end{aligned} \tag{3.87}$$

where subscript seg, I_{seg}, r_{seg}, α_{seg}, and Zn_{seg} stand for, respectively, a segment index, the magnitude of current, radius, polar angle, and the n^{th} order zonal harmonic coefficient.

Table 3.2 presents key parameters of a solenoid magnet arbitrarily chosen for verification of our segmentation method. The magnet consists of a stack of 12 single pancake coils wound with HTS tapes, 4.1 mm wide and 0.12 mm thick. The inner radius, outer radius, and height are, respectively, 50 mm, 59.36 mm and 51.4 mm. 0.2 mm pancake-to-pancake spacers are assumed. Both p and q in Figure 3.12 are ranged 10 - 1000 in this case study. The key idea is to compare spatial harmonic coefficients from the solenoid magnet in Table 3.2 that are calculated using the "Garrett" method, the "Inverse" method based on field measurement results from finite element analysis (FEA), and the "Segmentation (Seg.)" method. Table 3.3 summarizes the results of zonal harmonic coefficients calculated with the three different methods, and segmentation dependent harmonic coefficient errors up to the 10$^{\text{th}}$ order where both p and q are 10, 100, and 1000. Here the harmonic coefficient error is defined in (3.88):

$$\epsilon_n = |\frac{Zn^{Garrett} - Zn^{Proposed}}{Zn^{Garrett}}|, \tag{3.88}$$

where ϵ_n, $Zn^{Garrett}$, and $Zn^{Proposed}$ are, respectively, the n^{th} order zonal harmonic

coefficient error, the n^{th} order zonal harmonic coefficient calculated by the Garrett's method, and that by the proposed method.

The so-called "parameter sweep" technique is adopted to investigate the difference between the two methods, Garrett and Segmentation, depending on the number of segmentation, p and q in Figure 3.12. With comparison results between "Garrett" and "Inverse" shown in Table 3.3, low order coefficients ($Z0, Z2, Z4$) show good agreement, while high order coefficients ($Z6, Z8, Z10$) show some discrepancies. This may present a limit of the "Inverse" method not to be able to calculate high order coefficients. Good agreement in the results between the two methods, "Garrett" and "Seg-

Table 3.2: Key Parameters of a solenoid magnet

Magnet parameters	Unit	
Conductor width, w	[mm]	4.10
Conductor thickness, th	[mm]	0.12
Inner radius, a_1	[mm]	50
Outer radius, a_2	[mm]	59.36
The number of single pancake (SP)		12
SP - SP spacer	[mm]	0.20
Total height, $2b$	[mm]	51.40
The aspect ratio of magnet cross-section		5.49
Operating current, I_{op}	[A]	100
Uniforn current density, J_{uni}	[A/mm^2]	203.25
Simulation parameters	Unit	
The number of segmentation, p and q	[#]	10 - 1000

Table 3.3: Calculation Results of Spatial Harmonic Coefficients and Segmentation Dependent Spatial Harmonic Coefficient Errors

Coeffs.	Garrett	Inverse	Seg.(p=q=1000)
$Z0$ [T]	0.974	0.974	0.974
$Z2$ [T/cm^2]	$-0.657 \cdot 10^{-1}$	$-0.657 \cdot 10^{-1}$	$-0.657 \cdot 10^{-1}$
$Z4$ [T/cm^4]	$0.155 \cdot 10^{-1}$	$0.154 \cdot 10^{-1}$	$0.155 \cdot 10^{-1}$
$Z6$ [T/cm^6]	$-0.295 \cdot 10^{-2}$	$-0.486 \cdot 10^{-2}$	$-0.295 \cdot 10^{-2}$
$Z8$ [T/cm^8]	$-0.894 \cdot 10^{-2}$	$0.476 \cdot 10^{-1}$	$-0.894 \cdot 10^{-2}$
$Z10$ [T/cm^{10}]	$0.334 \cdot 10^{-1}$	-0.602	$0.334 \cdot 10^{-1}$

Errors	Garrett vs. Segmentation Method		
	p=q=10	p=q=100	p=q=1000
ϵ_0 [ppm]	379.9	4.481	0.03289
ϵ_2 [ppm]	1374	16.26	0.1459
ϵ_4 [ppm]	1438	17.17	0.1428
ϵ_6 [ppm]	9325	108.1	1.103
ϵ_8 [ppm]	25890	303.2	3.105
ϵ_{10} [ppm]	14700	174.5	1.786

mentation (Seg.)", in Table 3.3, however, may verify our segmentation method to calculate spatial harmonic coefficients of magnetic fields for a given current distribution.

Figure 3.13 shows calculated zonal harmonic coefficient errors up to the 10$^{\text{th}}$ order. There is an optimal ratio between p and q in terms of calculation accuracy. the optimal ratio at the point was found where error is the smallest in all the graphs plotted in Figure 3.13, and obtained the fact that the average value is 5.5. This ratio is similar to the aspect ratio of the cross-section of the chosen magnet indicated in Table 3.2.

With this analysis, it can be concluded that the segments should be in the shape of right-angle isosceles triangles to calculate spatial harmonic coefficients in case where our segmentation method is applied. Meanwhile, due to the axially long configuration of the magnet, the errors show less dependency on p rather than q for p of >300.

Further study was performed an HTS magnet. First, to obtain equivalent loop cur-

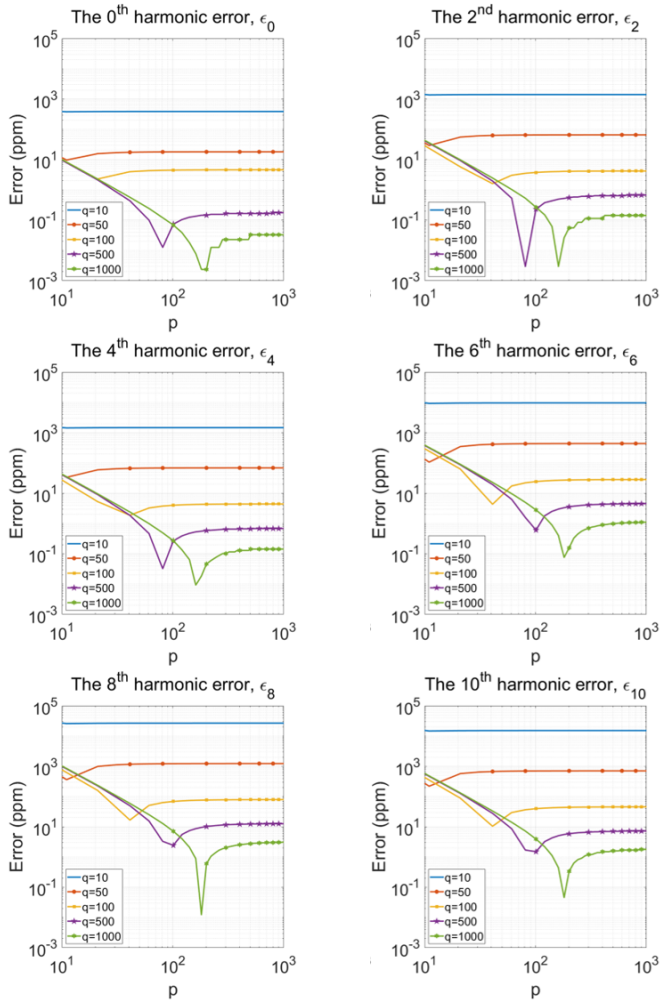

Figure 3.13: Calculation results of the number of segmentation, p and q, dependent zonal harmonic coefficient errors, ϵ_0, ϵ_2, ϵ_4, ϵ_6, ϵ_8, and ϵ_{10}.

rents from spatially distributed currents by non-uniform current densities, the finite element analysis (FEA) adopting H formulation and domain homogenization technique is utilized. For simplicity, $I_c(B)$ of REBCO tapes of the magnet is assumed to be constant, 300 A. The critical electric field is set to be E_c = 1 μV/cm, while the index number. Both p and q in Figure 3.12 are 300.

Figure 3.14 shows the calculation results of axial magnetic fields along the magnet center. It provides: (a) one solid line with squares and the other solid line with circles represent, respectively, calculated magnetic fields from only the transport current and from both transport and screening currents (B_z^{scf}); and (b) total current densities (transport + screening), J_{total}, in the magnet. Table 3.4 presents spatial harmonic coefficients calculated by two different methods: the "Segmentation" method proposed in this thesis, and the "Inverse" method commonly used in previous reports where field gradients are calculated using field mapping results from FEA. Calculation results of low order harmonic coefficients ($Z0, Z2, Z4$) indicated in Table 3.4 show good agreement between "Segmentation" method and "Inverse" method, while high order harmonic coefficients ($Z6, Z8, Z10$) show significant errors. Calculation of harmonic coefficients via "Inverse" method could contain a severe error in high order terms by the limit of "Inverse" method, which found in the "uniform current density magnet" case. So, the results might demonstrate potential of the proposed "Segmentation" method to more accurately calculate the spatial harmonic coefficients of an HTS magnet with screening current considered.

So far, a nonlinear numerical analysis method of harmonic analysis, named "Segmentation" method, was studied to calculate spatial harmonic coefficients of magnetic fields generated from both transport and screening currents. The key idea is to divide the current flowing domain into multiple segments, obtain equivalent "loop" currents in each segment using the proposed equivalent current transformation technique, calculate harmonic coefficients of magnetic fields by the individual loop currents, and obtain the final harmonic coefficients using the superposition. To verify the

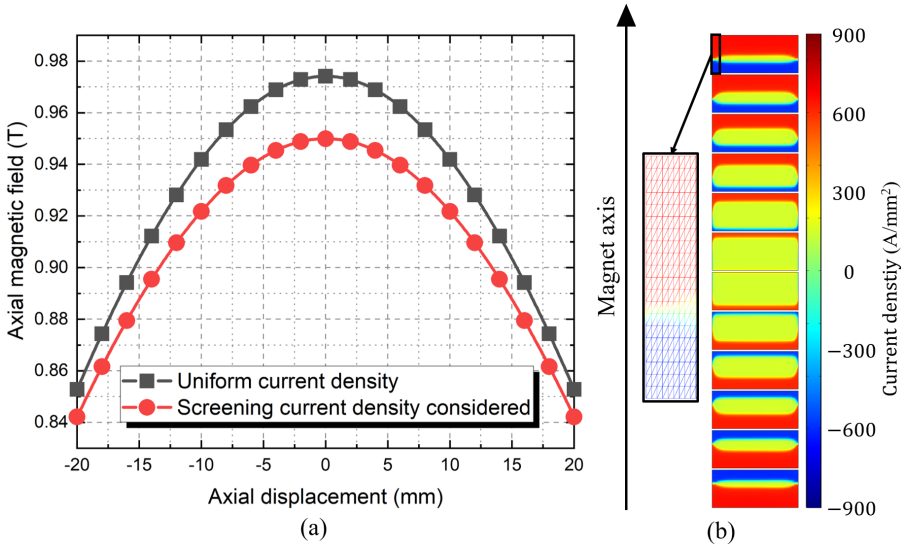

Figure 3.14: (a) Comparison between calculation results. (b) Calculation results of total current densities (transport + screening) in an HTS magnet.

Table 3.4: Spatial Harmonic Coefficients of Magnetic Fields Generated by the Chosen Solenoid Magnet with Screening Current Considered

Field	Coeff.	Unit	Segmentation	Inverse
B_z^{scf}	$Z0$	[T]	0.9500	0.9500
	$Z2$	[T/cm^2]	$-0.5720 \cdot 10^{-1}$	$-0.5720 \cdot 10^{-1}$
	$Z4$	[T/cm^4]	$0.9576 \cdot 10^{-2}$	$1.011 \cdot 10^{-2}$
	$Z6$	[T/cm^6]	$-0.2912 \cdot 10^{-2}$	$-1.053 \cdot 10^{-2}$
	$Z8$	[T/cm^8]	$-0.1488 \cdot 10^{-1}$	$2.094 \cdot 10^{-1}$
	$Z10$	[T/cm^{10}]	$0.3254 \cdot 10^{-1}$	2.000

proposed segmentation method, a solenoid high temperature superconductor (HTS) magnet comprising a stack of 12 single pancake coils was assumed and spatial field gradients of the magnet without screening current were calculated up to the 10^{th} order by the so-called Garrett's method (proven) and the proposed segmentation method. Good agreement between the two results validates feasibility of the proposed method to calculate harmonic field coefficients for a given current distribution. Then, harmonic coefficients of magnetic field generated by both transport and screening currents in the HTS magnet were calculated using the proposed segmentation method and "Inverse" method. In calculation of screening currents, the finite element method based on the edge-element of H formulation and the domain homogenization technique, both of which were reported previously, were used. Differences between "Inverse" and "Segmentation" methods in low order harmonic coefficients are less than 0.1% up to the 2^{nd} order, while 5% up to the 4^{th} order. However, significant differences are shown in high order terms due to a limit of a numerical analysis based "Inverse" method. The results demonstrate the potential of our segmentation method to accurately calculate spatial harmonic coefficient of magnetic fields of an HTS magnet with the non-uniform screening current distribution taken into account.

3.5 Mechanical Stress Distribution Simulation Method

As the magnetic field and current density of HTS magnet increase, a larger Lorentz force is generated within the magnet, and consequently, it can degrade the mechanical stability. As shown in Figure 3.15, most of the REBCO conductors experience 95% critical current degradation when the applied strain is larger than 0.4% [128]. Therefore, precise estimation of mechanical stress in superconducting magnets is essential for the mechanical integrity of such magnets. According to the record-high 45.5 T direct current magnet, it has been revealed that the screening current could exacerbate the mechanical stress problems in HTS magnets. Precise estimation of screening current

induced stress is an additional challenge for mechanical analysis of HTS magnets.

This chapter reviews how the conventional stress and strain analysis was performed in LTS magnets. The limitation of the conventional stress analysis methods to apply to HTS magnets is also presented. After that, a FEM based-stress analysis method for HTS magnets considering screening current and dry-winding technology is revisited.

3.5.1 Analytic formula-based method to analyze stress distribution

The stable operation of a superconductor magnet, both mechanically and electrically, is essentially required for various applications. Meanwhile, one of the determinants to regulate the stable operation is the displacement of superconductor wires. The dis-

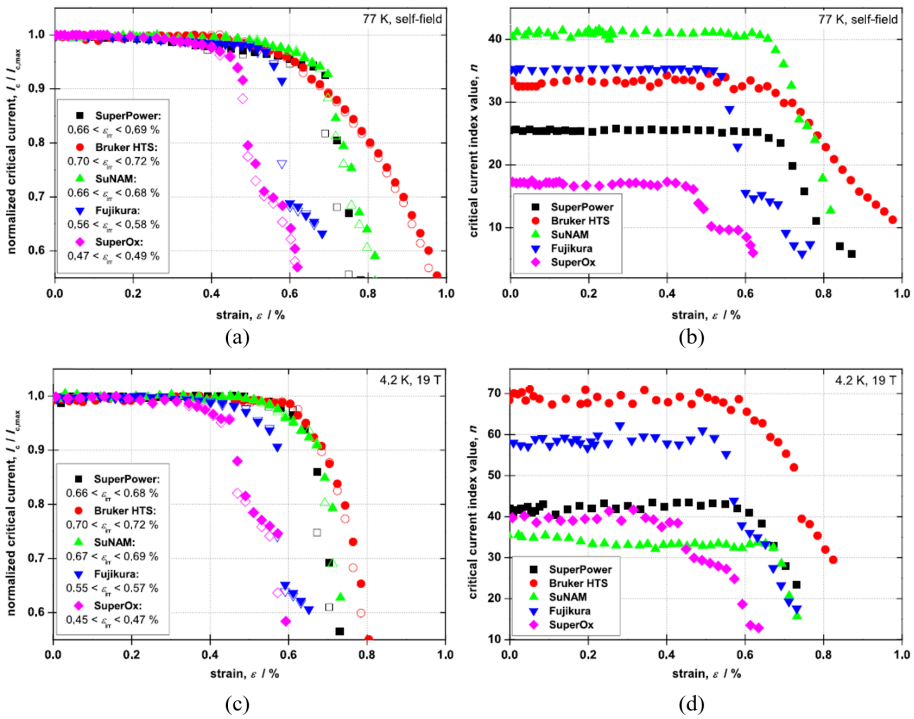

Figure 3.15: Experimental results of critical current characteristics depend on the applied mechanical stress at (a)–(b) 77 K of liquid nitrogen and (c)–(d) 4.2 K of liquid helium.

placement induces mechanical stress in a superconductor magnet. The mechanical stress can degrade the current-carrying capacity of superconducting wires. As a result, excessive mechanical stress and strain issues caused by intense Lorentz force, the product of high current density and high field in a superconductor magnet itself, have been discussed for a long time. Researchers have made numerous endeavors to address mechanical issues. They thus have studied numerical simulation approaches to calculate mechanical stress and strain distribution in superconductor magnets.

In continuum mechanics, the Cauchy stress tensor, also called stress tensor, is widely utilized to assess mechanical stress distribution caused by a volume force in a continuum body, and the tensor is also available to calculate stress distribution in superconductor magnets. The stress tensor is a second order tensor and it consists of nine components that completely define the state of stress at a point inside a material:

$$\sigma_{ij} = \begin{bmatrix} \sigma_{11} & \sigma_{12} & \sigma_{13} \\ \sigma_{21} & \sigma_{22} & \sigma_{23} \\ \sigma_{31} & \sigma_{32} & \sigma_{33} \end{bmatrix}, \tag{3.89}$$

where components along the diagonal of the matrix present normal stress, while off-diagonal components are shear stress. According to the principle of conservation of linear momentum, if a given continuum body is in static equilibrium, then it can be demonstrated that the components of stress tensor should satisfy the equilibrium equations:

$$\sigma_{ji,j} (\equiv \sigma_{ij} \mathbf{n}_j) + \mathbf{F}_i = 0, \tag{3.90}$$

where $\mathbf{n}_j$ is a normal vector and $\mathbf{F}_i$ is a body force per unit volume. In addition, according to the principle of conservation of angular momentum, equilibrium requires that the summation of moments with respect to an arbitrary point is zero, which leads to the conclusion that the stress tensor is symmetric, thus having only six independent stress components, instead of the original nine:

$$\sigma_{ij} = \sigma_{ji}. \tag{3.91}$$

Note that the only source to induce stress in a continuum body is deformation. Here one can conclude that a theory is needed to define deformation for the stress calculation; the infinitesimal strain theory can gratify the needs.

The infinitesimal strain theory is a mathematical approach to describing the deformation of a continuum body. The displacements of the material particles are assumed to be much smaller (indeed, infinitesimally smaller) than any relevant dimension of the body. Let's assume that constitutive properties of a material, e.g., density and stiffness, are unchanged by the deformation. Then, the infinitesimal strain tensor, also known as Cauchy's strain tensor, is considerably simplified, and they are presented with:

$$u_i = [u_1, u_2, u_3], \tag{3.92}$$

$$\begin{aligned}
\epsilon_{ij} &= \frac{1}{2}[(\nabla u_i)^{tr} + \nabla u_i] \\
&= \frac{1}{2}(u_{i,j} + u_{j,i}) \\
&= \begin{bmatrix} \epsilon_{11} & \epsilon_{12} & \epsilon_{13} \\ \epsilon_{21} & \epsilon_{22} & \epsilon_{23} \\ \epsilon_{31} & \epsilon_{32} & \epsilon_{33} \end{bmatrix} \\
&= \begin{bmatrix} \frac{\partial u_1}{\partial x_1} & \frac{1}{2}\left(\frac{\partial u_1}{\partial x_1} + \frac{\partial u_1}{\partial x_1}\right) & \frac{1}{2}\left(\frac{\partial u_1}{\partial x_1} + \frac{\partial u_1}{\partial x_1}\right) \\ \frac{1}{2}\left(\frac{\partial u_1}{\partial x_1} + \frac{\partial u_1}{\partial x_1}\right) & \frac{\partial u_1}{\partial x_1} & \frac{1}{2}\left(\frac{\partial u_1}{\partial x_1} + \frac{\partial u_1}{\partial x_1}\right) \\ \frac{1}{2}\left(\frac{\partial u_1}{\partial x_1} + \frac{\partial u_1}{\partial x_1}\right) & \frac{1}{2}\left(\frac{\partial u_1}{\partial x_1} + \frac{\partial u_1}{\partial x_1}\right) & \frac{\partial u_1}{\partial x_1} \end{bmatrix}
\end{aligned} \tag{3.93}$$

where u_i is a displacement vector, $x_{i\in\{1,2,3\}}$ dimension variables, and ϵ_{ij} Cauchy's strain tensor. Especially for a superconductor magnet, which is axisymmetric, the stress and strain tensors can be defined within a cylindrical coordinate (r, ϕ, z). The orientations for components in the tensors are named, respectively, radial (r), hoop (ϕ), and axial (z) assuming that the basis dimension variables are set to be (r, ϕ, z).

Superconductor wire consists of superconductor, buffer layer, reinforcement structure and others. Instead of considering each components, equivalent mechanical porperties are conventionally used to simplify the stress formulation. Note that the me-

chanical properties of the composite wire are homogeneous, linear, and orthotropic. Then, generalized Hooke's law for stress and strain relation is given by the following equations:

$$\epsilon_r = \frac{1}{E_r}\sigma_r - \frac{\nu_{\theta r}}{E_\theta}\sigma_\theta - \frac{\nu_{zr}}{E_z}\sigma_z, \tag{3.94}$$

$$\epsilon_\theta = \frac{\nu_{r\theta}}{E_r}\sigma_r + \frac{1}{E_\theta}\sigma_\theta - \frac{\nu_{z\theta}}{E_z}\sigma_z, \tag{3.95}$$

$$\epsilon_r = -\frac{\nu_{rz}}{E_r}\sigma_r - \frac{\nu_{\theta z}}{E_\theta}\sigma_\theta + \frac{1}{E_z}\sigma_z, \tag{3.96}$$

$$\gamma_{rz} = \frac{1}{G_{rz}}\tau_{rz}, \tag{3.97}$$

where E_r, E_θ, and E_z are Young's moduli. ν_{rz}, $\nu_{\theta z}$, and $\nu_{r\theta}$ are Poisson's ratios. G_{rz} is the shear modulus. ϵ_r, ϵ_ϕ, and ϵ_z are the strains in the orthgonal directions, and γ_{rz} is the shear strain in the r-z plane. Figure 3.16 presents an example of cross section of a uniform current density solenoid. In the magnet, the mechanical stresses consisting of $\sigma_r(r,z)$ (radial component), $\sigma_\phi(r,z)$ (hoop component), $\sigma_z(r,z)$ (axial component), and $\tau_{rz}(r,z)$ (shear component) are distributed in the windings that are subjected to a magnetic force density generated by uniform current density (λJ) in the magnet. If shear stress is neglected, force balance equation of a continuum solenoid magnet is given by the following equations:

$$r\frac{\partial \sigma_\rho}{\partial r} + \sigma_\rho - \sigma_\theta = -B(r)Jr. \tag{3.98}$$

In the case of an axisymmetric body, the relation between radial displacement, u_r, and strain are given by equations:

$$\epsilon_r = \frac{\partial u_r}{\partial r}, \tag{3.99}$$

$$\epsilon_\theta = \frac{u_r}{r}. \tag{3.100}$$

Considering (3.96)–(3.98), (3.101) is obtained:

$$\frac{d^2u_r}{dr^2} + \frac{1}{r}\frac{du_r}{dr} - \zeta^2\frac{u_r}{r^2} = -\frac{1-\nu_{r\theta}\nu_{\theta r}}{E_r}\lambda J B_z(r), \tag{3.101}$$

$$\zeta = \sqrt{\frac{E_\theta}{E_r}}. \tag{3.102}$$

By solving this equation, together with the boundary conditions that radial stress at the innermost and outermost radial end is zero, stress distributions within the magnet can be calculated.

3.5.2 Finite element method to simulate stress distribution

However, the method mentioned above is not applicable in the stress analysis of HTS magnets. The reasons are summarized as follows: first, the current density is non-uniform due to the screening current, and second, the windings in an HTS magnet do not behave like a continuum but behave as individual bodies due to the dry winding technique. For two reasons, the stress analysis of an HTS magnet has to incorporate the mechanical contact between adjacent turns and the non-uniform stress distribution due to SCS. In detail about the former one, the mechanical stress distribution in the section acting as a continuum should be derived considering the force equilibrium, while the area acting as an individual body through the presence or absence of mechanical con-

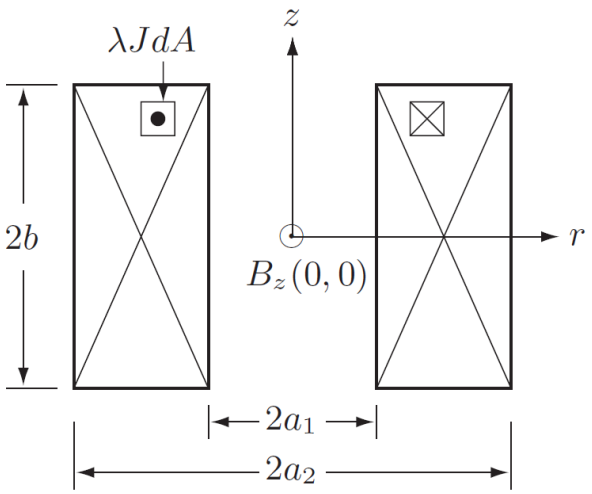

Figure 3.16: Schematic drawing of a solenoid magnet with uniform current density. a_1, a_2, b, and λJ indicate the inner radius, outer radius, the half of total height, and uniform current density in the magnet.

tact between adjacent windings should be derived considering the force equilibrium or the Lorentz force. To solve this problem, first, a numerical analysis model based on FEA was adopted. The governing equations of the stress and strain analysis are give with (3.103)–(3.105)

$$\rho \frac{\partial^2 \mathbf{u}}{\partial t^2} = \nabla \cdot (\mathrm{FS})^{\mathrm{tr}} + \mathrm{Fv}, \tag{3.103}$$

$$\mathrm{F} = \mathrm{I} + \nabla \mathbf{u}, \tag{3.104}$$

$$\mathbf{u} = [u, 0, w]^{\mathrm{tr}}, \tag{3.105}$$

where ρ, **u**, S, F, I, and v indicate, respectively, the density, displacement vector, stress tensor, deformation gradient, identity tensor, and volume. Figure 3.17 presents to-scale drawings of a few turns wound HTS coil and boundary conditions for the stress and strain analysis: (a) a to-scale drawing including coil bobbin and HTS windings; (b) the contact boundary conditions colored by violet lines between adjacent turns; (c) the roller condition colored by blue lines at the top and bottom surfaces of the given coil; and (d) the fixed condition colored by a blue box. For the roller condition, $\mathbf{u} \cdot \mathbf{n}$ is imposed, where **n** is the normal vector of the selected surface. For the fixed boundary condition, $\mathbf{u} = 0$ is imposed.

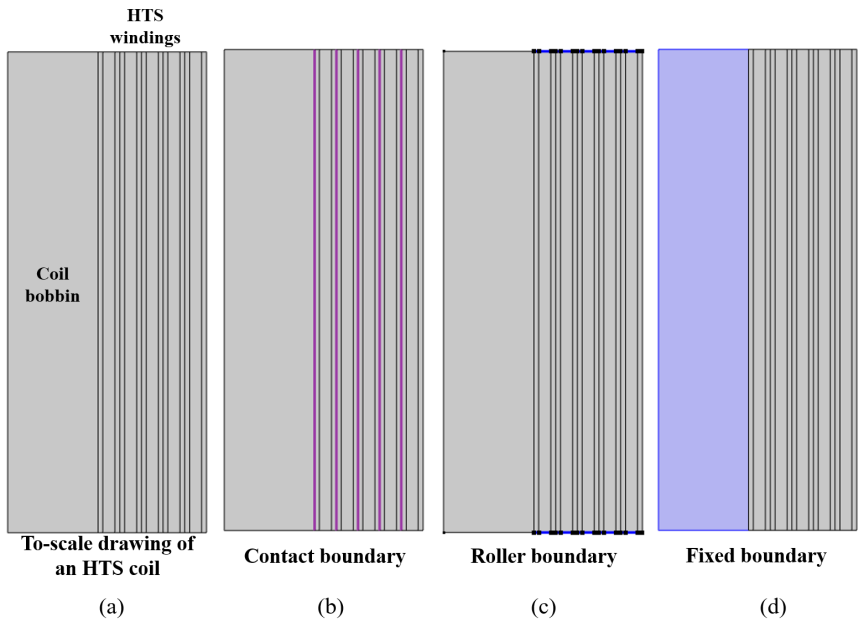

Figure 3.17: (a) To-scale drawing coil bobbin and HTS windings. (b)–(d) Various contact boundary conditions used for the mechanical stress simulation.

Chapter 4

Analysis Results of HTS NMR Magnets to Demonstrate Numerical Simulation Methods of Screening Current

4.1 Introduction to the Project of a 400 MHz ^{1}H NMR Application Development using a 9.4 T All-HTS Magnet

Korea Basic Science Institute (KBSI) launched a project to develop an NMR application using an HTS magnet only. The main target of this project was to validate the feasibility of using HTS magnets for an NMR application. Researchers proposed to compose two sequential studies for the project. During the first step, the magnet named "Demo (Demonstration)" was designed, constructed, and tested by a collaborative team led by KBSI. They intended to demonstrate the feasibility of the key approaches in building a 9.4 T 66 mm all-HTS magnet for a 400 MHz NMR application [126] with this preliminary study. The Demo consists of a stack of 32 double-pancake (DP) coils with the so-called multi-width [129] technique incorporated. As a result, the Demo magnet successfully reached its full field of 3 T under a conduction-cooling environment at 17 K in 2016 and an NMR signal was captured after a series of ferro-shimming in 2017 [130, 131]. As expected, its "pre-shim" spatial field gradients of the Demo magnet were substantially larger than those originally designed [132]

mainly due to SCF as well as construction errors. From the Demo magnet test results, nevertheless, it was concluded that the feasibility of using an HTS magnet for an NMR application was validated partially. During the second step, the collaborative team performed the main study of a 9.4 T HTS NMR magnet. They designed, constructed, and tested a 9.4 T HTS magnet for a 400 MHz ^{1}H NMR application based on the experience of successful development of the 3 T HTS Demo magnet. As expected, the development has been successfully completed. The 9.4 T magnet fully charged up to its full field under a conduction-cooling environment at 10 K in 2018 and a sub-ppm level NMR signal was finally captured. The achievement of all-HTS NMR magnet development was a genuine milestone in the HTS magnet discipline in that the collaborative team firstly developed an HTS NMR system comparable to its LTS NMR counterpart and addressed SCF issue on field uniformity. In addition, the achievement deserved to be selected as a state-of-the-art HTS technology [133] since the persistent SCF issue of HTS magnet technology was addressed by using numerical simulation methods, a passive magnetic field uniformity improvement technique, and other techniques. Here I have made a lot of endeavors in analyzing screening current and its effects on HTS coils and demonstrated the validity of using the methods by comparing simulated results and measured ones.

4.2 Analysis Results of a 3 T All-HTS NMR Demo Magnet

A preliminary study was performed using the H formulation method and domain homogenization technique. This study aims to validate the use of a “integrated” (H formulation + domain homogenization) FEA method to analyze screening current and the consequent effect, i.e., SCF, at the NMR magnet level. For the numerical simulation, first, the highly nonlinear conductivity in terms of field-dependent $I_c(\mathbf{B})$ was reviewed since it directly affects the non-uniform current density analysis. Reconstruction of $I_c(\mathbf{B})$ was performed based on measured $I_c(\mathbf{B})$ with a variation of curve fitting tech-

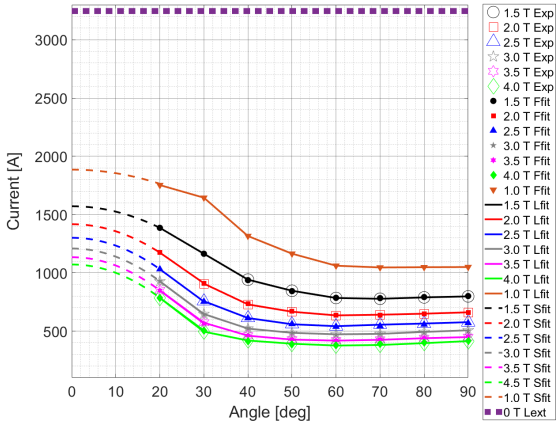

Figure 4.1: $I_c(B, \theta)$ of a 12 mm SuNAM HTS tape at 20 K. Exp, Ffit, Lint, Sfit, and Lext in the legend stand for data obtained from experiment, curve fit using (4.1), linear interpolation, spline curve fit, and linear extrapolation, respectively.

niques [79, 134, 135]. Figure 4.1 shows measured and reconstructed $I_c(\mathbf{B})$ of a 12 mm wide sample tape. In Figure 4.1, open symbols stand for measured data at the magnitude of $|\mathbf{B}|$ (B) of 1.5–4 T and the field angle of $\mathbf{B}$ (θ) of 20–90°. Note that θ = 90° represents the direction parallel to the c-axis of the HTS layer. The curve fitting function is provided with (4.1):

$$I_c(\mathbf{B}) = I_c(B, \theta) = a(\theta) B^{-b(\theta)}, \tag{4.1}$$

where $a(\theta)$ and $(\theta)b$ are constants for a given field angle of θ ranged 20–90° (Table 4.1). The results of $I_c(B, \theta)$ were adopted in the calculation of HTS conductivity described with the power-law E–J model [136].

Table 4.2 presents key parameters the 3 T HTS magnet. It consists of a stack of multiple coils, while Table 4.3 presents the measured dimensions of the magnet. In case of an HTS magnet, an HTS tape has the key feature of thin tape and thus high current density in an HTS winding. Since the high current density can affect electromagnetic simulation results, especially for spatial magnetic fields, the use of measured dimensions of an HTS magnet is desirable in an electromagnetic simulation.

Table 4.1: Constants for $I_c(B, \theta)$ Reconstruction using (4.1) for 1 T $\leq B \leq$ 4 T and $\theta \geq 20^\circ$

	Field Angle θ°							
	20	30	40	50	60	70	80	90
a	1753	1644	1316	1136	1062	1048	1045	1051
b	0.579	0.853	0.837	0.797	0.741	0.715	0.691	0.668

Table 4.2: Key Parameters of the 3 T HTS magnet for a case study

Magnet parameters	Unit	
Inner diameter (ID)	[mm]	100–101.9
Outer diameter (OD)	[mm]	115.4
Tape width	[mm]	4.1–8.1
Total height	[mm]	328.0
Operating current, I_{op}	[A]	201.16
Operating temperature, T_{op}	[K]	17
Inductance, L	[H]	0.581
Stored magnetic energy	[kJ]	11.7
Peak magnetic stress	[MPa]	70.8

Table 4.3: Measured geometric dimensions of the 3 T HTS NMR Demon Magnet. [unit: mm]

	SP1	SP2	SP3	SP4	SP5	SP6	SP7	SP8	SP9	SP10	SP11	SP12	SP13	SP14	SP15	SP16	SP17
ID	112.7	106.9	107.0	107.0	107.3	107.4	107.2	107.2	107.4	107.3	107.1	107.2	107.1	107.2	107.2	107.4	107.3
OD	114.5	114.5	114.6	114.7	114.9	115	114.8	114.7	114.8	114.9	114.9	114.5	114.7	114.5	114.4	114.4	114.4
Center	168.4	159.7	151.4	143.2	135.9	128.7	122.4	116.2	110.9	105.7	101.4	96.7	92.4	87.7	83.4	78.7	74.4
Turn	13	69	69	65	66	66	64	65	67	64	64	64	64	64	64	65	65
	SP18	SP19	SP20	SP21	SP22	SP23	SP24	SP25	SP26	SP27	SP28	SP29	SP30	SP31	SP32	SP33	SP34
ID	107.1	107.1	108.1	108.1	108.1	108.1	108.4	108.4	108.4	108.5	108.4	108.4	108.2	108.1	108.2	108.2	108.2
OD	114.4	114.4	114.4	114.2	114.7	114.8	115.0	114.6	114.8	114.9	114.8	114.8	114.6	114.5	114.8	114.6	114.4
Center	69.7	65.4	60.7	56.4	51.7	47.4	42.7	38.4	33.7	29.4	24.7	20.4	15.7	117.4	6.70	2.40	-2.30
Turn	64	64	56	56	56	56	56	56	56	56	56	56	56	56	56	56	56
	SP35	SP36	SP37	SP38	SP39	SP40	SP41	SP42	SP43	SP44	SP45	SP46	SP47	SP48	SP49	SP50	SP51
ID	108.4	108.2	108.3	108.4	108.4	108.4	108.4	108.4	108.3	108.1	108.1	107.2	107.2	107.2	107.2	107.2	107.2
OD	114.6	114.4	114.5	114.9	115.0	115.0	114.9	114.8	114.9	114.3	114.3	114.3	114.1	114.2	114.2	114.5	114.7
Center	-6.60	-11.3	-15.6	-20.3	-24.6	-29.3	-33.6	-38.3	-42.6	-47.3	-51.6	-56.3	-60.6	-65.3	-69.6	-74.3	-78.6
Turn	56	56	56	56	56	56	56	56	56	56	56	56	55	64	64	64	64
	SP52	SP53	SP54	SP55	SP56	SP57	SP58	SP59	SP60	SP61	SP62	SP63	SP64	SP65	SP66		
ID	107.2	107.1	107.2	107.3	107.5	107.4	107.4	107.3	107.3	107.5	107.4	107.3	106.8	106.8	113.0		
OD	114.4	114.5	114.6	114.3	114.7	115.2	114.8	114.4	114.9	114.6	114.7	114.4	114.5	114.5	114.5		
Center	-83.3	-87.6	-92.3	-96.6	-101.3	-105.6	-110.8	-116.1	-122.3	-128.6	-135.8	-143.1	-151.3	-159.6	-168.3		
Turn	64	64	64	63	64	65	66	65	66	65	64	64	68	68	13		

1: SP is the abbreviation of single pancake which is the typical geometry shape of HTS solenoid magnet.

Figure 4.2–4.4 illustrates nonlinear numerical analysis results. Figure 4.2 illustrates: (a) a to-scale drawing of the 3 T HTS NMR Demo magnet; (b) total current density in the upper (left) and lower (right) halves of the all the 66 single pancake coils; (c) radial magnetic flux density (B_r); and (d) the corresponding axial magnetic flux density (B_z). Figure 4.3 compares axial field scans along the magnet axis: squares for calculated fields using the actual coil dimensions in Table 4.3 and considering only the transport currents without screening currents (B_{unf}). In Figure 4.3, circles, triangles, and stars stand for, respectively, calculated fields from screening and transport currents with actual coil dimensions (B_{scf}), measured fields (B_m), calculated fields using the original design parameters (B_d). B_{unf} shows a strong asymmetry on the magnet midplane $z = 0$ when compared with B_d, which confirms the field errors due to the manufacturing uncertainties. Significant discrepancy was observed between B_{scf} and B_{unf}, which explains the strong impact of screening currents on the spatial field distribution of the Demo magnet. A difference in magnitude between B_{scf} and B_m was also observed in Figure 4.3. The ratio of peak value between B_m and B_{scf} is about 1.02. It is suspicious that the mechanical contraction due to thermal contraction or due to the axial force for module coil integration causes the difference between calculation and measurement. Yet, with the given uncertainties of electromagnetic properties of the HTS tapes, the normalized B_{scf} agrees reasonably well with the normalized B_m as shown in Figure 4.4.

So far, the comparison results are provided. The good agreement between the normalized B_{scf} and B_m was confirmed, but the discrepancy in the magnitude. It was concluded that the difference in the peak value may be caused by the mechanical contraction of HTS winding. However, the thermal contraction coefficients of all the HTS windings and other structures for an HTS magnet and all the tape widths are not measurable, which implies that they are "unknown" parameters. Thus, the ratio between the peak value of B_{scf} and that of B_m is set to be a correction factor, and it is used in the nonlinear numerical analysis study of a 9.4 T HTS NMR magnet.

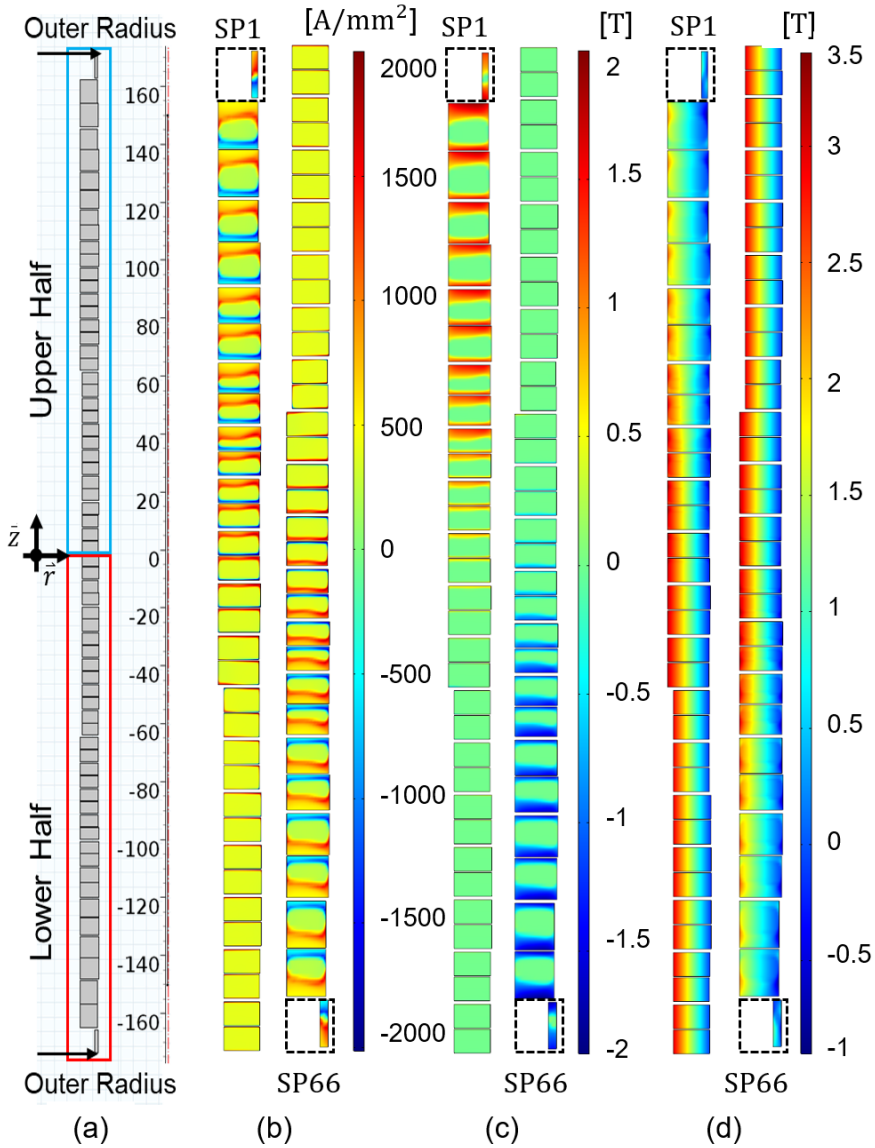

Figure 4.2: Simulation results of: (a) a to-scale drawing of the 3 T HTS magnet; (b) total current density including transport current and screening current; (c) radial magnetic field B_r; and (d) axial magnetic field B_z.

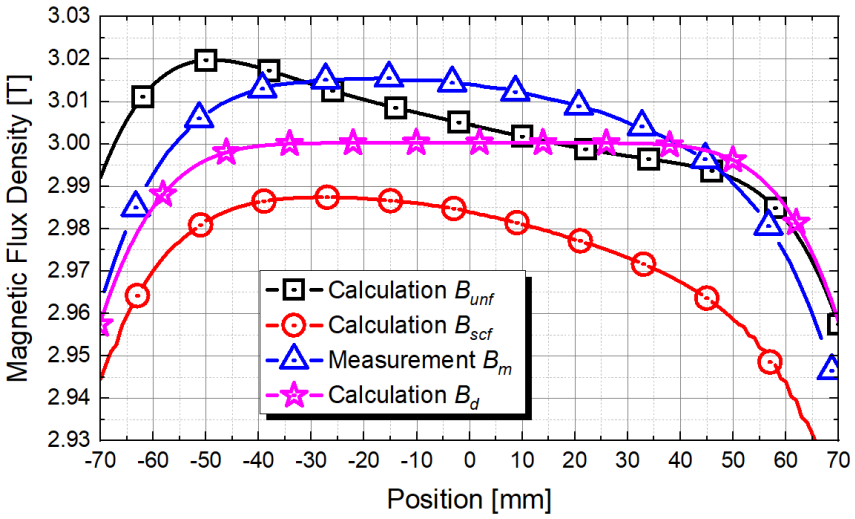

Figure 4.3: Calculated and measured axial magnetic fields along the magnet axis

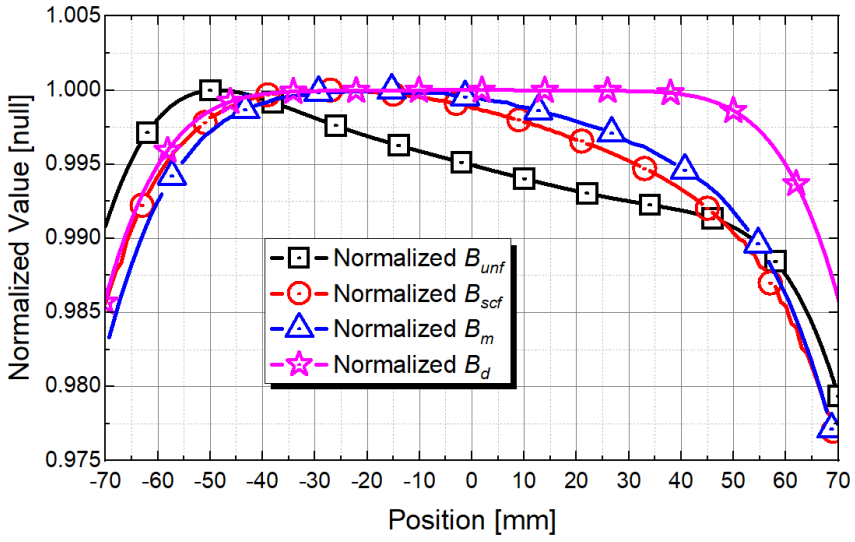

Figure 4.4: Peak normalized magnetic fields.

4.3 Analysis Results of a 9.4 T All-HTS NMR Magnet

4.3.1 Key parameters of the 9.4 T HTS NMR magnet

Key parameters were summarized in Table 4.4; the 9.4 T 100 mm HTS NMR magnet analysis results with the simple assumption of uniform current distribution are provided in Figure 4.5. The HTS magnet has the advantage that it is highly compact compared with its LTS counterparts due to the NI winding technique. In addition, the high-performance I_c of HTS tape in high fields may also affect the compactness. The self-field I_c at 77 K of liquid nitrogen is about 200 A for a 4.1 mm wide HTS tape. The field and temperature-dependent critical current $I_c(B,T)$ data were considered in the design, as provided in Figure 4.6. Meanwhile, the reconstruction approach provided in the preliminary study of the 3 T HTS NMR Demo magnet is also used in this study. For this project, $I_c(B,T)$ of a 4.1 mm wide short-sample tape was measured at 4.2 K, 20 K, 40 K, and 77 K because of the temperature dendency of I_c; here the field angle of 90° corresponds to the direction parallel to the HTS c-axis. Based on the $I_c(B,T)$ data, I_c analysis was performed to investigate minimum I_c of the HTS NMR magnet and determine operating current (I_{op}). The so-called "equivalent" I_c mapping technique was incorporated to obtain I_c distribution in the magnet. As a result, the simulated minimum I_c of the 9.4 T HTS NMR magnet is far larger than its opering current of $\sim$190 A at 10 K.

In the construction phase, HTS tapes of 144–152 m in length were used for fabricating double-pancake (DP) coils. A constant winding tension was applied during the winding process. After the winding was completed, all the DPs were stacked in accordance with the design table. After the stacking step, the number of turns of each DP was adjusted to make the outer diameters identical to some extent to ease the DP-to-DP joint procedure. Since, it was identified that manufacturing uncertainties affect numerical simulation of screening current in an HTS magnet, the "average" thickness of HTS windings in each HTS coil was thus measured, Figure 4.7.

Table 4.4: Key parameters of a 400-MHz/100-mm NI HTS NMR Magnet

Parameter		M1N	M2	M3N	M4	M5N	M6	M7N	M8	M9N	M10	M11	M12	M13	M14
Conductor configuration															
Average width and thickness	[mm]	4.1 – 8.1; 0.12													
Effective $\boldsymbol{E}$	[GPa]	$(E_r, E_\theta, E_z) = (156, 168, 168)$													
Magnet configuration															
Inner and outer radii	[mm]	50 – 51.34; 73.4													
Overal height ($2b$)	[mm]	512													
Total tape length	[km]	8.66 (4.1-mm equivalent)													
Operation															
B_{cen}	[T]	9.4 (400 MHz ^{1}H frequency)													
I_{op}	[A]	187.36													
T_{op}	[K]	20													
J_{cond}	[A/mm^2]	380	380	380	380	380	380	380	380	380	380	306	256	220	193
Inductance, L	[H]	8.50													
Peak $B \perp$	[T]	0.25	0.36	0.33	0.39	0.13	0.26	0.29	0.73	0.66	1.20	1.24	1.24	1.28	2.58
Peak stress, σ_{mag}	[MPa]	$\sim$120 (ν:0.3; no overbanding; all compressive radial stress with a peak of -5.9 MPa)													
Field homogeneity															
$\lvert z \rvert < 1.5$cm	[ppm]	< 1 (ideal before shimming)													
$Z2$	[Hz/cm^2]	-0.3429$\times 10^2$													
$Z4$	[Hz/cm^4]	-0.5282$\times 10^3$													
$Z6$	[Hz/cm^6]	-0.2618$\times 10^3$													
$Z2$	[T/cm^2]	-0.8053$\times 10^{-6}$													
$Z4$	[T/cm^4]	-0.1243$\times 10^{-4}$													
$Z6$	[T/cm^6]	-0.6149$\times 10^{-5}$													

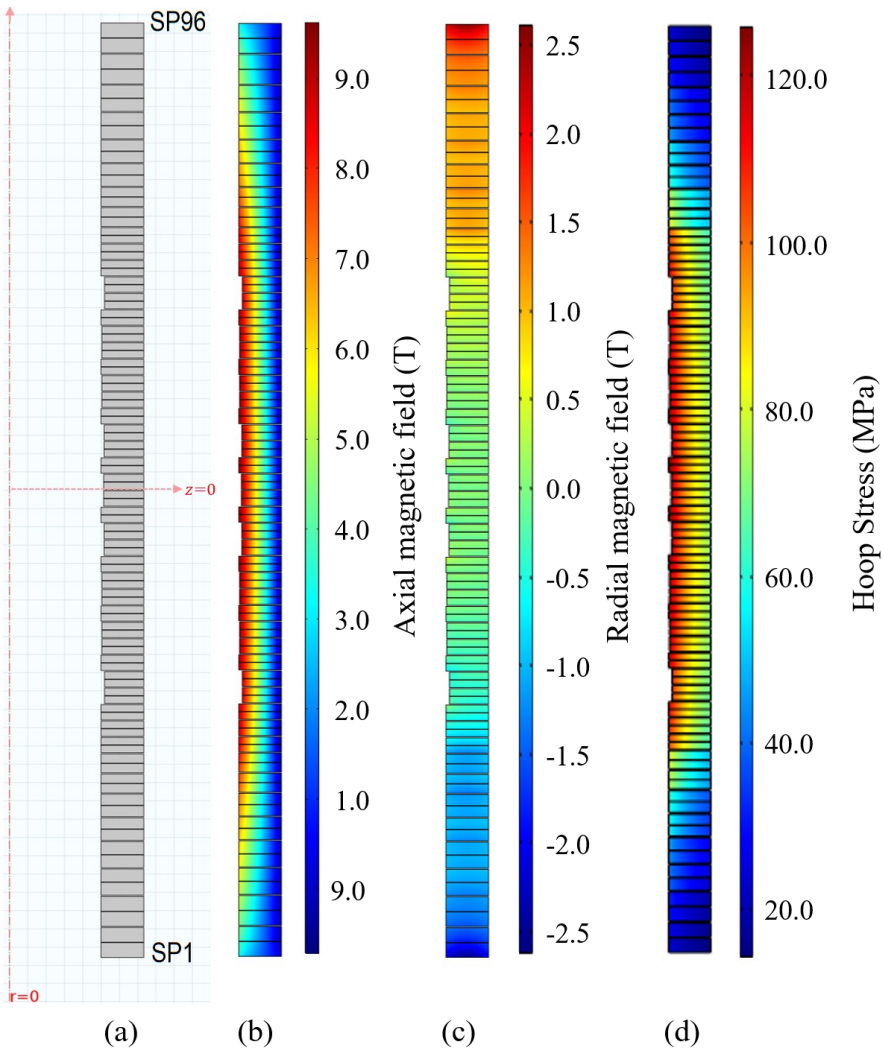

Figure 4.5: To-scale drawings of a 9.4 T all-HTS magnet: (a) the design result; (b)–(c) electromagnetic analysis results of axial and radial magnetic fields in an HTS magnet assuming the uniform current density in each coil; and (d) hoop stress analysis results.

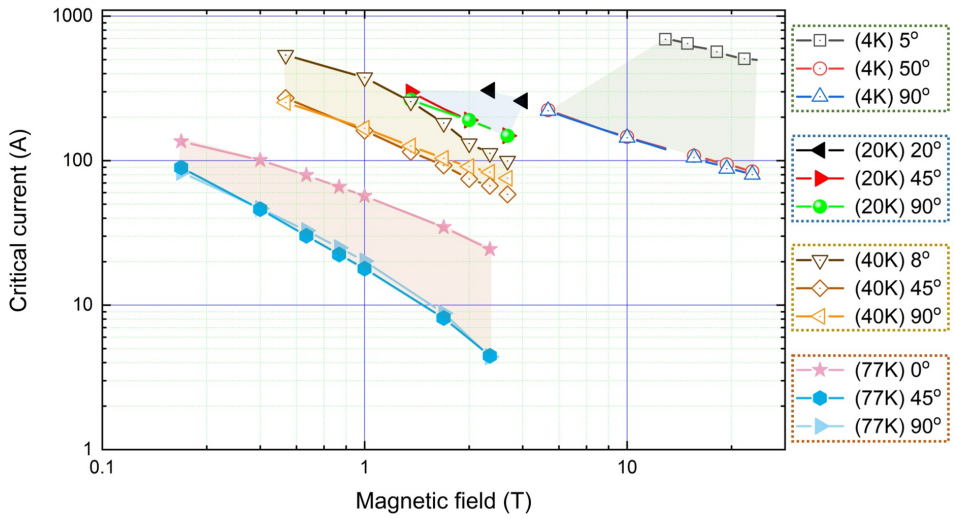

Figure 4.6: Measured $I_c(B,T)$ of an HTS tape used for the 9.4 T HTs magnet construction. This data was measured by SuNAM Co., Ltd.

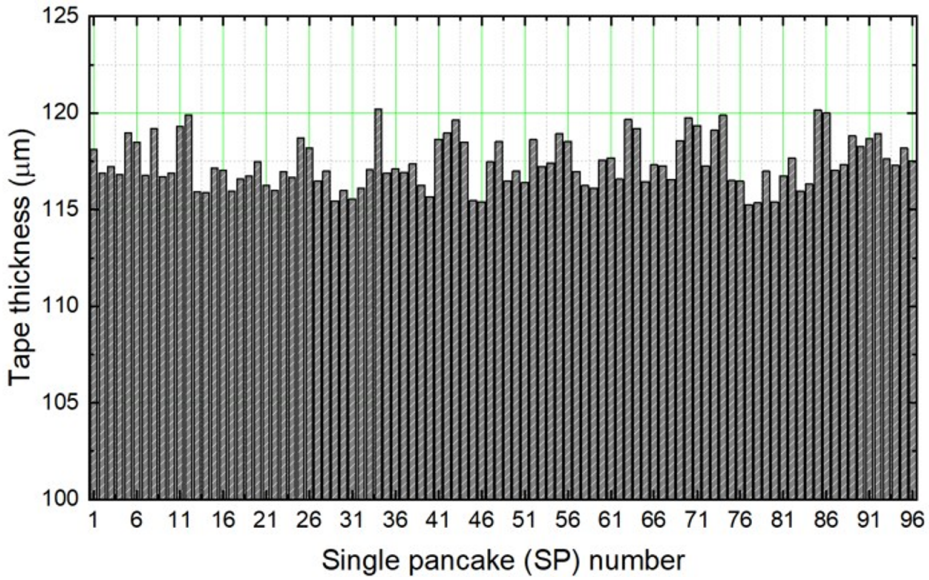

Figure 4.7: Measured thickness of individual HTS single pancake (SP) coils.

In the installation phase, reinforcement parts for mechanical supports and cooling components for the conduction cooling channel connected to the main cold head of a cryocooler were assembled. After the magnet construction and instrumentation were completed, the magnet was initially energized in liquid nitrogen (LN2) bath at 77 K to check instrumentation signals and operational parameters of the magnet. These parameters include the inductive and resistive voltage induced by characteristic resistance, lap-joint resistance, and DP-DP splice resistance. The average resistance of all the DPs was 154 nΩ, as shown in Figure 4.8. In addition, from an experiment at 77 K, coil-I_c, characteristic resistances, the effective inductance of each DP coil, and other equivalent electric parameters of each DP coil were evaluated from the measured DP terminal voltages, center fields, and power supply data.

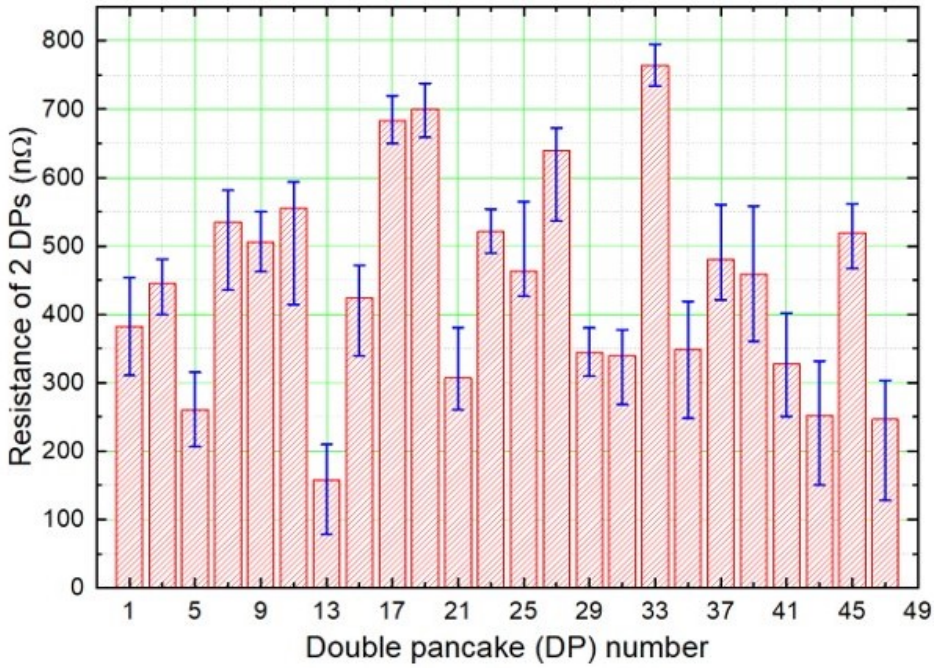

Figure 4.8: Measured results of joint resistance between adjacent HTS module coils in the 9.4 T HTS magnet.

Figure 4.9 provides the construction and instrumentation result of the 9.4 T HTS NMR magnet. There are 48 DP coils, and two single pancake type superconducting current leads at the top and bottom. The superconducting current lead was used to carry a high current with negligible Joule heating loss. Each copper block for the conduction-cooling attached to each DP coil is connected to the main stage of a cryocooler by using audio cables containing a substantial amount of silver for superb thermal conductivity.

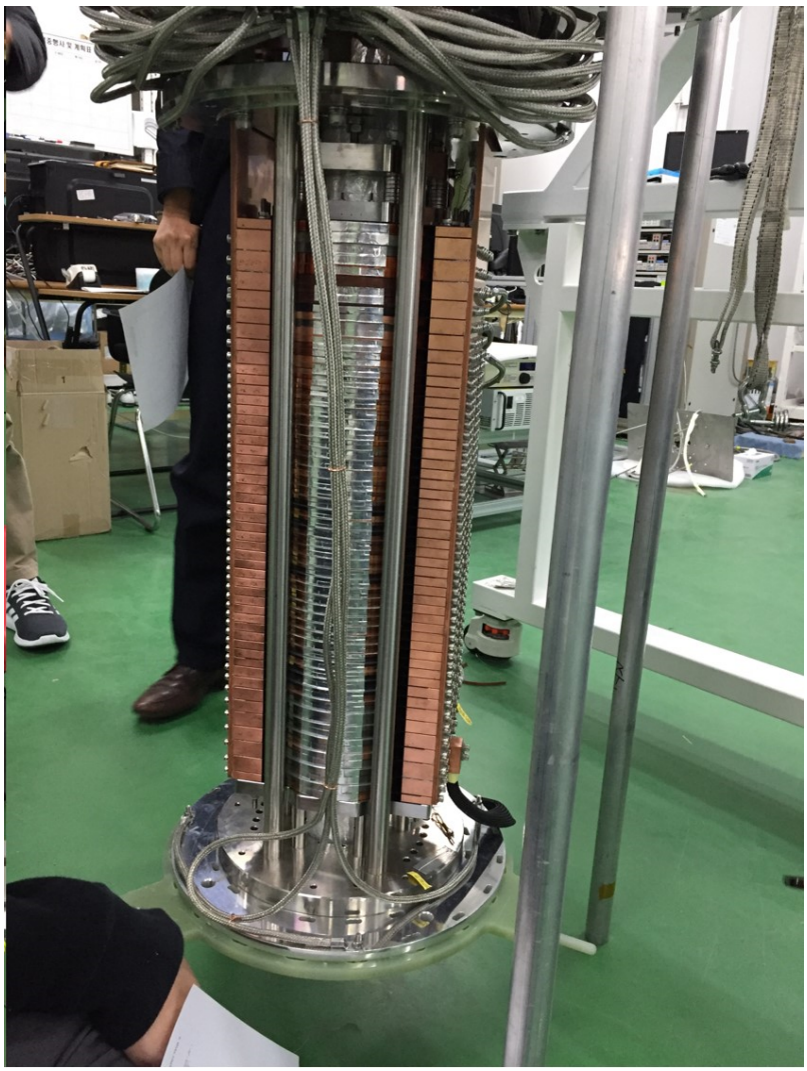

Figure 4.9: KBSI 9.4 T all-HTS 400 MHz NMR magnet.

After the construction, the 9.4 T HTS NMR magnet was cooled down, and sequentially, a charge and discharge test was performed. The operating temperature of the magnet was about 10 K. It was charged up to its operating current of 187 A. To substantially suppress pernicious impacts of turn-to-turn leak current due to NI configuration on the 9.4 T HTS NMR magnet, the charging rate of the magnet was set to be extremely slow. Hence, it was found that temperature increment occurred during the magnet operation, but the magnitude was marginal; it means that the leak current is also marginal, and consequently, the magnet is thermally stable. The target magnetic field of 9.4 T was finally reached at the magnet center. The results are presented in Figure 4.10. It provides the operating current from the power supply for the magnet, total voltage of the magnet, magnetic field at the magnet center, and temperatures of selected DP coils.

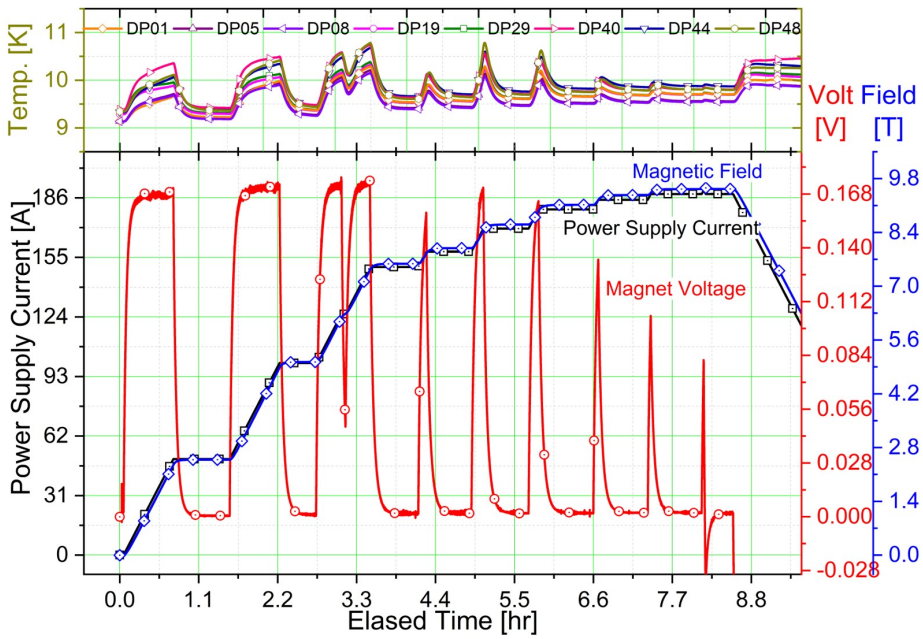

Figure 4.10: Operation results of the 9.4 T HTS NMR magnet.

4.3.2 Numerical simulation results

Non-uniform current and field distribution with screening current

Figure 4.11 presents the calculation results of non-uniform current density in the 9.4 T HTS NMR magnet when the HTS magnet is fully charged. Figure 4.12 provides the consequent magnetic fields. The current distribution includes transport current and screening current. FEA adopting the H formulation and domain homogenization technique was utilized. Measured $I_c(B,T)$ and geometric dimensions were considered. The power-law model for the electromagnetic $E-J$ constitutive law is adopted; the index value is set to be n=30 in average based on a reference [137]. For the magnet operation, it was assumed that the operating current (I_{op}) was charged up to its target current with the constant charge rate. Meanwhile, additional results that depend on the operating current were provided in Figure 4.13–4.16: Figure 4.13, 4.14, 4.15, and 4.16 stand for, respectively, non-uniform current distribution, radial magnetic field distribution, axial magnetic field distribution, J_c distribution according to I_{op}=50, 100, 150, 160, 170, and 180 A. There are marginal differences when I_{op} becomes larger than 150 A. Near the top and bottom coils, where the penetrating field is intense compared to the central coils, the non-uniform current density is prominent. However, when $I_{op} > 150$ A, the little variation is confirmed. It may be due to the so-called "full" penetration phenomenon. When HTS windings are in the "full" penetration state, radial magnetic fields penetrating individual windings can not be expelled. Consequently, the non-uniformity of current distribution in an HTS winding becomes somewhat uniform. However, the current distribution is still "non-uniform." This phenomenon can also be elucidated by referring to J_c variation provided in Figure 4.16. From I_{op}=50 A to 150 A, there is a notable difference in J_c according to the field dependency, while the marginal difference is confirmed when $I_{op} > 150$ A. Bean's theory may support this argument. According to the theory, current density depends on I_c distribution.

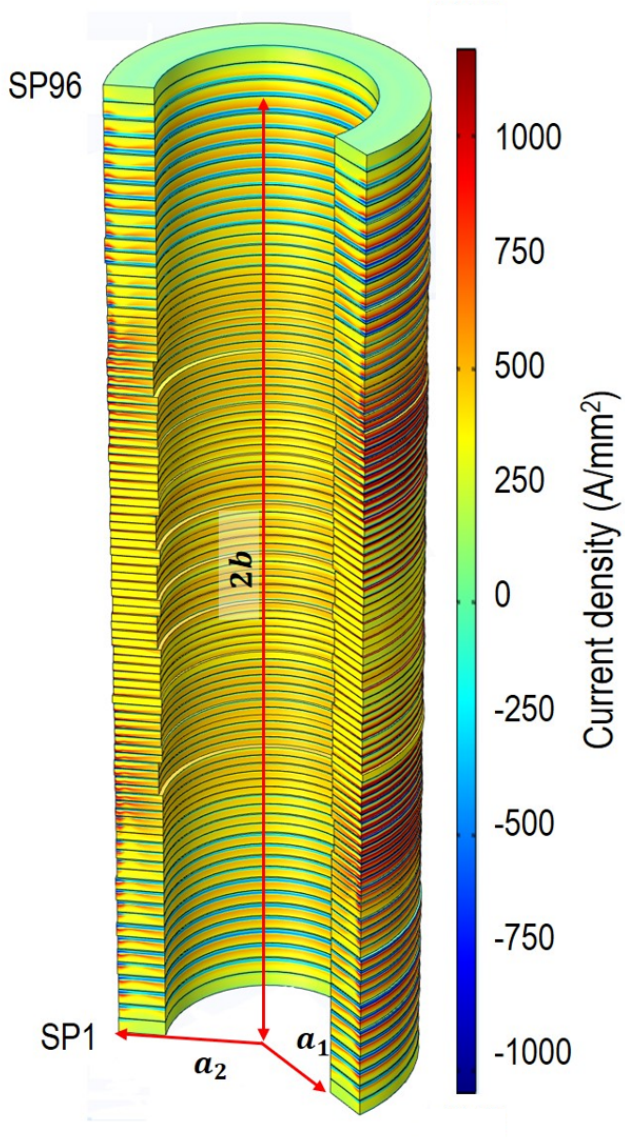

Figure 4.11: Simulation results of non-uniform current distribution in the 9.4 T HTS NMR magnet.

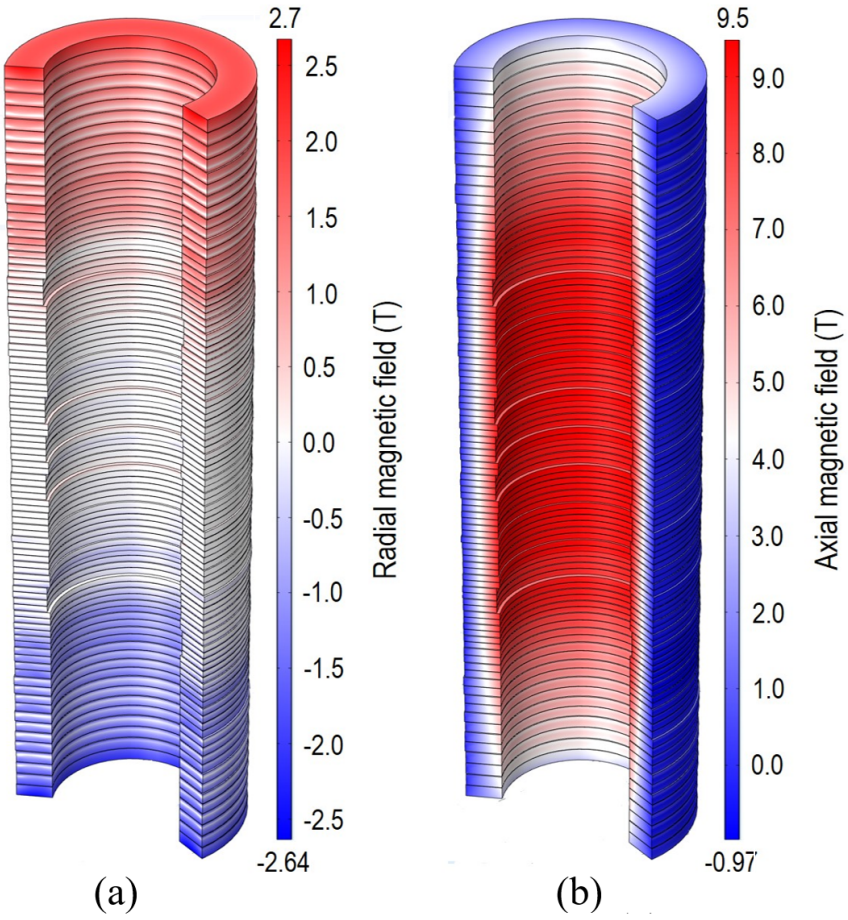

Figure 4.12: Simulation results of (a) axial and (b) radial magnetic fields in the 9.4 T HTS NMR magnet.

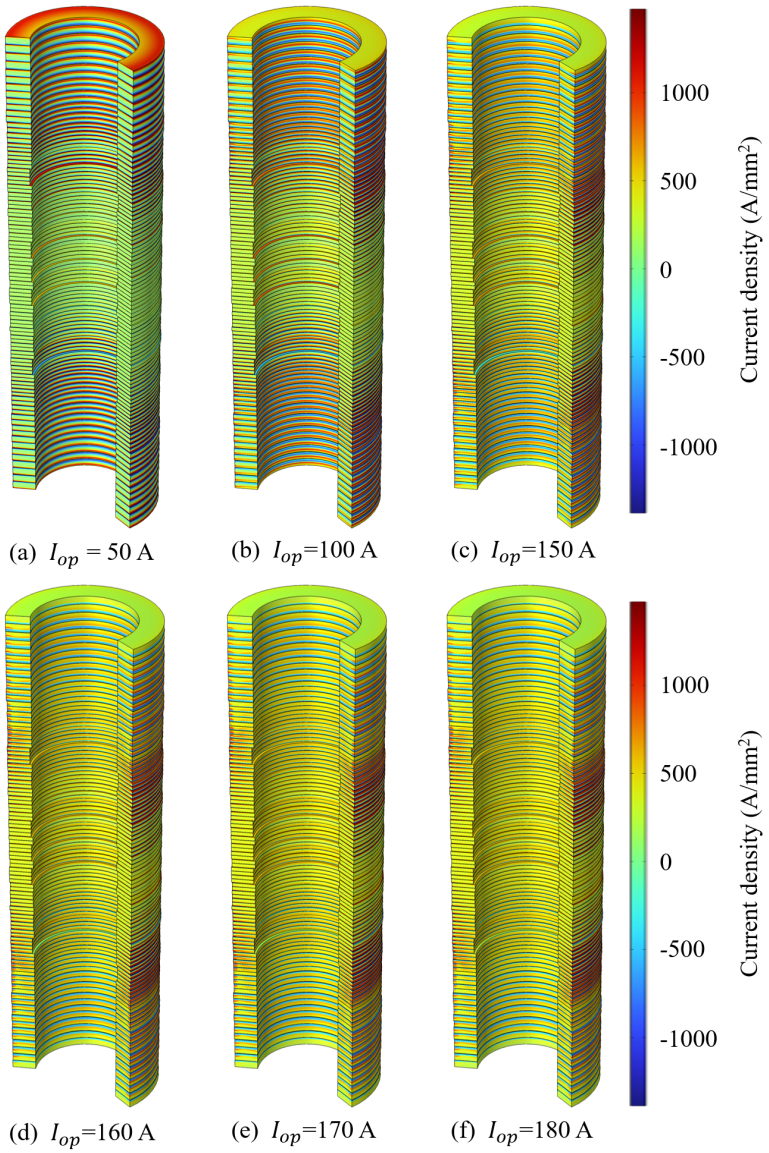

Figure 4.13: Simulation results of total current density in the 9.4 T HTS NMR magnet according to the operating current.

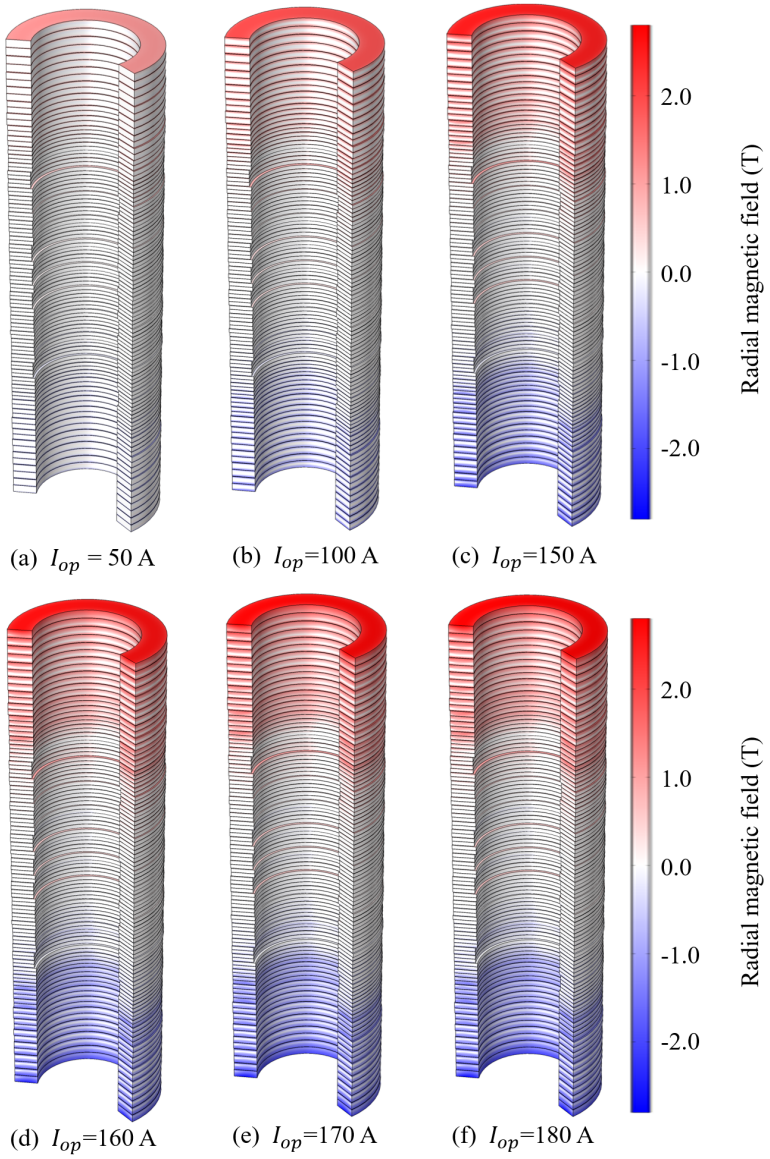

Figure 4.14: Simulation results of radial magnetic fields in the 9.4 T HTS NMR magnet according to the operating current.

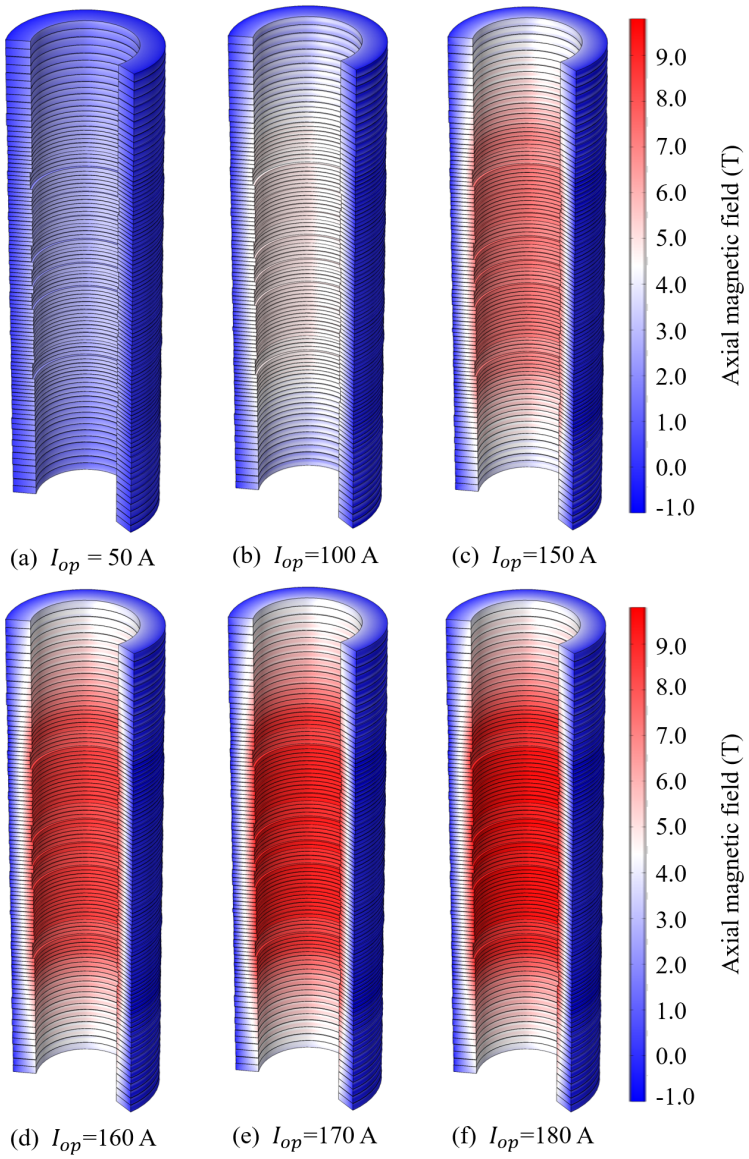

Figure 4.15: Simulation results of axial magnetic fields in the 9.4 T HTS NMR magnet according to the operating current.

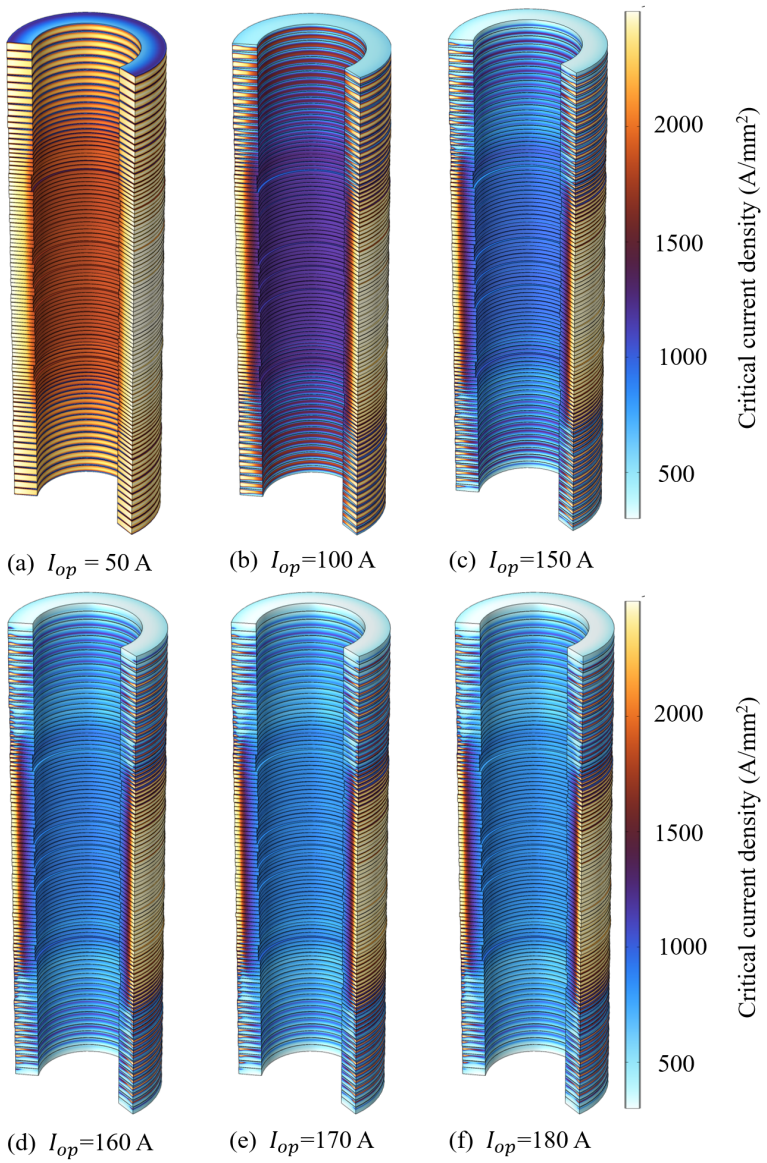

Figure 4.16: Simulation results of field-dependent critcial current density $J_c(B,T)$ distribution in the 9.4 T HTS NMR magnet according to the operating current.

Nonlienar inductance variation by screening current relaxation

The inductance of a conventional LTS magnet has been widely believed that it is not changed, assuming quasi-steady state operation. The argument may be initiated from the assumption of uniform current distribution. However, it may be invalid to an HTS magnet since the non-uniform current density is distributed due to screening current. The nonlinear inductance variation is indeed discovered by measuring module coil terminal voltages. The module coil terminal voltages of the 9.4 T HTS NMR magnet also presented the nonlinear behaviors. The measure results suggest that the behavior depends on the operating current flowing in the magnet. Hence, the nonlinear inductive voltage behaviors were studied using the numerical simulation methods provided in chapter 3. Here, "equivalent" inductance is defined. It is the total sum of self and mutual inductances of a module coil; it is a "reasonable" assumption in consideration of the situation that the operating current is equal to the current flowing in HTS tapes where marginal turn-to-turn leak current due to NI configuration exists. The calculation results of the "equivalent" inductance of module coils in the 9.4 T HTS NMR magnet are provided in Figure 4.17. They are used to perform a circuit simulation, and the simulated results are compared with measured ones. In detailed results of calculated self and mutual inductances between module coils are summarized in Figure 4.18. In Figure 4.18, left plots present self and mutual inductances of 24 module coils—a module coil is a stack of two DP coils— and right plots present errors between calculated results with screening current and those without screening current. The error was calculated with:

$$\text{error } [\%] = \frac{M_{i,j}^{sc} - M_{i,j}^{ideal}}{M_{i,j}^{ideal}} \times 100, \tag{4.2}$$

where $M_{i,j}^{sc}$ and $M_{i,j}^{ideal}$ stand for mutual inductance between i$^{\text{th}}$ module coil and j$^{\text{th}}$ module coil considering non-uniform current density due to screening current, and that considering uniform current density.

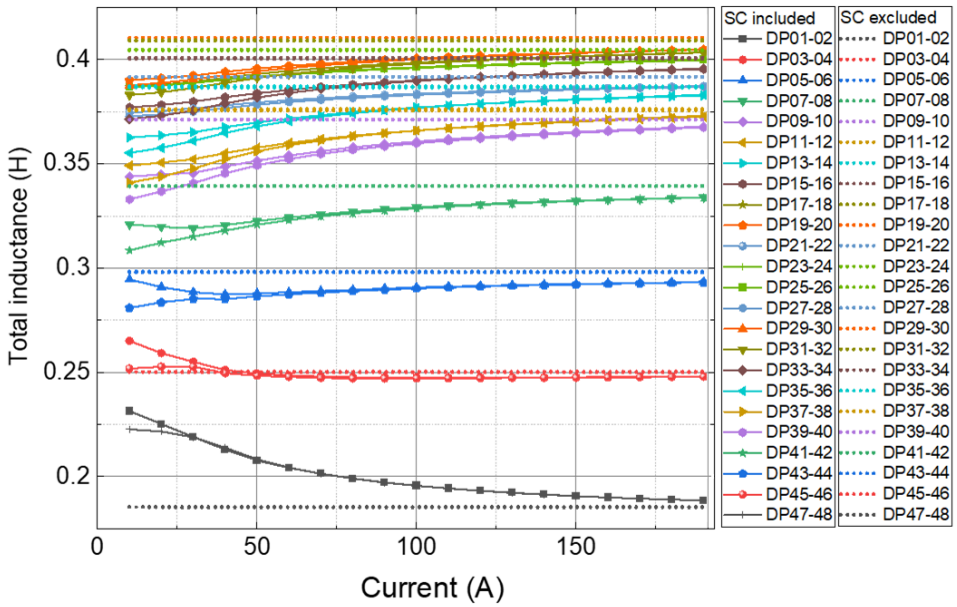

Figure 4.17: Numerical simulation results of time-varying “equivalent” inductance of each module coil in the 9.4 T HTS NMR magnet according to the operating current.

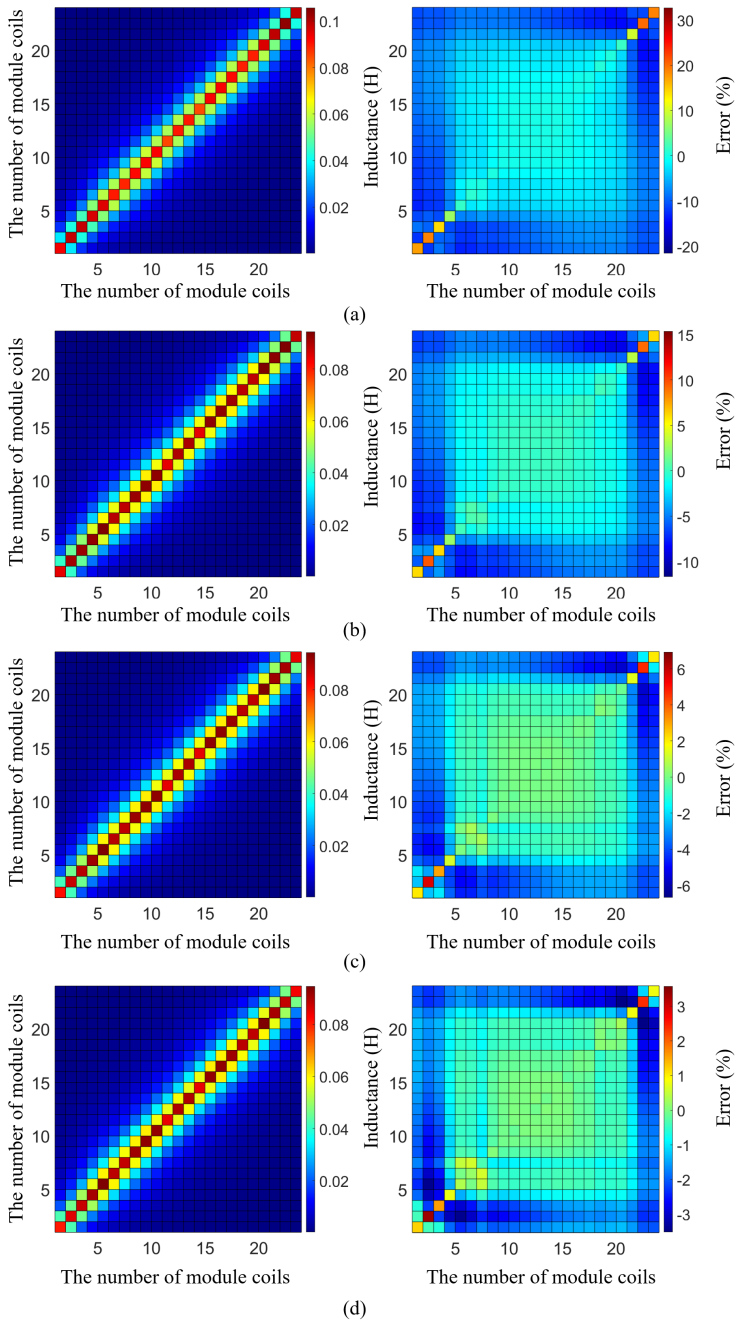

Figure 4.18: Calculated self and mutual inductances of module coils in the 9.4 T HTS NMR magnet when I_{op}=: (a) 50 A; (b) 100 A; (c) 150 A; and (d) 185 A.

Nonlienar spatial and temporal magnetic fields with SCF

The "precision" of numerical simulation of screening current may be assessed by the field mapping result mainly due to the impacts of SCF on spatial and temporal magnetic field behaviors. Accordingly, the detrimental impacts of SCF on the spatial and temporal magnetic fields in a bore of the 9.4 T HTS NMR magnet were described using the numerical simulation methods. An optimal operation protocol adopting 15 times current sweep reversal (CSR) techniques—CSR is a current control technique. Field mapping results were analyzed to demonstrate the validity of using numerical simulation methods in terms of spatial and temporal magnetic field behaviors. The CSR technique is well-known for suppressing substantial screening current in an HTS magnet and consequently improving spatial and temporal electromagnetic reliability and stability. After the CSR operation, the temporal magnetic field stability to obtain an NMR signal was acquired in the actual measurement. Figure 4.19 provides the measured results of operating current measured from the power supply terminal, total magnet voltage measured from the HTS magnet terminal, and field mapping results along the magnet axis. Figure 4.20 presents calculated total current density in the upper half, including transport current and screening current, that depends on the number of applied CSR. Figure 4.20 presents calculated total current density in the upper half, including transport current and screening current, that depends on the number of applied CSR; Figure 4.20(a) for the first quarter of the HTS magnet; and (b) for the second quarter. Although construction errors between the upper and bottom halves of the magnet are not equal, the difference in terms of the non-uniform current distribution in the magnet between them is insignificant, so the upper half is only provided in Figure 4.20. Figure 4.21 provides transient response of spatial magnetic field. It may demonstrate quantitatively the CSR effect on the spatial magnetic field that increases the magnetic field intenstiy and field uniformity by suppressing screening current in an HTS magnet and thus improving uniformity of current distribution in an HTS magnet, as shown in Figure 4.20.

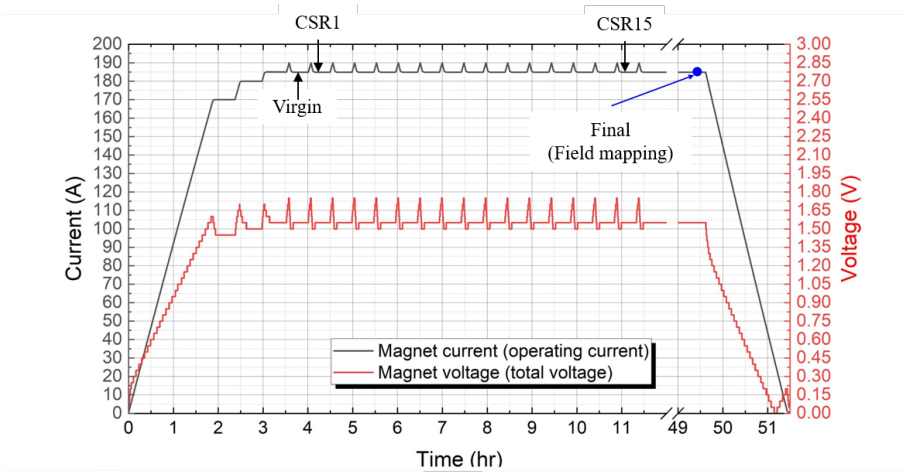

(a)

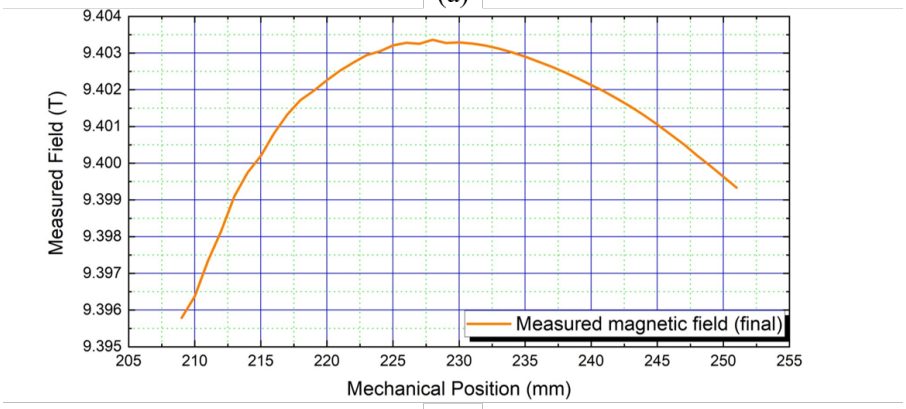

(b)

Figure 4.19: (a) Measured results of operating current measured from the power supply terminal, total magnet voltage measured from the HTS magnet terminal. (b) Field mapping results along the magnet axis.

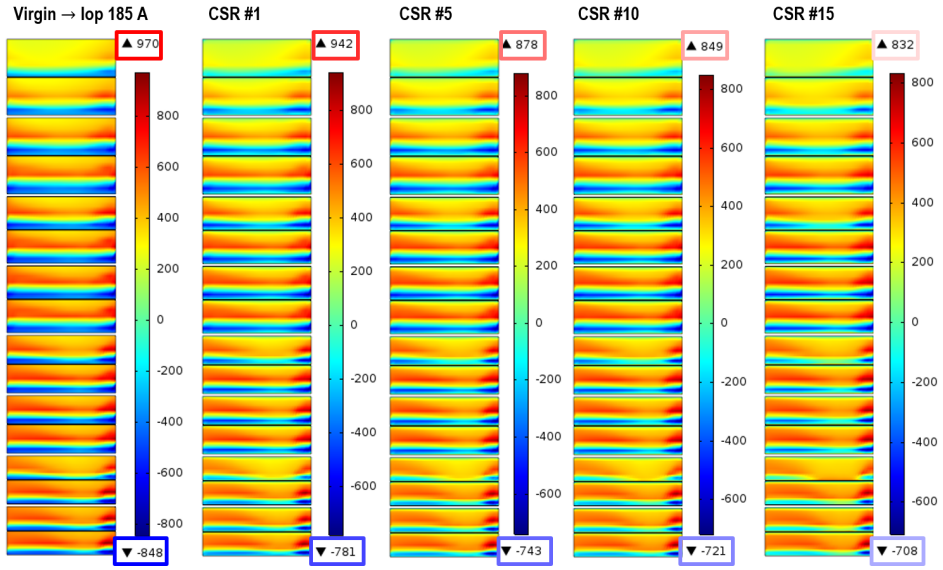

(a)

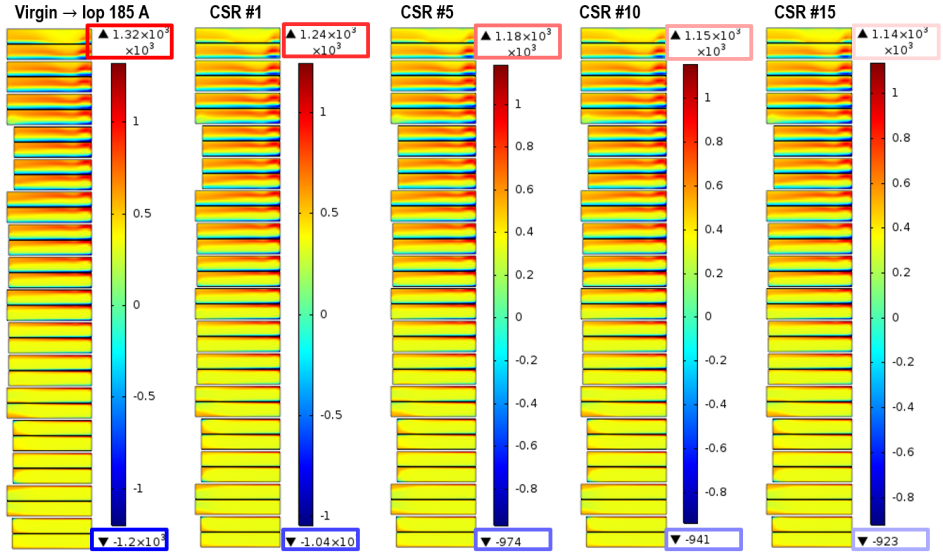

(b)

Figure 4.20: Calculated total current density in the upper half: (a) the first quarter of the HTS magnet; and (b) the second quarter of the HTS magnet.

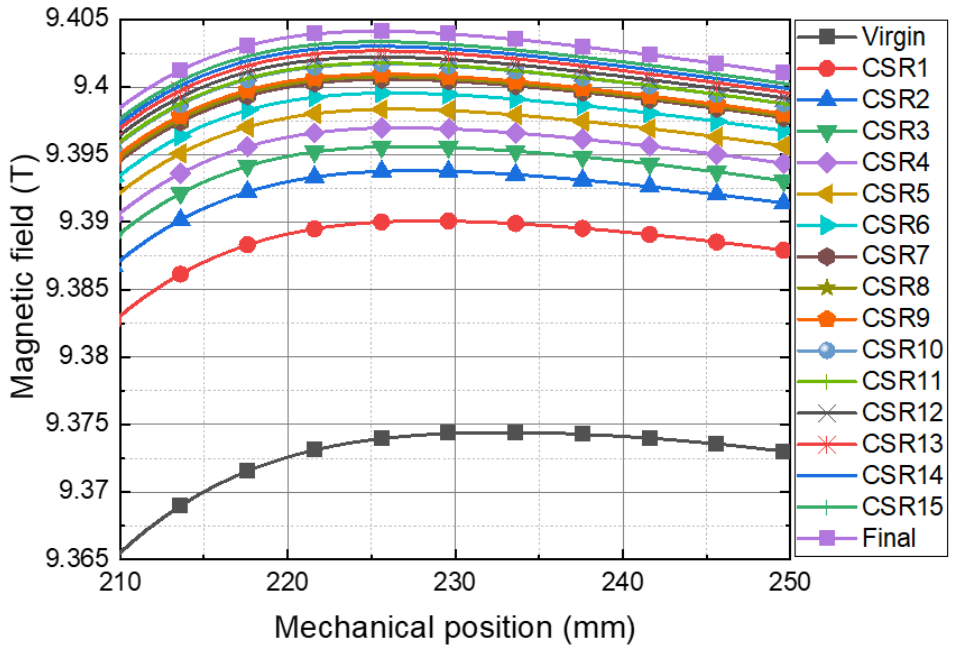

Figure 4.21: Simulation results of the transient response of spatial magnetic field depending on the number of CSR applications.

Mechanical stress distribution with SCS

Figure 4.22 presents numerical simulation results of mechanical stress (hoop stress only) and the mechanical strain (magnetic stress considered only) in the 9.4 T HTS NMR magnet. In this analysis, the magnetic force, Lorentz force of $\mathbf{J} \times \mathbf{B}$, was considered. The peak mechanical hoop stress is 120 MPa assuming the uniform current density in each HTS coil, while it becomes 600 MPa with non-uniform current density due to screening current incorporated. Fortunately, since the peak value is less than the 95% I_c retention stress of HTS tapes, which is about 700 MPa, it is expected that the HTS magnet operates well without any mechanical stability issue. The expectation agrees well with the actual operating results—the magnet has indeed stably operated without any electric and mechanical failures since the first charge in 2018.

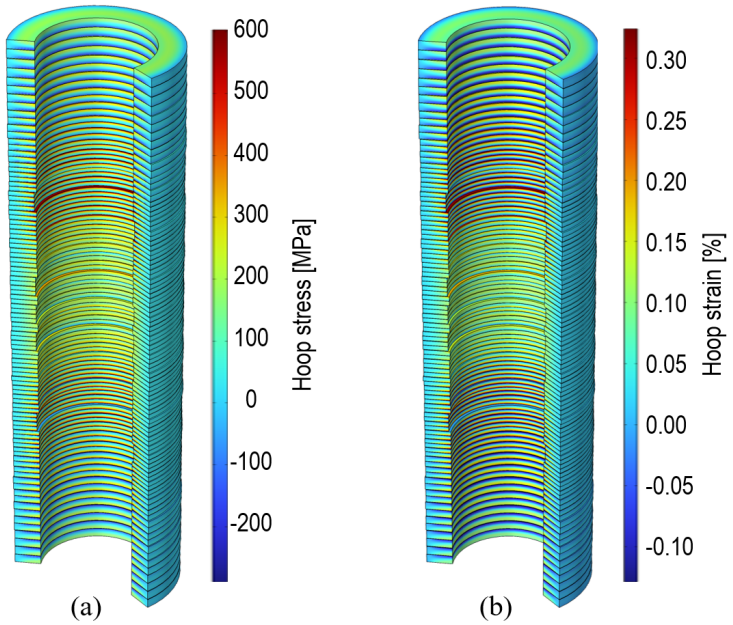

Figure 4.22: Simulation results of mechanical stress distribution and the consequent mechanical strain in the 9.4 T HTS NMR magnet.

4.3.3 Comparison between simulation and measurement results

Coil terminal voltages

A modified lumped-circuit model is proposed to consider the nonlinear inductance of each module coil, Figure 4.23. Then, coil terminal voltages of individual module coils in the 9.4 T HTS NMR magnet are described using a circuit network shown in Figure 4.24. Each module coil, a stack of two DP coils, is represented using one inductor and two resistors. One connected with the inductor in series presents the resistance, including the HTS resistance and DP-to-DP joint resistance, and the other presents the contact resistance. Meanwhile, the resistor between adjacent module coils stands for the joint resistance between them. The comparison results between simulation and measurement are provided in Figures 4.25–4.29; Figures 4.27–4.29 present enlarged views of coil voltages and the central magnetic field for a selected time interval.

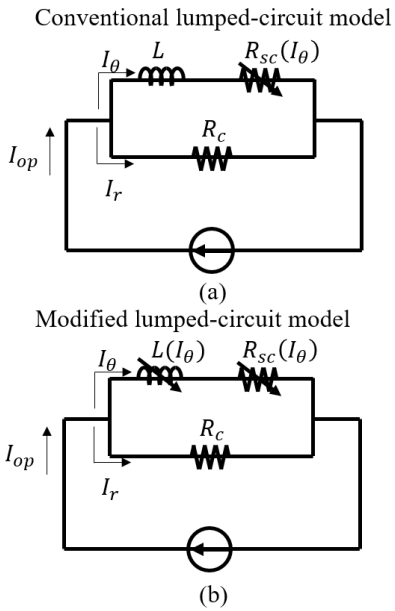

Figure 4.23: Equivalent lumped-circuit model of a module coil: (a) conventionally used model; (b) modified model (proposed).

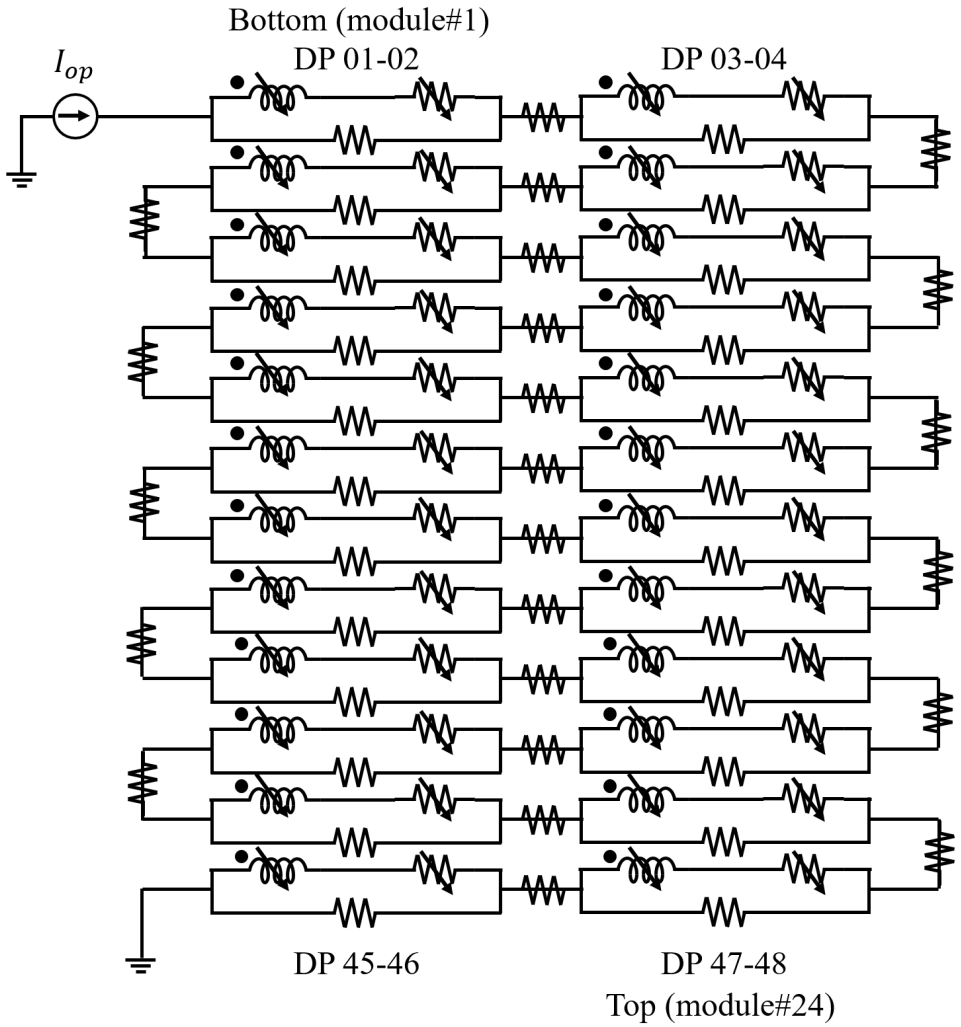

Figure 4.24: Equivalent circuit model for nonlinear numiercal analysis of current and voltage behavior in the 9.4 T HTS NMR magnet.

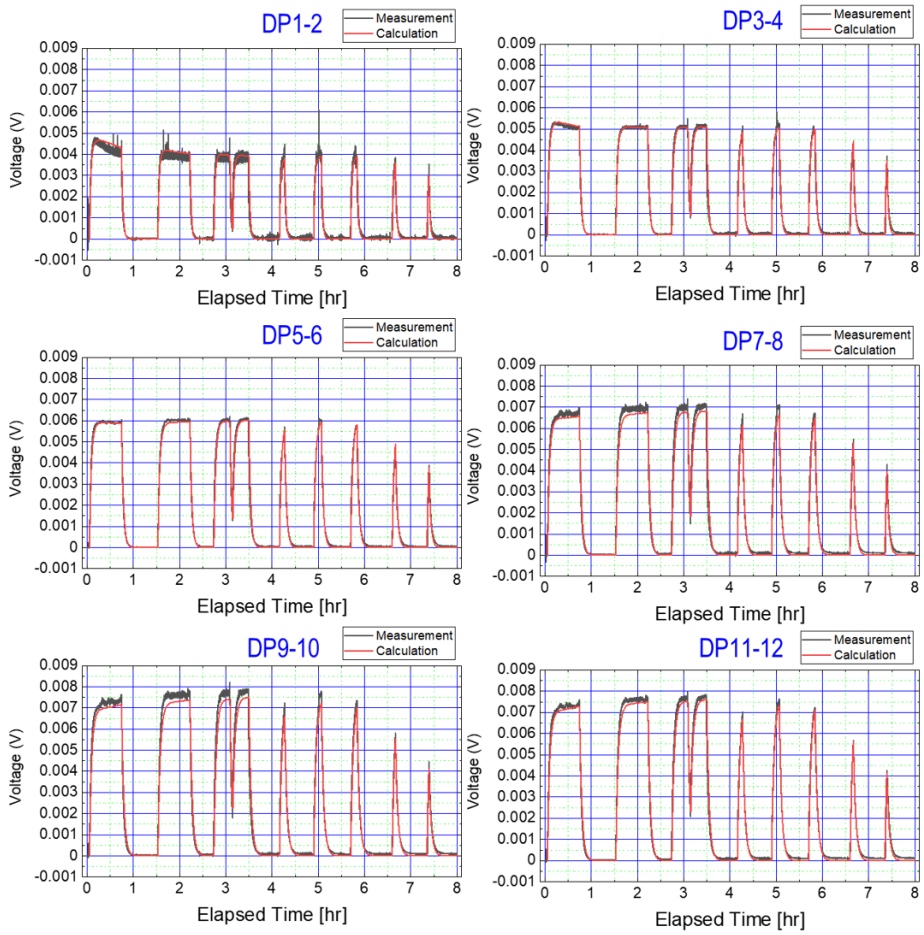

Figure 4.25: Nonlinear voltage behaviors of DP01-02, DP03-04, DP05-06, DP07-08, DP09-10, and DP11-12.

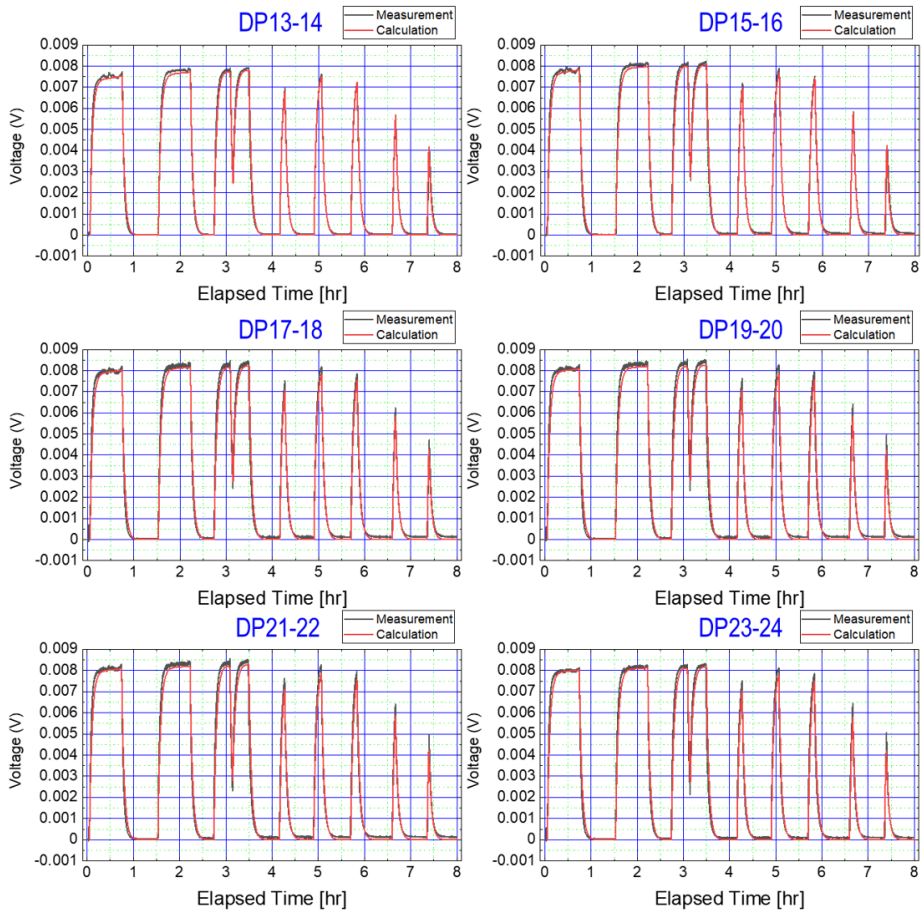

Figure 4.26: Nonlinear voltage behaviors of DP13-14, DP15-16, DP17-18, DP19-20, DP21-22, and DP23-24.

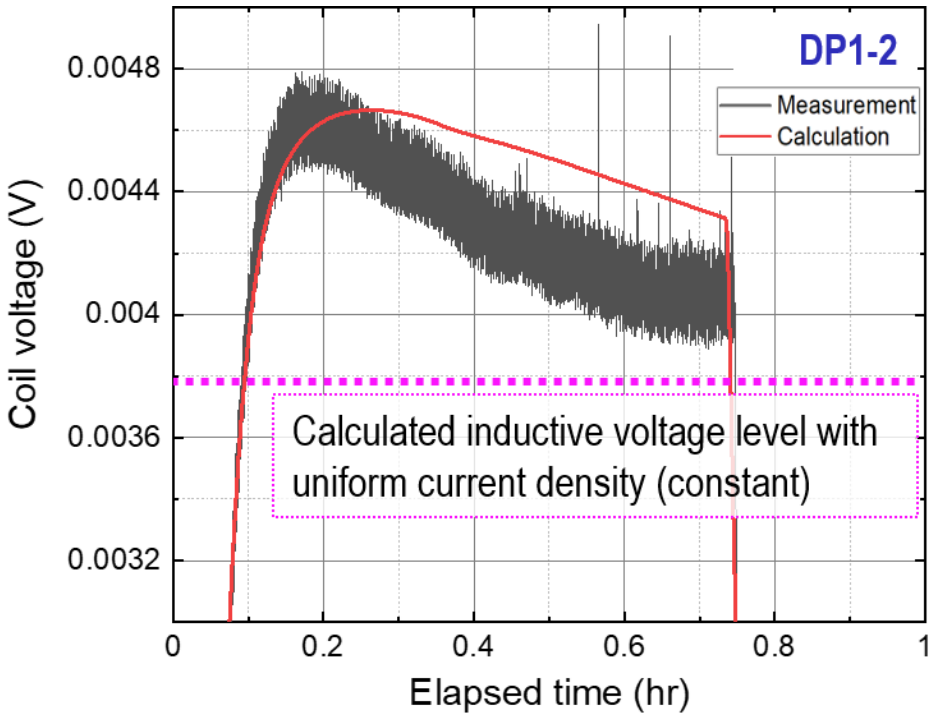

Figure 4.27: Enlarged view of a module coil voltage (DP1–2).

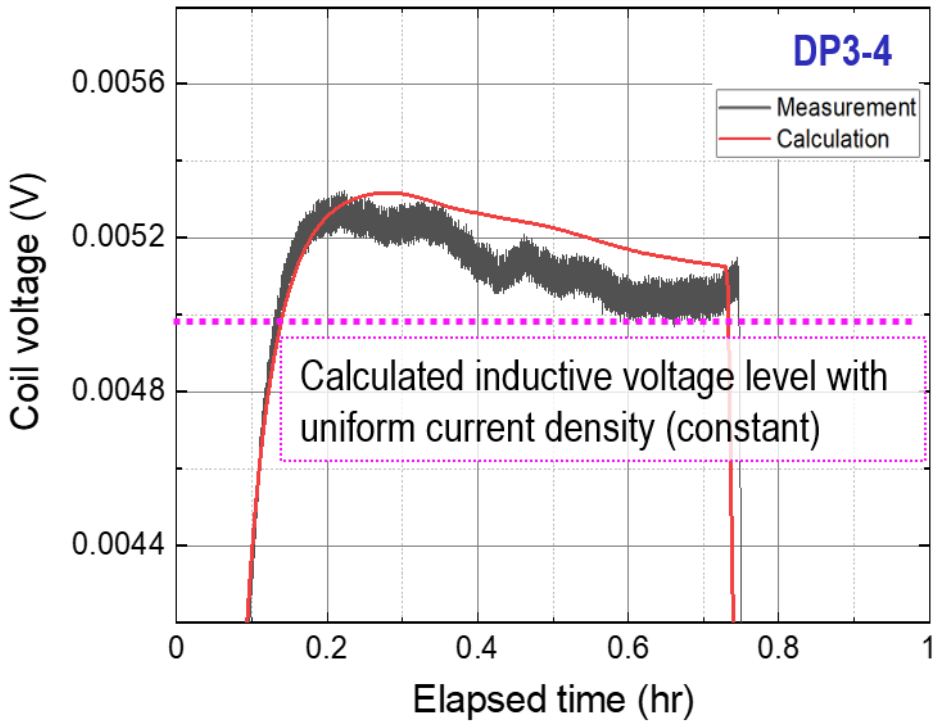

Figure 4.28: Enlarged view of a module coil voltage (DP3–4).

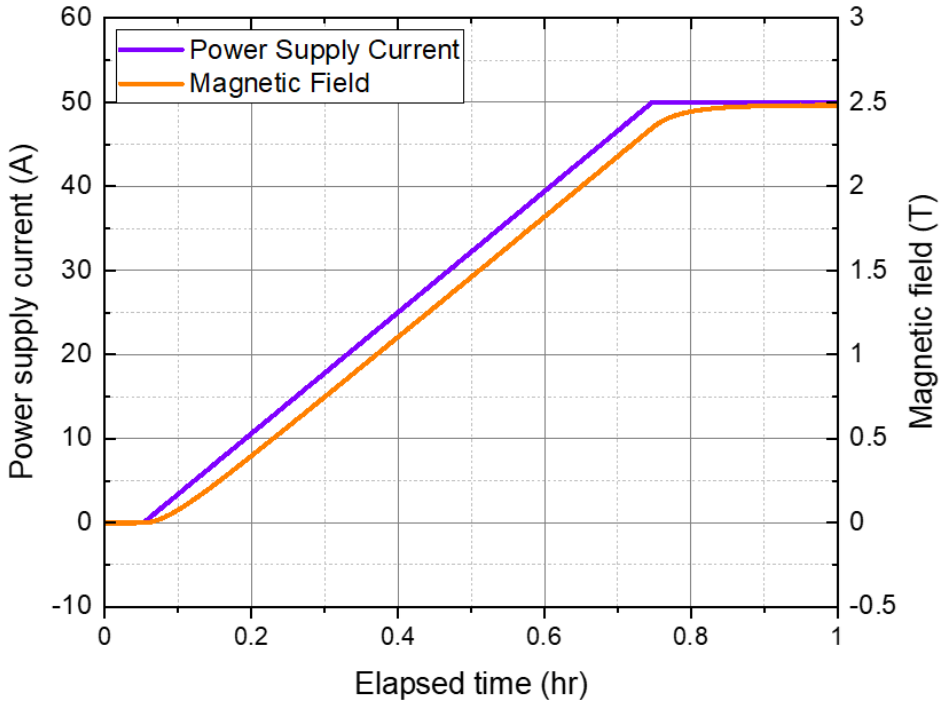

Figure 4.29: Enlarged view of operating current and magnetic field at center.

Here coil terminal voltages of the lower half were representatively provided in consideration of the symmetry feature of the magnet. Inductive voltages of DP1–2 and DP3–4 present that the magnitude decreases; others present that the magnitude increases. As shown in enlarged views of coil voltages, the signal-noise-ratio of coil voltage is at most 5%. However, as shown in the enlarged view of the central magnetic field, the ratio is far less than 1%. It implies that the voltage noise might not affect the "effective" current distribution in module coils. Meanwhile, excluding the nonlinear inductance variation, coil voltage behaviors may not be described. In conclusion, the proposed simulation methods can explain the nonlinear behaviors of inductance.

Field mapping of spatial magnetic fields

Figure 4.30(a) presents the comparison result between calculation (a blue line with triangles) and measurement (a black line with squares) in terms of field mapping results along the magnet axis. Note that z=250 mm in the mechanical position is the magnet center. The difference in the peak magnitude of the field intensity between calculation and measurement is 2 mT. The error between the difference and the peak value of measured field intensity is about 200 ppm. Figure 4.30(a) suggests that although there is a discrepancy in the magnitude, the field gradient seems reasonably consistent between calculation and measurement. Thus, measured and calculated results in Figure 4.30(a) were normalized by their peak value, and the results are shown in Figure 4.30(b). It compares the measurement and calculation. The design results (normalized by 9.4 T) are also added to confirm the SCF effects on the field gradient. The field gradient near the magnetic center (z=250 mm) is approximately zero in the design stage. However, the field gradient and the magnitude are significantly changed mainly due to screening current. It was found that the magnetic center moved to z=230 mm during the field mapping process.

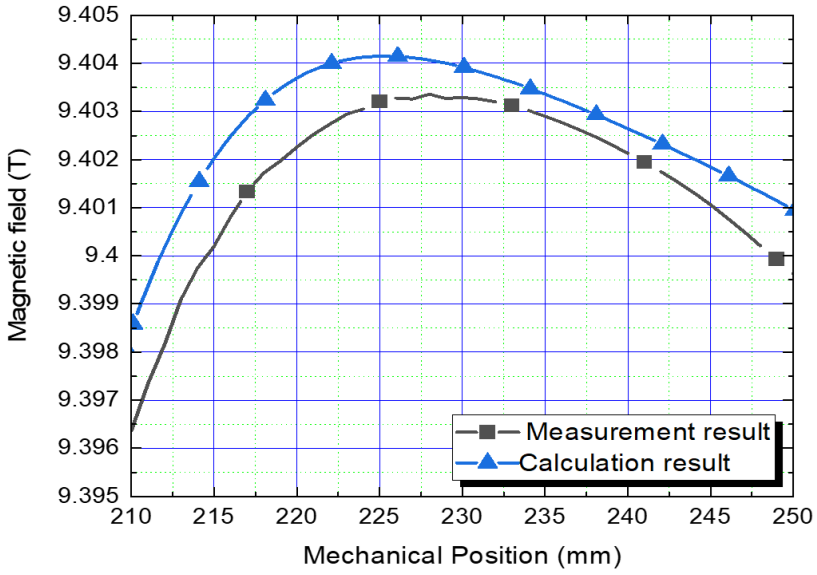

(a)

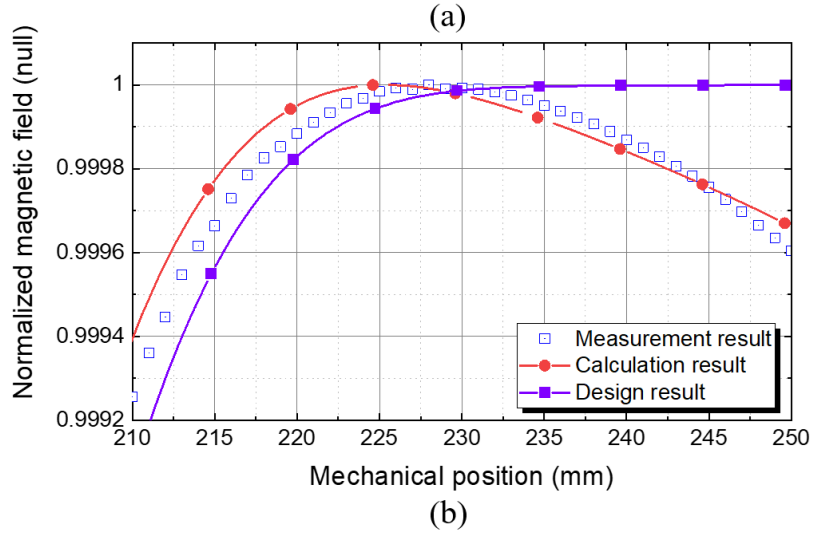

(b)

Figure 4.30: Comparison result between calculation and measurement of field mapping results along the magnet axis: (a) axial magnetic field; (b) normalized field.

Spatial field uniformity and temporal field stability

Table 4.5 provides the spatial and temporal behavior of the magnetic field in a bore of the 9.4 T HTS NMR magnet. The table offers nonlinear numerical analysis results of harmonic analysis using the segmentation method. There are seventeen CSRs applications to improve the magnetic field uniformity and stability. The measured field uniformity is 123 ppm at the field mapping, while the calculated one is 107 ppm. The

Table 4.5: Calculation results of zonal harmonic coefficients up to the sixth order.

	The n^{th} order zonal harmonic coefficients: Z_n [T/m$^{\text{n}}$]						
	Z_0	Z_1	Z_2	Z_3	Z_4	Z_5	Z_6
Virgin	9.372	$1.997{\cdot}10^{-1}$	-4.401	8.206	$0.2204{\cdot}10^{2}$	$8.689{\cdot}10^{2}$	$2.594{\cdot}10^{4}$
CSR1	9.387	$2.003{\cdot}10^{-1}$	-3.028	8.248	$0.7946{\cdot}10^{2}$	$8.495{\cdot}10^{2}$	$0.1853{\cdot}10^{4}$
CSR2	9.390	$2.001{\cdot}10^{-1}$	-2.721	8.263	$1.063{\cdot}10^{2}$	$8.452{\cdot}10^{2}$	$-0.5120{\cdot}10^{4}$
CSR3	9.392	$2.006{\cdot}10^{-1}$	-2.543	8.272	$1.241{\cdot}10^{2}$	$8.425{\cdot}10^{2}$	$-0.9461{\cdot}10^{4}$
CSR4	9.393	$2.006{\cdot}10^{-1}$	-2.434	8.279	$1.362{\cdot}10^{2}$	$8.408{\cdot}10^{2}$	$-1.226{\cdot}10^{4}$
CSR5	9.395	$2.007{\cdot}10^{-1}$	-2.326	8.285	$1.483{\cdot}10^{2}$	$8.391{\cdot}10^{2}$	$-1.505{\cdot}10^{4}$
CSR6	9.396	$2.007{\cdot}10^{-1}$	-2.250	8.290	$1.573{\cdot}10^{2}$	$8.378{\cdot}10^{2}$	$-1.706{\cdot}10^{4}$
CSR7	9.397	$2.007{\cdot}10^{-1}$	-2.188	8.295	$1.651{\cdot}10^{2}$	$8.398{\cdot}10^{2}$	$-1.876{\cdot}10^{4}$
CSR8	9.397	$2.007{\cdot}10^{-1}$	-2.135	8.298	$1.717{\cdot}10^{2}$	$8.359{\cdot}10^{2}$	$-2.018{\cdot}10^{4}$
CSR9	9.397	$2.008{\cdot}10^{-1}$	-2.081	8.301	$1.782{\cdot}10^{2}$	$8.349{\cdot}10^{2}$	$-2.161{\cdot}10^{4}$
CSR10	9.398	$2.008{\cdot}10^{-1}$	-2.039	8.304	$1.838{\cdot}10^{2}$	$8.342{\cdot}10^{2}$	$-2.279{\cdot}10^{4}$
CSR11	9.398	$2.008{\cdot}10^{-1}$	-1.999	8.306	$1.889{\cdot}10^{2}$	$8.334{\cdot}10^{2}$	$-2.389{\cdot}10^{4}$
CSR12	9.398	$2.008{\cdot}10^{-1}$	-1.965	8.309	$1.934{\cdot}10^{2}$	$8.328{\cdot}10^{2}$	$-2.485{\cdot}10^{4}$
CSR13	9.399	$2.009{\cdot}10^{-1}$	-1.931	8.311	$1.979{\cdot}10^{2}$	$8.321{\cdot}10^{2}$	$-2.581{\cdot}10^{4}$
CSR14	9.399	$2.009{\cdot}10^{-1}$	-1.901	8.314	$2.020{\cdot}10^{2}$	$8.316{\cdot}10^{2}$	$-2.666{\cdot}10^{4}$
CSR15	9.399	$2.009{\cdot}10^{-1}$	-1.894	8.314	$2.032{\cdot}10^{2}$	$8.315{\cdot}10^{2}$	$-2.689{\cdot}10^{4}$
Final	9.400	$2.009{\cdot}10^{-1}$	-1.877	8.316	$2.058{\cdot}10^{2}$	$8.312{\cdot}10^{2}$	$-2.742{\cdot}10^{4}$

calculated field stability is 0.041 ppm/hr on average during the CSR operations, while the measured one is 0.33 ppm/hr. The discrepancy between calculated and measured field stability may result from the so-called power supply drift. The drift of magnetic field strength was indeed improved from about ± 8 ppm/day without "Field-Lock" technology to less than ± 0.15 ppm/day with field-lock applied; the field-lock technique is a compensation technique of unstable magnetic field to fix NMR measurement frequency. Although there is a discrepancy between calculated and measured field stability, there is a good agreement in the field uniformity.

So far, numerical analysis of the 9.4 T HTS magnet for a 400 MHz NMR application has been conducted. The comparison results between analysis and measurement were provided in terms of measurable variables, such as inductive voltages and magnetic fields. There are good agreements, although a discrepancy is confirmed in the magnitude. However, the discrepancy might be significant when the conventional uniform current distribution is assumed. For instance, the nonlinear inductive voltage behavior, the field gradients variation near the magnet center, and the field profile variation can not be described without the nonlinear numerical analysis methods. Conclusively, the numerical simulation methods are validated with this study.

From this thesis, one can discuss two improvements in terms of the design and operation of an HTS magnet compared to conventional research. The first one is to consider screening current in the design stage. Here I intend to discuss the design option of an HTS magnet for MR applications. Screening current may induce the even-order spatial harmonic fields as shown in Table 4.5. Therefore, it would be nice for HTS magnet designers to design an HTS magnet to create the even-order harmonic fields in a way to compensate for harmonic errors to be induced by screening current, assuming uniform current density in the first-cut design stage. For instance, if the magnet were designed to generate positive Z_2, negative Z_4, and positive Z_6, considering the simulation results, the 9.4 T HTS magnet would create better uniform magnetic fields in a target space. The second one is to suggest an optimal magnet operation protocol.

The 9.4 T HTS NMR magnet demonstrated that CSR is a practical option to mitigate screening current with magnet operation. Then, it is feasible to design the current operation protocol to maximally mitigate screening current using the proposed simulation methods with the magnet operation stability, e.g., the cooling power margin, considered. For instance, this thesis provides a numerical method to simulate current and voltage behaviors. With the method, it would be possible to estimate time-dependent AC loss and the consequent heat flux distribution in a conduction cooling system. It implies that optimal CSR operation can be designed considering the thermal stability of an HTS magnet in a conduction cooling system. Meanwhile, it is widely known that an optimal method is to charge the operating current of the magnet as close as possible to the critical current of the magnet and then return to the target current. The key role of the provided simulation methods is to calculate the maximum target current value that can be determined by heat loss for the optimal CSR operation protocol.

Chapter 5

A Customized Heater to Mitigate Screening Current in HTS Coil by Optimal Temperature Control

Here I report a customized electric heater, named "Thermal Eraser", to mitigate the screening current as a practical solution. The key idea is the optimal control of spatial temperature distribution in an HTS coil by using a Thermal Eraser. For the validation of the proposed idea, a superconducting module (HTS test coil + Thermal Eraser) was designed, fabricated, and tested with a conduction-cooling cryogenic facility. From the test results, the feasibility of using the Thermal Eraser to suppress screening current was demonstrated in terms of two aspects: first, the creation of the designated spatial temperature distribution within the HTS test coil as designed, and second, the quantitative evaluation of its effectiveness in screening current reduction.

5.1 Key Concept: Optimal Control of Critical Current with a Customized Heater named "Thermal Eraser"

Thermal Eraser is a customized heater for an HTS coil to create designated spatial temperature distribution. The principle of screening current mitigation by the Thermal Eraser activation is that the activation creates designated temperature distribution,

degrades local critical current of individual windings of an HTS coil, and finally, mitigates screening current. This mechanism is based on the nature of screening current that the magnitude of screening current depends on the magnitude of critical current. In order to implement the idea, the following steps are needed: first, estimate the critical current distribution of individual windings in a given HTS test coil; second, calculate optimal temperature distribution to make critical currents of individual windings equal (or similar); third, design a customized heater (hereafter Thermal Eraser) that create the designated temperature distribution; fourth, assemble an HTS test coil and a Thermal Eraser; and last, test the superconducting coil module.

Figure 5.1 shows a key concept of Thermal Eraser. There are an HTS test coil (grey in Figure 5.1), and a Thermal Eraser (dark red heater wires in Figure 5.1) that creates a *designated* spatial temperature distribution (color gradient ranging red to yellow in Figure 5.1) in the test coil. Figure 5.2 describes the principle of the Thermal Eraser.

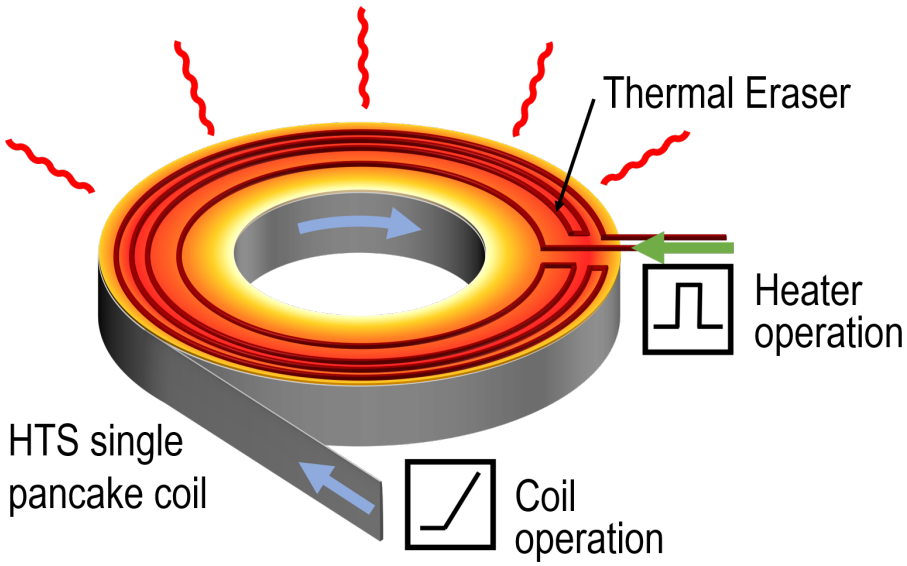

Figure 5.1: Schematic drawing of a superconducting coil module including a Thermal Eraser and an HTS coil.

It presents an example of local temperature and critical current distributions at each turn of a coil. T^{init} and I_c^{init} are initial temperature and critical current distributions before activation of the Thermal Eraser. T^{tar} and I_c^{tar} are target temperature and critical current distributions after activation of the Thermal Eraser. In most HTS magnets, T^{init} may be assumed to be spatially uniform during a nominal steady-state operation. The key design philosophy is to "control" the spatial distribution of T^{tar} in a way to make I_c^{tar} to be lower than I_c^{init} and spatially uniform in an ideal case. As a result, the spatial pattern of T^{tar} becomes similar to that of I_c^{init} but not completely "identical" since the field and temperature dependence of the critical current of HTS, which must be considered in the design of Thermal Eraser, is not linear. r in Figure 5.2 is defined as the radial position of each turn in the coil.

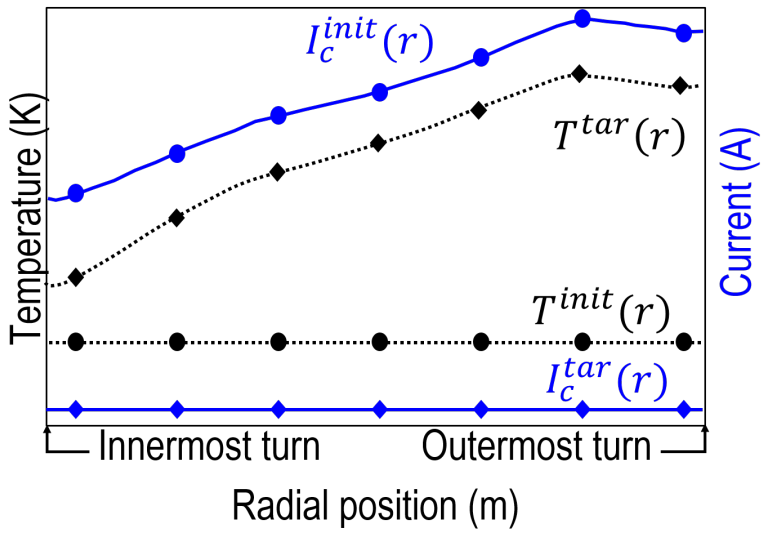

Figure 5.2: Example of local temperature and critical current distributions at each turn of a coil; T^{init} and I_c^{init} are, respectively, initial temperature and critical current distributions before activation of the Thermal Eraser and T^{tar} and I_c^{tar} are, respectively, target temperature and critical current distributions after activation of the Thermal Eraser.

5.2 Experimental Study to Validate the Feasibility of "Thermal Eraser" in Mitigating Screening Current

5.2.1 Design and simulation results

The design of a Thermal Eraser was performed with numerical simulation. First, an HTS test coil was analyzed to obtain $I_c^{init}(r)$ and $I_c^{tar}(r)$. Once the dimensions, the operating current, and initial operating temperature of the given test coil are given, magnetic fields within the coil can be calculated with numerical simulation. Table 5.1 provides the required dimensions and simulation parameters of the given test coil.

Table 5.1: Key parameters of test coil and Thermal Eraser

NI HTS test coil		
HTSwire manufacturer		SuNAM
Tape width;thickness	[mm]	4.1;0.14
Inner and outer radii	[mm]	20;83
Total number of turns		450
Operating current	[A]	50
Operating temperature	[K]	10
Self-inductance	[mH]	19.0
Characteristic resistance	[$\mu\Omega$]	126
Time constant	[s]	150
Magnet constant	[mTA^{-1}]	6.4
Thermal Eraser		
Material		SUS310
Inner and outer radii	[mm]	61;80
Number of heating lines		10
Interval between two adjacent lines	[mm]	1
NI HTS coil $\leftrightarrow$ Thermal Eraser electromagnetic interaction		
Mutual-inductance	[nH]	700

In the preliminary analysis for the Thermal Eraser design, the operating current of 50 A, the operating temperature of 10 K, and the field and temperature-dependent critical current information $I_c(B,T)$ were considered. The target of Thermal Eraser activation is to substantially suppress screening current and the consequent screening current-induced field (SCF). As a result, $I_c^{tar}(r)$ was determined to compel 50% of SCF reduction at the magnetic center of the coil considering sufficient operation margin from an unexpected quench. In this study, it is set that the design target is the reduction of not screening current but SCF because the mitigation of screening current is barely measurable unlike SCF reduction, which can be measured with Hall sensors.

Provided that the critical current is proportional to temperature at a given magnetic field, $T^{tar}(r)$ can be analytically calculated with [108]:

$$T^{tar}(r) = T^{init}(r) + [I_c^{init}(r) - I_c^{tar}(r)] \cdot \left[\frac{T_c - T_{\text{LN2}}}{I_c^{T_{LN2}}(r) - I_c^{T_c}(r)}\right], \tag{5.1}$$

where T_{LN2}, T_c, $I_c^{T_{LN2}}(r)$, and $I_c^{T_c}(r)$ stand for, respectively, liquid nitrogen temperature of 77 K, the critical temperature of 92 K, the critical current distribution in a given HTS coil at 77 K and a given magnetic field, and the critical current at the critical temperature (essentially zero). Measurement based $I_c^{T_{LN2}}(r)$ is provided in Figure 5.3.

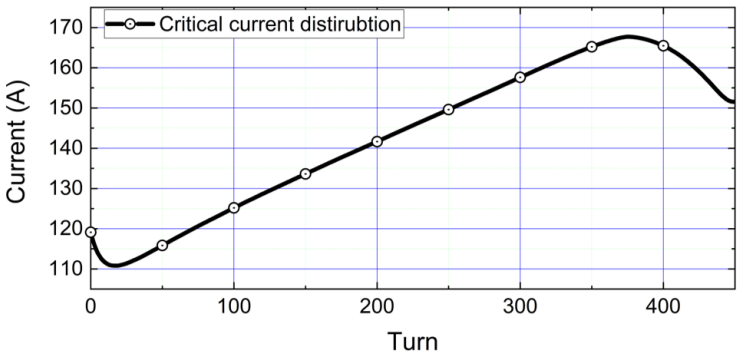

Figure 5.3: I_c distribution in the given coil considering the operating current of 50 A and measured $I_c(B, T = 77\text{ K})$ data.

The second step is to build a time-dependent numerical simulation model for implementing the $T^{tar}(r)$ in the given coil with multiple heating lines in a practical way. The COMOSL Multiphysics (thermal+electromagnetic) FEM tool was used to design and analyze the Thermal Eraser. The actual dimensions of a conduction cooling system were considered in the COMSOL model together with temperature-dependent material properties of key components, e.g., a cooling channel directly attached to the test coil and the main cooling plate attached to the main cold head of a cryocooler. Figure 5.4 presents a to-scale 2D axisymmetric COMSOL model that includes the conduction cooling stage, the HTS test coil, Thermal Eraser and instrumentations. The well-known H formulation with the domain homogenization technique [109, 111] with the power-law model for the E–J constitutive law of REBCO [136] (details are provided in chapter 3) was adopted for nonlinear numerical numerical analysis of screening current in the test coil. Meanwhile, the commonly-used heat transfer simulation module provided in the COMSOL Multiphysics was used for the simulation of temperature distribution.

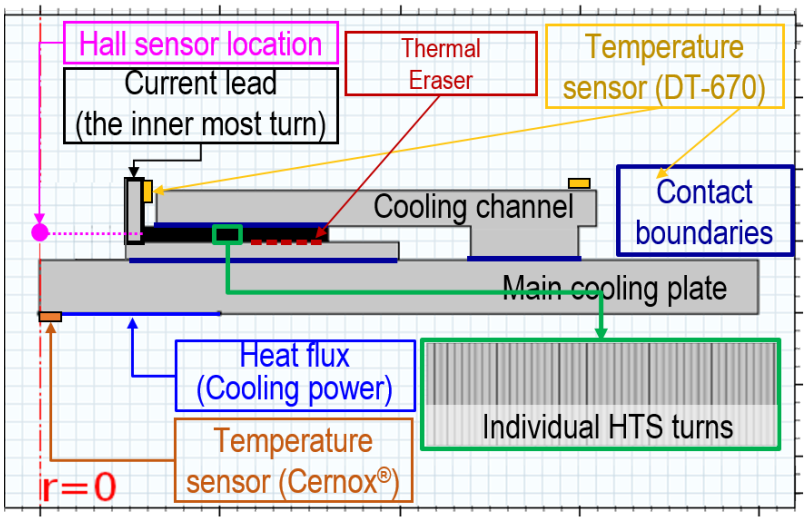

Figure 5.4: To-scale 2D axisymmetric COMSOL model that includes the conduction cooling stage, the HTS testcoil, Thermal Eraser and instrumentations.

The last step is to optimize the Thermal Eraser design. As shown in Figure 5.5, key design variables are: the number of heating lines (six in Figure 5.5), the distance between adjacent heating lines (d_{ht}), width (w_{ht}) and thickness (δ_{ht}) of each heating line, and the radial position of the innermost heating line (r_{ht}). The objective function to be minimized is defined as:

$$f^{obj} = \int |T^{sim}(r) - T^{tar}(r)|\, dr, \tag{5.2}$$

where $T^{sim}(r)$ is a simulated spatial temperature distribution in an HTS coil considering a design result of a Thermal Eraser. The genetic algorithm was adopted for the design optimization. For design simplicity, additional design constraints were determined: first, d_{ht} of the entire heating lines is identical; second, w_{ht} and δ_{ht} are set to be 1 mm and 0.1 mm, respectively; third, the Thermal Eraser is activated for 1 minute with an operating current of 1 A; and last, total resistance of the Thermal Eraser is 25 Ω in consideration of our in-house power supply rating. The design optimization results are summarized in Table 5.1. Figure 5.6 presents a comparison between $T^{tar}(r)$ and $T^{sim}(r)$ (simulated temperature distribution with the design optimization result). It shows reasonably good agreement; the average of $|T^{sim}(r) - T^{tar}(r)|$ is ∼3 K.

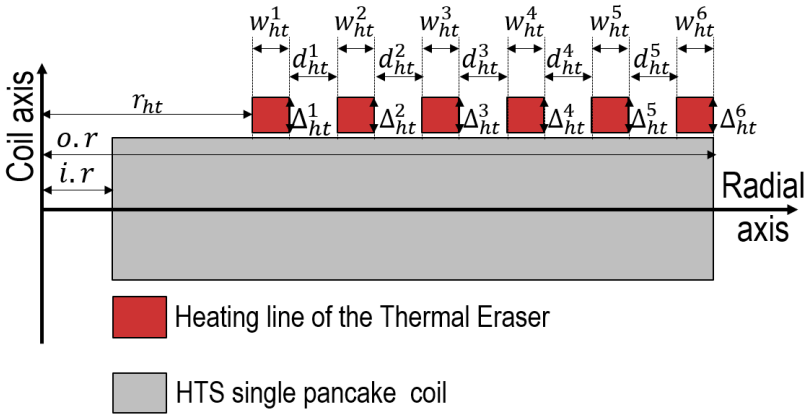

Figure 5.5: Schematic 2D axisymmetric drawing to show key design variables of Thermal Eraser.

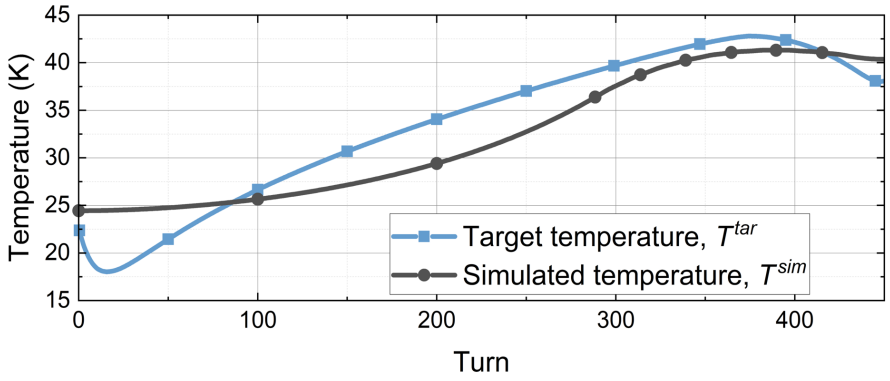

Figure 5.6: Comparison between $T^{tar}(r)$, the analytic calculation results, and $T^{sim}(r)$, the COMSOL simulation results.

5.2.2 Construction and instrumentation results

Figure 5.7 show the construction and instrumentation process in detail. In the construction phase, an HTS test coil was fabricated with the NI winding technique. During the winding, the constant winding tension of 10 kgf, measured by a sensor in a winding machine, was applied, while a "slow" winding speed, less than 5 rpm, was adopted to sustain the so-called equilibrium state in the aspect of mechanical stress distribution by the winding tension. To measure local voltages and temperatures of the coil, multiple short pieces of HTS tapes were inserted as voltage taps at every 100 turns. Although the compressive radial stress induced by the constant winding tension is sufficient to fix the taps, the electrical soldering technique was utilized to prevent detaching of the taps from the windings. After the test coil construction, key operation parameters, including characteristic resistance of the coil (the sum of all contact resistances), time constant, and magnet constant (magnetic field at the coil center with the operating current of 1 A), were measured in a liquid nitrogen bath at 77 K. The results are summarized in Table 5.1. Meanwhile, the Thermal Eraser was electrically insulated with the Kapton sheet of 100 μm thick so that the operating current for the Thermal Eraser supplied from a power source can not detour to the HTS test coil.

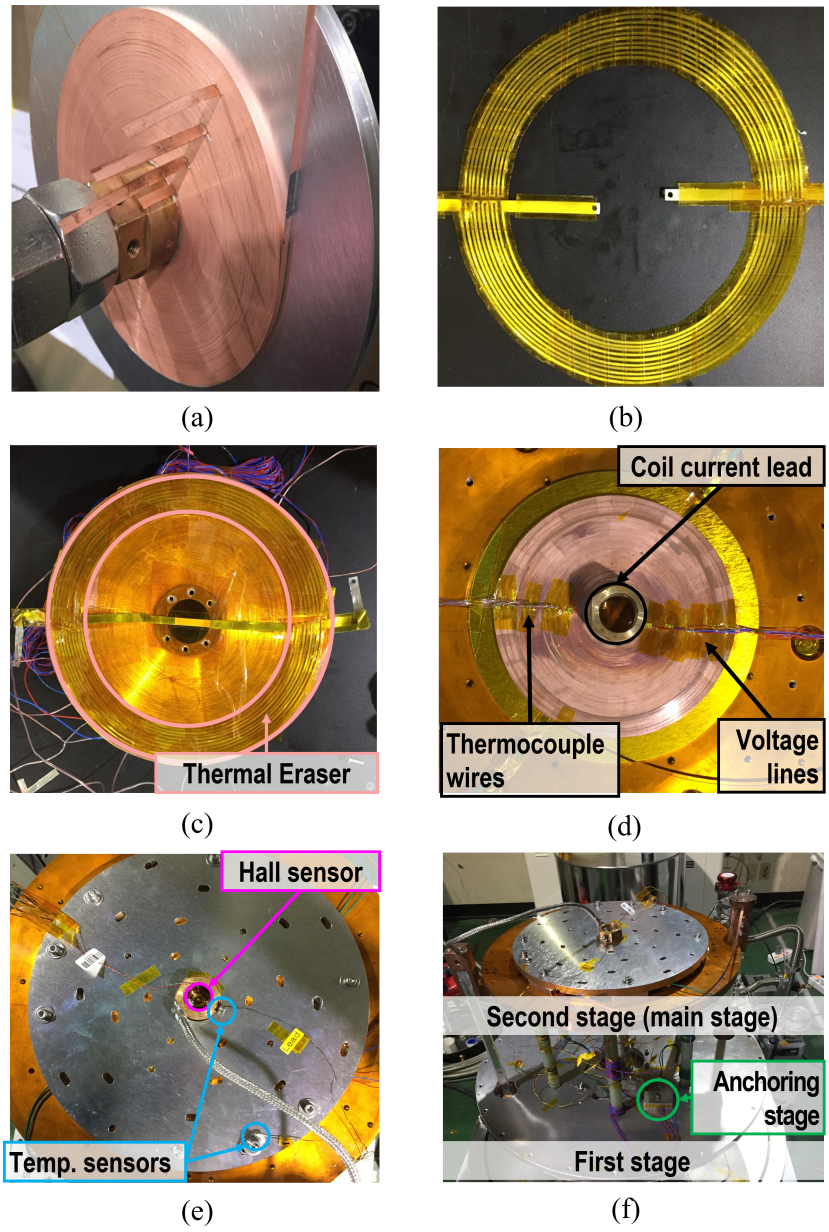

Figure 5.7: (a) Winding an NI HTS test coil and inserting pieces of REBCO tapes for REBCO taps, (b) fabricating the customized heater, (c) assembling Thermal Eraser and coil, (d) installing heater current supply lines, thermocouple wires, and voltage signal lines, (e) locating a Hall sensor and temperature sensors, and (f) final assembly.

As for the instrumentation, Table 5.2 summarizes details of selected instruments, which include each device's measurement range. Extra care was devoted to estimating the range of each signal, as the magnitude of screnning current in an HTS coil is often marginal. Figure 5.5 shows the locations of Cernox and silicon diode (DT-670) temperature sensors, and Hall sensors (HGCA 3020). As the reference temperature point for thermocouple sensors, the first stage of our in-house conduction cooling system was used as an anchoring stage. Our data acquisition (DAQ) system consists of SCXI 1000, 1125, and 1305 of the National Instruments, while a nano-voltmeter was used to improve the measurement accuracy of magnetic fields. Two types of power supplies were used, one with a small current drift for the test coil operation and the other with a fast on-off switching speed (maximum 1.3 kHz) for the Thermal Eraser operation.

Table 5.2: Specifications of instruments for the feasibility test of Thermal Eraser

Name	Model	Range
Temperature sensor I	Lake Shore Cernox®	0.10 – 325 K
Temperature sensor II	Lake Shore DT-670	1.4 – 500 K
Temperature sensor III	Lake Shore Thermocouple	3.0 – 475 K
Magnetic field sensor	Lake Shore HGCA3020	>3 T
Data acquisition	NI SCXI system	-5 – 5 V
Nano-voltmeter	KEITHELY 2182A	-100 – 100 mV
Temperature monitor	Lake Shore Model 218	0 – 7.5 V
Gaussmeter	Lake Shore Model 425	350 mG – 350 kG
Power supply I	Oxford MercuryiPS	-10 - 10 V / -240 – 240 A
Power supply II	PowerTM EX 300-12	0 – 300 V / 0 – 12 A
Power supply III	Lake Shore Model 121	100 nA – 100 mA

5.2.3 Operation and evaluation results

The superconducting coil module, including the HTS test coil and the Thermal Eraser, was tested at 7 K in a conduction cooling system. The coil was energized up to 50 A with the constant ramping rate of 0.1 As^{-1}. The Thermal Eraser was activated after a sufficient time interval (more than 20 minutes) considering the charging delay of an NI HTS coil [138]. As a result, due to the Thermal Eraser activation, local temperatures in the HTS test coil rose, and finally, the magnetic field increment was captured.

Figure 5.8–5.9 shows experimental results of temperature measured by sensors, currents, voltages, and magnetic field at the test coil center over the entire experiment. In the Figure 5.8, the peak temperature variation during charging ($0 < t < 60$ minutes, i.e., before activation of Thermal Eraser) was marginal (0.2 K), which may validate our assumption on the spatially uniform distribution of T^{init}. As shown in Figure 5.9, there is no discernible local voltage change during the Thermal Eraser operation as expected, mainly due to the marginal mutual inductance of 700 nH between the Thermal Eraser and the test coil.

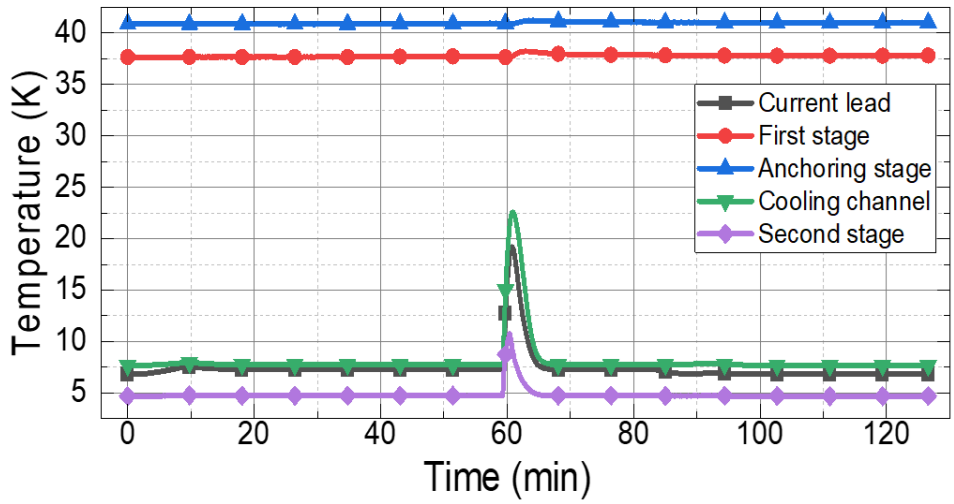

Figure 5.8: Experimental results of temperatures measured by cryogenic temperature sensors, i.e., Cernox® and DT-670.

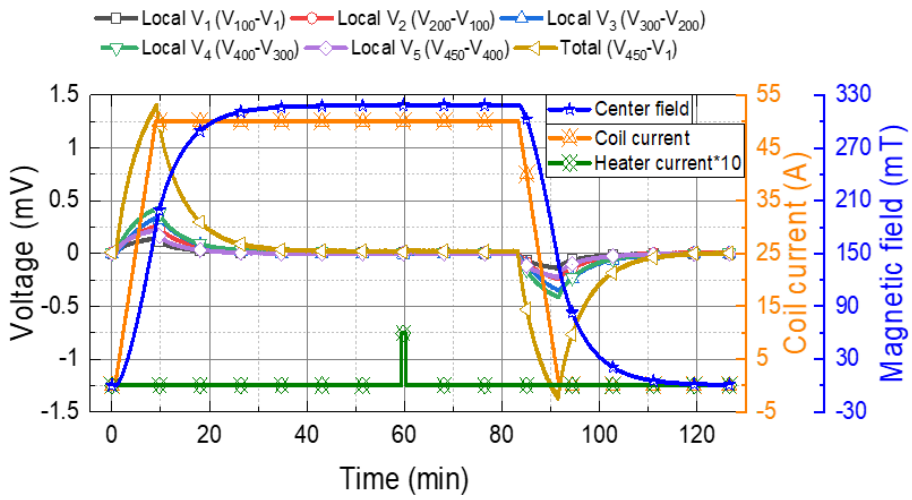

Figure 5.9: Experimental results of currents, voltages, and the magnetic field at the coil center; $V_n - V_m$ indicates the local voltage difference between n^{th} and m^{th} turns.

Figure 5.10–5.11 provides temperatures at the radial location of selected turns and the coil center field under the operation of the Thermal Eraser. As shown in Figure 5.10, the local temperatures at 1st, 100th, 200th, 300th, 400th, and 450th turns, were initially uniform at 7 K. They rose to 18, 24, 26, 30, 39, and 40 K, respectively, at the time when the Thermal Eraser activation is terminated. Figure 5.11 shows the measured coil center fields (B_z). B_z is 317.9 mT before activation of the Thermal Eraser and 318.5 mT after. To confirm that this field increment is not originated from the temperature-dependent measurement error of the Hall sensor, B_z was continuously measured until the temperature of the test coil returned back to its initial value of 7 K. Finally, B_z settled to 318.5 mT. The magnetic field increment by the SCF reduction of 0.6 mT was captured. Provided that the calculated SCF at the beginning of activation of the Thermal Eraser is 1 mT, it is concluded that our proposed Thermal Eraser reduces 60% of SCF. Field stability for 10 minutes before activation of Thermal Eraser was 0.09 mT/min in average, while marginal (<0.01 mT/min) after the activation.

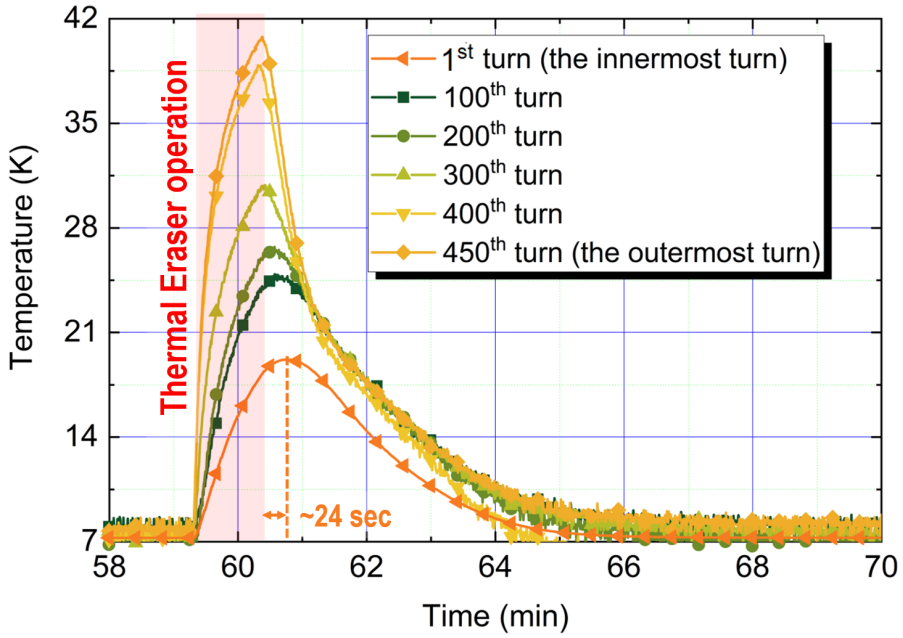

Figure 5.10: Spatially-distributed temperature in the NI HTS test coil.

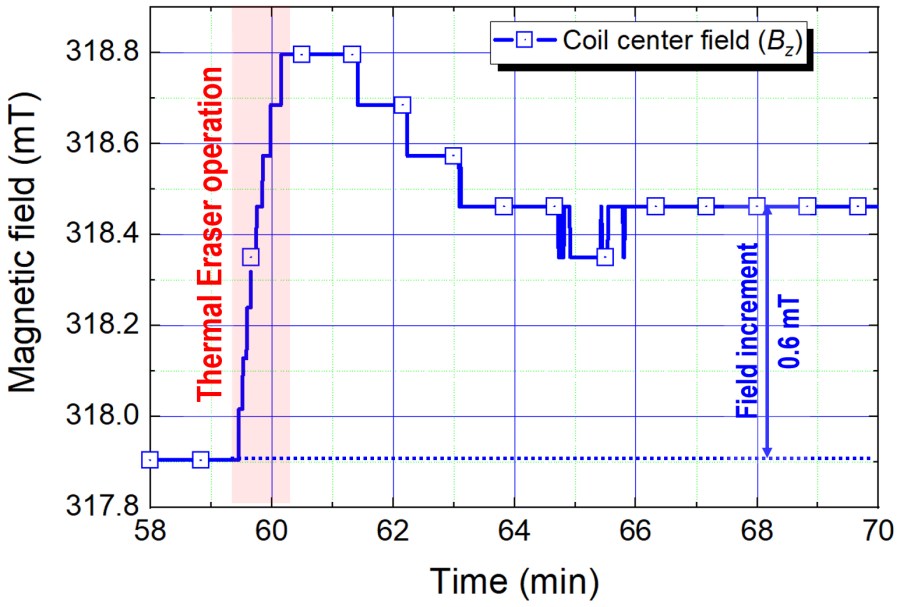

Figure 5.11: Measured magnetic field at the coil center (B_z).

For a post-experiment analysis, FEM simulation with COMSOL Multiphysics using the actual parameters of the test coil and the Thermal Eraser was conducted to describe experimental results. The target of this analysis is to investigate discrepancies between calculation and measurement, and thus to discuss practical considerations in applying the Thermal Eraser to an HTS NMR and MRI magnet.

Figure 5.12 compares the spatial distribution of total current density (i.e., transport and screening): (a) before activation of the Thermal Eraser; and (b) after. The peak values of current density before and after activation of the Thermal Eraser are, respectively, 2200 Amm^{-2} and 700 Amm^{-2}; as expected, the non-uniformity of current distribution in an HTS coil is substantially mitigated by screening current reduction due to the Thermal Eraser activation. The coil center field, $B_{z,cen}$, before the activation is calculated to be 317.8 mT, while it increased to 318.3 mT after the activation. When the screening current is not considered, $B_{z,cen}$ is calculated to be 318.8 mT. The measured SCF reduction of 0.6 mT agrees reasonably well with the calculated one of 0.5 mT. This result may validate our simulation approach as well as the effectiveness of the Thermal Eraser to mitigate the screening current and the consequent SCF.

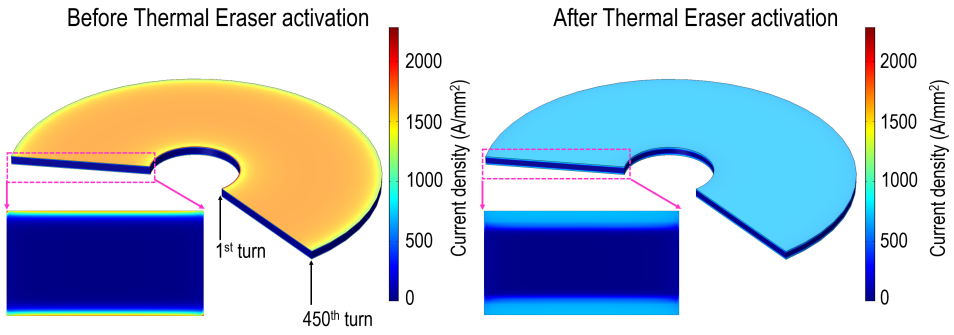

Figure 5.12: Non-uniform current distribution in the given test coil: (a) before activation of the Thermal Eraser; (b) after.

Measured temperature gradient was analyzed in consideration of the actual dimensions and operating conditions: the actual operating temperature of 7 K (10 K assumed in the design); the increment of the inner and outer radii of the Thermal Eraser by 2 mm; and the actual resistance of the Thermal Eraser of 20 Ω (25 Ω assumed in the design). Figure 5.13 shows the temperature profiles of the coil at the termination of Thermal Eraser operation. The red line with squares represents simulated ones with the designed parameters of the Thermal Eraser. The green line with circles represents the experimental results measured immediately after activation of the Thermal Eraser (referring to Figure 5.10). The blue line with triangles shows the simulated temperature profile with the actual parameters of the Thermal Eraser. Note that the marginal difference between the designed and actual parameters of the Thermal Eraser rather largely impacts the performance of the Thermal Eraser. As a result, it can be concluded that the difference between the simulated and measured results is mainly due to: the manufacturing errors of the Thermal Eraser and the different operating conditions from the ideal ones expected in the design stage.

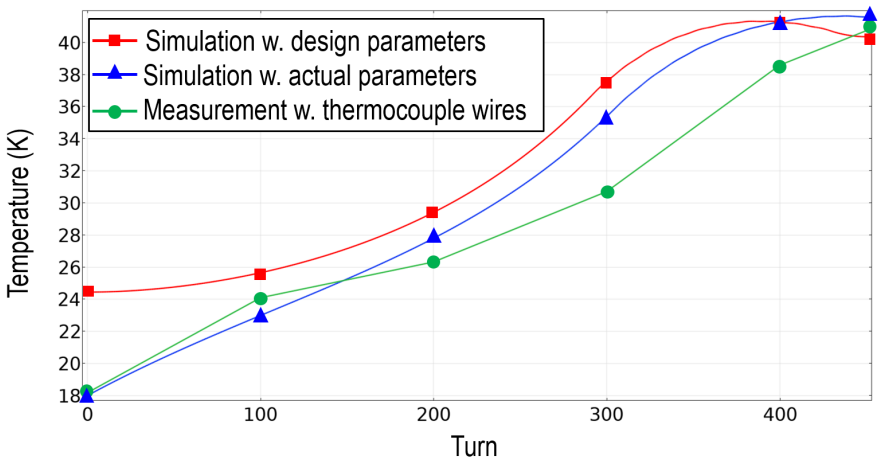

Figure 5.13: Simulation and measurement results of local temperatures in the given HTS test coil.

In conclusion, here I proposed the “Thermal Eraser”, a customized heater that is dedicated to mitigating screening currents in an HTS coil. The key idea of the Thermal Eraser is to create a designated temperature distribution in a way to manipulate local critical currents of individual turns of the HTS coil. For the feasibility demonstration of the Thermal Eraser, a superconducting coil module, including a Thermal Eraser and an HTS coil, was designed and constructed. After the construction and instrumentation of the test coil system, The superconducting coil module was tested at temperatures ranging 7–40 K under a conduction cooling environment. The test coil was energized up to its operating current of 50 A with a constant ramping rate of 0.1 As^{-1}, and then the Thermal Eraser was activated for 1 minute with the operating current of 1 A. By activation of the Thermal Eraser, the temperature distribution in the test coil at selected turns was controlled, and the results were measured. Although there was a small difference between measured and designed temperature distribution, the measurements showed good agreement with the designed ones. The consequent magnetic field increment by the Thermal Eraser activation at the coil center was also measured. The magnetic field at the coil center was 317.9 mT at the beginning of activation of the Thermal Eraser and increased to 318.5 mT eventually. From the result, it was concluded that 0.6 mT increment of the magnetic field was captured, which is due to the reduction of screening current. The measured SCF reduction value agreed reasonably well with the calculated value of 0.5 mT, which is calculated using COMSOL Multiphysics, a commercial finite element method program. Finally, an issue was discussed regarding some practical considerations of the Thermal Eraser by providing comparison results between calculation and measurement results in terms of spatially distributed temperatures. This thesis delivered a viable option for HTS magnets to efficiently mitigate highly non-uniform current densities with Thermal Eraser, a hardware-based optimal temperature control approach. It is believed that it could play a key role in ameliorating detrimental effects caused by screening current in HTS user magnets.

Chapter 6

Conclusion

High temperature superconductor (HTS) magnet is an emerging technology holding immense potential for future high field and large power applications. Among them, nuclear magnetic resonance (NMR) and magnetic resonance imaging (MRI) applications strongly require HTS magnets for higher field intensity and uniformity. Even though high temperature superconductivity was discovered over 30 years ago, the penetration to the NMR and MRI market of this allure HTS magnet has been hindered by the lack of in-depth understanding of nonlinear electromagnetic behaviors mainly due to screening current and the consequent lack of mitigation techniques.

The key difficulty in compiling good knowledge of nonlinear electromagnetic behaviors of an HTS magnet by screening current is based on the limitation of conventional analysis methods. They have suffered from simulating the non-uniform current distribution of HTS, and consequently, endured bitter failure to describe screening current and its consequential effects, such as screening current-induced field (SCF) and screening current-induced stress (SCS).

This thesis aimed to address the challenging issues of conventional analysis methods and HTS magnet technology. A study on screening current was thus performed to simulate screening current and mitigate its detrimental effects on HTS magnets for NMR and MRI applications.

Numerical methods were proposed to simulate screening current and its detrimental effects on HTS magnets: non-uniform current distribution simulation method; current and voltage behavior simulation method; inductance variation simulation method; and mechanical stress simulation method. The validity of the numerical simulation methods was demonstrated with a 9.4 T HTS NMR magnet. The demonstration results are summarized as follows. First, the nonlinear change of inductive voltage was analyzed, which could not be described with the conventional lumped circuit simulation method. The maximum error between calculation and measurement is far less than 2%. Second, measured results of spatial magnetic fields (axial component only) agreed well with calculated ones. The maximum difference between calculation and measurement is 2.0 mT, where the magnitude of the magnetic field at the magnetic field center is 9.4 T. Third, the location change of magnetic field center was simulated. The calculated location change is 30 mm, while the measured one is 28 mm. Fourth, the transient response of magnetic fields was explained in terms of field uniformity and stability. Calculated magnetic field uniformity near the magnetic field center in a 10 mm diameter spherical volume is 107 ppm, while measured one is 123 ppm. Last, the magnet operation stability in terms of mechanical stress was explained. The calculated peak mechanical stress with SCS included is 600 MPa. It suggests the 9.4 T HTS NMR magnet operates well without electrical and mechanical incidents, considering the 95% critical current retention stress of 700 MPa.

A customized electric heater named “Thermal Eraser” was proposed to mitigate detrimental effects on HTS magnets due to screening current. The key philosophy of Thermal Eraser is to intentionally degrade critical currents of individual windings to be uniform by optimal control of temperature gradient in an HTS coil. The optimization technique, a so-called genetic algorithm, was adopted in the design of a Thermal Eraser. Then, a superconducting module, including an HTS test coil and a Thermal Eraser, was constructed, tested, and evaluated. The experimental challenge to demonstrate the feasibility of the Thermal Eraser was the lack of a systematic instrumenta-

tion approach to retrieve the reduction of screening current and measurement of local temperatures. This research overcame the challenge of using cryogenic thermocouple wires and a "precise" data acquisition system with high measurement resolution. As a result, it was confirmed that the Thermal Eraser activation might substantially suppress screening current in a physical way. The key concept to suppress screening current was proposed and implemented by a customized electric heater named Thermal Eraser. Thermal Eraser activation aimed to reduce SCF by 50% at the center (corresponding to 0.5 mT) in a conduction cooling system in the design, while the measured magnetic field increment was 0.6 mT. The Thermal Eraser operation result of spatial temperature distribution agreed well with the designated temperature distribution in the design stage; the maximum temperature difference is 6 K.

A study on screening current to simulate and mitigate detrimental effects on HTS magnets for NMR and MRI applications was conducted. However, the mechanical stress simulation method and Thermal Eraser should be improved since there are some deficiencies in the corresponding studies. Limitations and improvements of the relevant studies are summarized as follows. Stress simulation results were qualitatively compared with the magnet operation results. Therefore, the research should be supplemented with the direct comparison results in terms of measured stress or strain by the use of measurement instruments, e.g., strain gauges or displacement sensors. Although the direct comparison analysis can not have been performed mainly due to the lack of a systematic measurement instrument of mechanical strain and stress in this thesis, future works of directly measuring strain using cryogenic strain gauges will be performed—numerous endeavors of the relevant research have actively been made in recent. Meanwhile, the feasibility of using a Thermal Eraser was demonstrated that the optimal temperature control might be an option to mitigate screening current at the coil level. Additional studies should be performed to extend this research to the magnet level. First, the applicability of an electric heater to intentionally generate extra Joule loss in terms of thermal stability should be discussed at the magnet level, i.e., a stack of

HTS module coils. Second, the practicability of the idea should be examined whether there is remnant space between HTS module coils in an HTS magnet for embedding a heater or not.

In conclusion, this thesis defined the key issues of high-field HTS magnet technology for NMR and MRI magnets. Then, it intended to address the issues by providing solutions in the two aspects: numerical simulation of screening current and nonlinear electromagnetic behaviors of HTS magnet; and a practical technique to mitigate screening current and its detrimental effects on HTS magnet. The solutions were demonstrated with numerical and experimental studies. From the study on numerical simulation methods to describe screening current and its detrimental effects on HTS magnets, a design option considering spatial magnetic field errors and an optimal operation protocol with multiple current sweep reversal applications were discussed. Meanwhile, applicability was discussed in the study on optimal temperature control to mitigate screening current and its detrimental effects. I hope this research will open a new horizon to pave the way for prospective HTS magnet technology for NMR and MRI applications.

Bibliography

[1] E. Moser, E. Laistler, F. Schmitt, and G. Kontaxis, "Ultra-high field NMR and MRI—the role of magnet technology to increase sensitivity and specificity," *Frontiers Phys.*, vol. 5, p. 33, 2017.

[2] D. G. Nishimura, *Principles of magnetic resonance imaging*. Standford Univ., 2010.

[3] J. A. Pople, W. G. Schneider, W. Schneider, H. Bernstein, and H. J. Bernstein, *High-resolution nuclear magnetic resonance*. McGraw-Hill, 1959.

[4] M. D. Sauzade and S. K. Kan, "High resolution nuclear magnetic resonance spectroscopy in high magnetic fields," *Adv. Electronics and Electron Phys.*, vol. 34, pp. 1–93, 1973.

[5] P. Wikus, W. Frantz, R. Kümmerle, and P. Vonlanthen, "Commercial gigahertz-class NMR magnets," *Supercond. Sci. Technol.*, vol. 35, no. 3, p. 033001, 2022.

[6] K. Lord, "New MRI machine in Victoria may help unravel mysteries of stroke," accessed 2014-10-17. [Online]. Available: https://www.abc.net.au/news/2014-10-17/new-mri-machine-to-help-unravel-mysteries-of-stroke/5816738

[7] J. Schwartz *et al.*, "Status of high temperature superconductor based magnets and the conductors they depend upon," *arXiv preprint arXiv:1108.1634*, 2011.

[8] H. Maeda and Y. Yanagisawa, "Future prospects for NMR magnets: A perspective," *J. Magnetic Reson.*, vol. 306, pp. 80–85, 2019.

[9] S. Hahn *et al.*, "45.5-tesla direct-current magnetic field generated with a high-temperature superconducting magnet," *Nature*, vol. 570, no. 7762, pp. 496–499, 2019.

[10] H. W. Weijers *et al.*, "Progress in the development and construction of a 32-T superconducting magnet," *IEEE Trans. Appl. Supercond.*, vol. 26, no. 4, p. 4300807, 2016.

[11] J. Liu *et al.*, "World record 32.35 tesla direct-current magnetic field generated with an all-superconducting magnet," *Supercond. Sci. Technol*, vol. 33, no. 3, p. 03LT01, 2020.

[12] P. Fazilleau, X. Chaud, F. Debray, T. Lécrevisse, and J.-B. Song, "38 mm diameter cold bore metal-as-insulation HTS insert reached 32.5 T in a background magnetic field generated by resistive magnet," *Cryogenics*, vol. 106, p. 103053, 2020.

[13] B. Sorbom *et al.*, "Arc: A compact, high-field, fusion nuclear science facility and demonstration power plant with demountable magnets," *Fusion Eng. Des.*, vol. 100, pp. 378 – 405, 2015.

[14] A. Sykes *et al.*, "Compact fusion energy based on the spherical tokamak," *Nucl. Fusion*, vol. 58, no. 1, p. 016039, 2017.

[15] P. Bruzzone *et al.*, "High temperature superconductors for fusion magnets," *Nucl. Fusion*, vol. 58, no. 10, p. 103001, 2018.

[16] L. Rossi *et al.*, "The EuCARD-2 future magnets European collaboration for accelerator-quality HTS magnets," *IEEE Trans. Appl. Supercond.*, vol. 25, no. 3, p. 4001007, 2014.

[17] H. Piekarz, S. Hays, J. Blowers, B. Claypool, and V. Shiltsev, "Record fast-cycling accelerator magnet based on HTS conductor," *Nucl. Inst. Methods Phys. Res.*, vol. 943, p. 162490, 2019.

[18] J. Kim *et al.*, "Design, construction, and operation of an 18 T 70 mm no-insulation (RE) Ba2Cu3O7- x magnet for an axion haloscope experiment," *Rev. Sci. Instrum.*, vol. 91, no. 2, p. 023314, 2020.

[19] L. Rossi and C. Senatore, "HTS Accelerator Magnet and Conductor Development in Europe," *Instruments*, vol. 5, no. 1, p. 8, 2021.

[20] J. Liu, Y. Dai, and L. Li, "Progress in the development of a 25 T all superconducting NMR magnet," *Cryogenics*, vol. 79, pp. 79–84, 2016.

[21] R. Piao *et al.*, "High resolution NMR measurements using a 400 MHz NMR with an (RE) $Ba_2Cu_3O_{7-x}$ high-temperature superconducting inner coil: Towards a compact super-high-field NMR," *J. Magnetic Reson.*, vol. 263, pp. 164–171, 2016.

[22] Y. Li, L. Wang, and Q. Wang, "Electromagnetic Design of HTS Insert for Ultrahigh Field NMR Magnet," *IEEE Trans. Appl. Supercond.*, vol. 28, no. 3, pp. 1–5, 2017.

[23] X. Yuan, Y. Wang, Y. Hou, C. Kan, C. Cai, and M. Sun, "Conceptual Design of a Bitter-Like Superconducting Magnet Stacked by REBCO Annular Plates and Magnetized by Flux Pump," *IEEE Trans. Appl. Supercond.*, vol. 28, no. 3, p. 4603005, 2018.

[24] Y. Wang, Q. Wang, J. Liu, J. Cheng, and F. Liu, "Insert magnet and shim coils design for a 27 T nuclear magnetic resonance spectrometer with hybrid high and low temperature superconductors," *Supercond. Sci. Technol.*, vol. 33, no. 6, p. 064004, may 2020.

[25] B. Parkinson, "Design considerations and experimental results for MRI systems using HTS magnets," *Supercond. Sci. Technol*, vol. 30, no. 1, p. 014009, 2016.

[26] T. Tosaka *et al.*, "R&D project on HTS magnets for ultrahigh-field MRI systems," *IEEE Trans. Appl. Supercond.*, vol. 26, no. 4, p. 4402505, 2016.

[27] B. Parkinson, K. Bouloukakis, and R. Slade, "A compact 3 T all HTS cryogen-free MRI system," *Supercond. Sci. Technol*, vol. 30, no. 12, p. 125009, 2017.

[28] M. Oya *et al.*, "Design and manufacture of half-size 3-T high-temperature superconducting magnet for MRI," *IEEE Trans. Appl. Supercond.*, vol. 28, no. 3, p. 4401205, 2018.

[29] X. Wang *et al.*, "Electromagnetic design of 1.5 T no-insulation REBCO coil system charged by multiflux pumps for dedicated MRI," *IEEE Trans. Appl. Supercond.*, vol. 29, no. 5, p. 4601805, 2019.

[30] B. Shen *et al.*, "Development of an HTS Magnet for Ultra-Compact MRI System: Optimization Using Genetic Algorithm (GA) Method," *IEEE Trans. Appl. Supercond.*, vol. 30, no. 4, p. 4601805, 2020.

[31] Z. Li, N. Maki, T. Ida, M. Miki, and M. Izumi, "Comparative Study of 1-MW PM and HTS Synchronous Generators for Marine Current Turbine," *IEEE Trans. Appl. Supercond.*, vol. 28, no. 4, p. 5206605, 2018.

[32] H. Jing, N. Maki, T. Ida, and M. Izumi, "Electromechanical Design of an MW Class Wave Energy Converter With an HTS Tubular Linear Generator," *IEEE Trans. Appl. Supercond.*, vol. 28, no. 4, p. 4902504, June 2018.

[33] O. Rahman, K. M. Muttaqi, and D. Sutanto, "High temperature superconducting devices and renewable energy resources in future power grids: A case study," *IEEE Trans. Appl. Supercond.*, vol. 29, no. 2, p. 3800404, 2019.

[34] M. Ardestani, N. Arish, and H. Yaghobi, "A new HTS dual stator linear permanent magnet Vernier machine with Halbach array for wave energy conversion," *Phys. C: Supercond. Appl.*, vol. 569, p. 1353593, 2020.

[35] F. Dong, Z. Huang, D. Qiu, L. Hao, W. Wu, and Z. Jin, "Design and analysis of a small-scale linear propulsion system for maglev applications (1)—the overall design process," *IEEE Trans. Appl. Supercond.*, vol. 29, no. 2, p. 5201005, 2019.

[36] U. Bong *et al.*, "A Design Study on 40 MW Synchronous Motor With No-Insulation HTS Field Winding," *IEEE Trans. Appl. Supercond.*, vol. 29, no. 5, p. 5203706, 2019.

[37] F. Dong, Z. Huang, D. Qiu, L. Hao, W. Wu, and Z. Jin, "Design and analysis of a small-scale linear propulsion system for maglev applications (2)–the HTS no-insulation magnets," *IEEE Trans. Appl. Supercond.*, vol. 29, no. 2, p. 5201005, 2019.

[38] Y. Du *et al.*, "Feasibility Study of a DC Linear Motor Based on the Magnet Track of High-Temperature Superconducting Maglev," *IEEE Trans. Appl. Supercond.*, vol. 30, no. 3, p. 3600605, 2020.

[39] J. Zheng, S. S. Peng, W. Y. Li, and Y. J. Dai, "Magnet design of 10MJ multiple solenoids SMES," *IOP Conference Series: Earth and Environmental Science*, vol. 233, p. 032026, Feb. 2019.

[40] J. Liu, L. Wang, Y. Wang, Q. Wang, and Y. Dai, "Design of a 30-T Superconducting Magnet for Quantum Oscillation Application," *IEEE Trans. Appl. Supercond.*, vol. 29, no. 5, p. 4301205, 2019.

[41] J. Choi *et al.*, "Commercial Design and Operating Characteristics of a 300 kW Superconducting Induction Heater (SIH) Based on HTS Magnets," *IEEE Trans. Appl. Supercond.*, vol. 29, no. 5, p. 3700105, 2019.

[42] L. Guo *et al.*, "Manufacture and Performance Test of 3.5 T High Temperature Superconducting Coils for the Magnetic Separation," *IEEE Trans. Appl. Supercond.*, vol. 30, no. 4, p. 3700605, 2020.

[43] H. Bai *et al.*, "The 40 T Superconducting Magnet Project at the National High Magnetic Field Laboratory," *IEEE Trans. Appl. Supercond.*, vol. 30, no. 4, p. 4300405, 2020.

[44] S. Hahn, J. Bascuñán, W.-S. Kim, E. S. Bobrov, H. Lee, and Y. Iwasa, "Field mapping, NMR lineshape, and screening currents induced field analyses for homogeneity improvement in LTS/HTS NMR magnets," *IEEE Trans. Appl. Supercond.*, vol. 18, no. 2, pp. 856–859, 2008.

[45] M. C. Ahn, T. Yagai, S. Hahn, R. Ando, J. Bascunan, and Y. Iwasa, "Spatial and temporal variations of a screening current induced magnetic field in a double-pancake HTS insert of an LTS/HTS NMR magnet," *IEEE Trans. Appl. Supercond.*, vol. 19, no. 3, pp. 2269–2272, 2009.

[46] S. Takahashi *et al.*, "Hoop stress modification, stress hysteresis and degradation of a REBCO coil due to the screening current under external magnetic field cycling," *IEEE Trans. Appl. Supercond.*, vol. 30, no. 4, pp. 1–7, 2020.

[47] Y. Li *et al.*, "Screening-current-induced strain gradient on REBCO conductor: an experimental and analytical study with small coils wound with monofilament and striated multifilament REBCO tapes," *IEEE Trans. Appl. Supercond.*, vol. 30, no. 4, pp. 1–5, 2020.

[48] R. Brambilla, F. Grilli, L. Martini, and F. Sirois, "Integral equations for the current density in thin conductors and their solution by the finite-element method," *Supercond. Sci. Technol.*, vol. 21, no. 10, p. 105008, 2008.

[49] R. Brambilla, F. Grilli, D. N. Nguyen, L. Martini, and F. Sirois, "AC losses in thin superconductors: the integral equation method applied to stacks and windings," *Supercond. Sci. Technol.*, vol. 22, no. 7, p. 075018, 2009.

[50] R. Brambilla, F. Grilli, and L. Martini, "Integral equations for computing AC losses of radially and polygonally arranged HTS thin tapes," *IEEE Trans. Appl. Supercond.*, vol. 22, no. 4, pp. 8 401 006–8 401 006, 2012.

[51] V. M. Zermeño and F. Grilli, "3D modeling and simulation of 2G HTS stacks and coils," *Supercond. Sci. Technol.*, vol. 27, no. 4, p. 044025, 2014.

[52] V. M. Zermeno, F. Grilli, and F. Sirois, "A full 3D time-dependent electromagnetic model for Roebel cables," *Supercond. Sci. Technol.*, vol. 26, no. 5, p. 052001, 2013.

[53] R. Brambilla, F. Grilli, L. Martini, M. Bocchi, and G. Angeli, "A finite-element method framework for modeling rotating machines with superconducting windings," *IEEE Trans. Appl. Supercond.*, vol. 28, no. 5, pp. 1–11, 2018.

[54] F. Liang *et al.*, "A finite element model for simulating second generation high temperature superconducting coils/stacks with large number of turns," *J. Appl. Phys.*, vol. 122, no. 4, p. 043903, 2017.

[55] E. Berrospe-Juarez, V. M. Zermeño, F. Trillaud, and F. Grilli, "Real-time simulation of large-scale HTS systems: Multi-scale and homogeneous models using the T–A formulation," *Supercond. Sci. Technol.*, vol. 32, no. 6, p. 065003, 2019.

[56] K. Zhang, S. Hellmann, M. Calvi, and T. Schmidt, "Magnetization simulation of ReBCO tape stack with a large number of layers using the ANSYS A-V-A formulation," *IEEE Trans. Appl. Supercond.*, vol. 30, no. 4, pp. 1–5, 2020.

[57] A. Arsenault, F. Sirois, and F. Grilli, "Implementation of the H-formulation in COMSOL Multiphysics for simulating the magnetization of bulk superconduc-

tors and comparison with the H-formulation," *IEEE Trans. Appl. Supercond.*, vol. 31, no. 2, pp. 1–11, 2020.

[58] L. Bortot *et al.*, "A coupled A–H formulation for magneto-thermal transients in high-temperature superconducting magnets," *IEEE Trans. Appl. Supercond.*, vol. 30, no. 5, pp. 1–11, 2020.

[59] S. Mykola and G. Fedor, "A–V formulation for numerical modelling of superconductor magnetization in true 3D geometry," *Supercond. Sci. Technol.*, vol. 32, no. 11, p. 115001, 2019.

[60] A. Arsenault, F. Sirois, and F. Grilli, "Efficient Modeling of High-Temperature Superconductors Surrounded by Magnetic Components Using a Reduced H–Formulation," *IEEE Trans. Appl. Supercond.*, vol. 31, no. 4, pp. 1–9, 2021.

[61] V. M. Rodriguez-Zermeno *et al.*, "Towards faster FEM simulation of thin film superconductors: a multiscale approach," *IEEE Trans. Appl. Supercond.*, vol. 21, no. 3, pp. 3273–3276, 2010.

[62] V. M. Zermeno, A. B. Abrahamsen, N. Mijatovic, B. B. Jensen, and M. P. Sørensen, "Calculation of alternating current losses in stacks and coils made of second generation high temperature superconducting tapes for large scale applications," *J. Appl. Phys.*, vol. 114, no. 17, p. 173901, 2013.

[63] Z. Hong, A. Campbell, and T. Coombs, "Numerical solution of critical state in superconductivity by finite element software," *Supercond. Sci. Technol.*, vol. 19, no. 12, p. 1246, 2006.

[64] R. Brambilla, F. Grilli, and L. Martini, "Development of an edge-element model for AC loss computation of high-temperature superconductors," *Supercond. Sci. Technol.*, vol. 20, no. 1, p. 16, 2006.

[65] Y. Yanagisawa *et al.*, "Effect of YBCO-coil shape on the screening current-induced magnetic field intensity," *IEEE Trans. Appl. Supercond.*, vol. 20, no. 3, pp. 744–747, 2010.

[66] Y. Koyama *et al.*, "Towards beyond 1 GHz NMR: Mechanism of the long-term drift of screening current-induced magnetic field in a Bi-2223 coil," *Physica C: Superconductivity*, vol. 469, no. 13, pp. 694–701, 2009.

[67] D. Yang, K. Kim, Y. Choi, O. Kwon, Y. Park, and H. Lee, "Screening current-induced field in non-insulated GdBCO pancake coil," *Supercond. Sci. Technol.*, vol. 26, no. 10, p. 105025, 2013.

[68] G. Dilasser, P. Fazilleau, and P. Tixador, "Experimental measurement and numerical simulation of the screening current-induced field decay in a small ReBCO coil," *IEEE Trans. Appl. Supercond.*, vol. 27, no. 4, pp. 1–4, 2016.

[69] Y. Yanagisawa *et al.*, "Magnitude of the screening field for YBCO coils," *IEEE Trans. Appl. Supercond.*, vol. 21, no. 3, pp. 1640–1643, 2010.

[70] L. Wang, Q. Wang, J. Liu, H. Wang, X. Hu, and P. Chen, "Screening current-induced magnetic field in a noninsulated GdBCO HTS coil for a 24 T all-superconducting magnet," *IEEE Trans. Appl. Supercond.*, vol. 27, no. 4, pp. 1–6, 2016.

[71] H. Ueda *et al.*, "Numerical simulation on magnetic field generated by screening current in 10-T-class REBCO coil," *IEEE Trans. Appl. Supercond.*, vol. 26, no. 4, pp. 1–5, 2016.

[72] H. Ueda, Y. Awazu, K. Tokunaga, and S. Kim, "Numerical evaluation of the deformation of REBCO pancake coil, considering winding tension, thermal stress, and screening-current-induced stress," *Supercond. Sci. Technol.*, vol. 34, no. 2, p. 024003, 2021.

[73] H. Ueda, H. Maeda, Y. Suetomi, and Y. Yanagisawa, "Experiment and numerical simulation of the combined effect of winding, cool-down, and screening current induced stresses in REBCO coils," *Supercond. Sci. Technol.*, vol. 35, no. 5, p. 054001, 2022.

[74] Y. Yan, Y. Li, and T. Qu, "Screening current induced magnetic field and stress in ultra-high-field magnets using REBCO coated conductors," *Supercond. Sci. Technol.*, vol. 35, no. 1, p. 014003, 2021.

[75] Y. Yan, C. Xin, M. Guan, H. Liu, Y. Tan, and T. Qu, "Screening current effect on the stress and strain distribution in REBCO high-field magnets: experimental verification and numerical analysis," *Supercond. Sci. Technol.*, vol. 33, no. 5, p. 05LT02, 2020.

[76] H. Miyazaki *et al.*, "Screening-current-induced magnetic field of conduction-cooled HTS magnets wound with REBCO-coated conductors," *IEEE Trans. Appl. Supercond.*, vol. 27, no. 4, pp. 1–5, 2017.

[77] D. J. Kolb-Bond *et al.*, "Computing strains due to screening currents in REBCO magnets," *IEEE Trans. Appl. Supercond.*, vol. 30, no. 4, pp. 1–5, 2020.

[78] D. Kolb-Bond *et al.*, "Screening current rotation effects: SCIF and strain in REBCO magnets," *Supercond. Sci. Technol.*, vol. 34, no. 9, p. 095004, 2021.

[79] Y. Yanagisawa *et al.*, "Effect of coil current sweep cycle and temperature change cycle on the screening current-induced magnetic field for Ybco-coated conductor coils," *Adv. Cryogenic Eng.*, vol. 57, pp. 1372–1380, 2011.

[80] Y. Yanagisawa, Y. Xu, X. Jin, H. Nakagome, and H. Maeda, "Reduction of screening current-induced magnetic field of REBCO coils by the use of multi-filamentary tapes," *IEEE Trans. Appl. Supercond.*, vol. 25, no. 3, pp. 1–5, 2014.

[81] K. Kim *et al.*, "Study on elimination of screening-current-induced field in pancake-type non-insulated HTS coil," *Supercond. Sci. Technol.*, vol. 29, no. 3, p. 035009, 2016.

[82] Y.-G. Kim *et al.*, "Study for reducing the screening current-induced field in a 10-MHz no-insulation magnet using current sweep reversal method," *IEEE Trans. Appl. Supercond.*, vol. 25, no. 3, pp. 1–5, 2014.

[83] Y. J. Hwang *et al.*, "A study on mitigation of screening current induced field with a 3-T 100-mm conduction-cooled metallic cladding REBCO magnet," *IEEE Trans. Appl. Supercond.*, vol. 27, no. 4, pp. 1–5, 2016.

[84] A. R. Innes and E. Rhoderick, *Introduction to superconductivity*. Pergamon Press, 1980.

[85] C. Kittel, *Introduction to solid state physics*. Wiley, 2021.

[86] M. Tinkham, *Introduction to superconductivity*. Courier Corporation, 2004.

[87] F. London and H. London, "The electromagnetic equations of the supraconductor," *Proc. R. Soc. A: Math. Phys. Eng. Sci.*, vol. 149, no. 866, pp. 71–88, 1935.

[88] C. J. Gorter and H. Casimir, "On supraconductivity I," *Physica*, vol. 1, no. 1-6, pp. 306–320, 1934.

[89] H. Fröhlich, "Theory of the superconducting state. I. The ground state at the absolute zero of temperature," *Phys. Rev.*, vol. 79, no. 5, p. 845, 1950.

[90] J. Bardeen, L. N. Cooper, and J. R. Schrieffer, "Microscopic theory of superconductivity," *Phys. Rev.*, vol. 106, no. 1, p. 162, 1957.

[91] B. Mühlschlegel, "Die thermodynamischen funktionen des supraleiters," *Zeitschrift für Physik*, vol. 155, no. 3, pp. 313–327, 1959.

[92] A. B. Pippard, *Elements of classical thermodynamics: for advanced students of physics*. Cambridge University Press, 1964.

[93] L. P. Gor'kov, "Microscopic derivation of the Ginzburg-Landau equations in the theory of superconductivity," *Sov. Phys. JETP*, vol. 9, no. 6, pp. 1364–1367, 1959.

[94] A. Pippard, "The coherence concept in superconductivity," *Physica*, vol. 19, no. 1-12, pp. 765–774, 1953.

[95] A. Gauzzi, B. J. Jönsson-Åkerman, A. Clerc-Dubois, and D. Pavuna, "Scaling between superconducting critical temperature and structural coherence length in YBa2Cu3O6. 9 films," *EPL*, vol. 51, no. 6, p. 667, 2000.

[96] T. Pereg-Barnea *et al.*, "Absolute values of the London penetration depth in YBa 2 Cu 3 O 6+ y measured by zero field ESR spectroscopy on Gd doped single crystals," *Phys. Rev. B*, vol. 69, no. 18, p. 184513, 2004.

[97] G. Grissonnanche *et al.*, "Direct measurement of the upper critical field in cuprate superconductors," *Nat. Comm.*, vol. 5, no. 1, pp. 1–8, 2014.

[98] J. G. Bednorz and K. A. Müller, "Possible highT c superconductivity in the Ba-La- Cu- O system," *Z. Phys. B*, vol. 64, no. 2, pp. 189–193, 1986.

[99] I. Božović, A. Bollinger, J. Wu, and X. He, "Can high-Tc superconductivity in cuprates be explained by the conventional BCS theory?" *Low Temp. Phys.*, vol. 44, no. 6, pp. 519–527, 2018.

[100] S. J. Chapman, Q. Du, and M. D. Gunzburger, "On the Lawrence–Doniach and anisotropic Ginzburg–Landau models for layered superconductors," *SIAM J. Appl. Math.*, vol. 55, no. 1, pp. 156–174, 1995.

[101] L. Civale *et al.*, "Vortex confinement by columnar defects in $YBa_2Cu_3O_7$ crystals: Enhanced pinning at high fields and temperatures," *Phys. Rev. Lett.*, vol. 67, no. 5, p. 648, 1991.

[102] W. Kwok, U. Welp, V. Vinokur, S. Fleshler, J. Downey, and G. Crabtree, "Direct observation of intrinsic pinning by layered structure in single-crystal $YBa_2Cu_3O_{7-\delta}$," *Phys. Rev. Lett.*, vol. 67, no. 3, p. 390, 1991.

[103] D. X. Fischer, R. Prokopec, J. Emhofer, and M. Eisterer, "The effect of fast neutron irradiation on the superconducting properties of REBCO coated conductors with and without artificial pinning centers," *Supercond. Sci. Technol.*, vol. 31, no. 4, p. 044006, 2018.

[104] K. Tsuchiya *et al.*, "Superconducting properties of commercial REBCO-coated conductors with artificial pinning centers," *Supercond. Sci. Technol.*, vol. 34, no. 10, p. 105005, 2021.

[105] D. S. Fisher, M. P. Fisher, and D. A. Huse, "Thermal fluctuations, quenched disorder, phase transitions, and transport in type-II superconductors," *Phys. Rev. B*, vol. 43, no. 1, p. 130, 1991.

[106] C. Senatore, C. Barth, M. Bonura, M. Kulich, and G. Mondonico, "Field and temperature scaling of the critical current density in commercial REBCO coated conductors," *Supercond. Sci. Technol.*, vol. 29, no. 1, p. 014002, 2015.

[107] D. A. Huse, M. Fisher, and D. S. Fisher, "Are superconductors really superconducting?" *Nature*, vol. 358, no. 6387, pp. 553–559, 1992.

[108] Y. Iwasa, *Case studies in superconducting magnets: design and operational issues*. Springer Science & Business Media, 2009.

[109] R. Brambilla, F. Grilli, and L. Martini, "Development of an edge-element model for AC loss computation of high-temperature superconductors," *Supercond. Sci. Technol.*, vol. 20, no. 1, pp. 16–24, 2007.

[110] S. Stavrev *et al.*, "Comparison of numerical methods for modeling of superconductors," *IEEE Trans. Magn.*, vol. 38, no. 2, pp. 849–852, 2002.

[111] V. M. R. Zermeno, A. B. Abrahamsen, N. Mijatovic, B. B. Jensen, and M. P. Soerensen, "Calculation of AC losses in stacks and coils made of second generation high temperature superconducting tapes for large scale applications," *J. Appl. Phys.*, vol. 114, no. 17, p. 173901, 2013.

[112] T. Wang *et al.*, "Analyses of transient behaviors of no-insulation REBCO pancake coils during sudden discharging and overcurrent," *IEEE Trans. Appl. Supercond.*, vol. 25, no. 3, pp. 1–9, 2015.

[113] G. Kim *et al.*, "A numerical method for spatially-distributed transient simulation to replicate nonlinear 'defect-irrelevant'behaviors of no-insulation HTS coil," *Supercond. Sci. Technol.*, vol. 34, no. 11, p. 115004, 2021.

[114] ——, "Fast Current Distribution Simulation Method for No-insulation HTS Coil with Defects," *IEEE Trans. Appl. Supercond.*, 2022.

[115] E. B. Rosa and F. W. Grover, *Formulas and tables for the calculation of mutual and self-inductance*. US Government Printing Office, 1948, no. 169.

[116] M. W. Garrett, "Calculation of fields, forces, and mutual inductances of current systems by elliptic integrals," *J. Appl. Phys.*, vol. 34, no. 9, pp. 2567–2573, 1963.

[117] C. Hoer and Y. Love, "Exact inductance equations for rectangular conductors with applications to more complicated geometries," *J. Res. Nat. Bureau Standards-C. Eng. Instrum*, vol. 69, no. 2, pp. 127–137, 1965.

[118] M. Gyimesi and D. Ostergaard, "Inductance computation by incremental finite element analysis," *IEEE Trans. Magn.*, vol. 35, no. 3, pp. 1119–1122, 1999.

[119] M. W. Garrett, "Thick cylindrical coil systems for strong magnetic fields with field or gradient homogeneities of the 6th to 20th order," *J. Appl. Phys.*, vol. 38, no. 6, pp. 2563–2586, 1967.

[120] J. Bascuñán, W. Kim, S. Hahn, E. S. Bobrov, H. Lee, and Y. Iwasa, "An LTS/HTS NMR magnet operated in the range 600–700 MHz," *IEEE Trans. Appl. Supercond.*, vol. 17, no. 2, pp. 1446–1449, 2007.

[121] J. Bascuñán, S. Hahn, Y. Kim, J. Song, and Y. Iwasa, "90-mm/18.8-T all-HTS insert magnet for 1.3 GHz LTS/HTS NMR application: Magnet design and double-pancake coil fabrication," *IEEE Trans. Appl. Supercond.*, vol. 24, no. 3, p. 4300904, 2013.

[122] Y. Iwasa *et al.*, "A high-resolution 1.3-GHz/54-mm LTS/HTS NMR magnet," *IEEE Trans. Appl. Supercond.*, vol. 25, no. 3, p. 4301205, 2014.

[123] H. Kitaguchi *et al.*, "Development of a Bi-2223 HTS magnet for 3T MRI system for human brains," *IEEE Trans. Appl. Supercond.*, vol. 20, no. 3, pp. 710–713, 2010.

[124] B. J. Parkinson, R. Slade, M. J. Mallett, and V. Chamritski, "Development of a cryogen free 1.5 T YBCO HTS magnet for MRI," *IEEE Trans. Appl. Supercond.*, vol. 23, no. 3, pp. 4 400 405–4 400 405, 2012.

[125] T. Baig, Z. Yao, D. Doll, M. Tomsic, and M. Martens, "Conduction cooled magnet design for 1.5 T, 3.0 T and 7.0 T MRI systems," *Supercond. Sci. Technol.*, vol. 27, no. 12, p. 125012, 2014.

[126] K. L. Kim, S. Yoon, K. Cheon, J. Kim, H. Lee, S. Lee, D. L. Kim, and S. Hahn, "400-MHz/60-mm all-REBCO nuclear magnetic resonance magnet: Magnet design," *IEEE Trans. Appl. Supercond.*, vol. 26, no. 4, p. 4302604, 2015.

[127] H. Miyazaki *et al.*, "Design of a conduction-cooled 9.4 T REBCO magnet for whole-body MRI systems," *Supercond. Sci. Technol.*, vol. 29, no. 10, p. 104001, 2016.

[128] C. Barth, G. Mondonico, and C. Senatore, "Electro-mechanical properties of REBCO coated conductors from various industrial manufacturers at 77 K, self-field and 4.2 K, 19 T," *Supercond. Sci. Technol.*, vol. 28, no. 4, p. 045011, 2015.

[129] S. Hahn *et al.*, "No-insulation multi-width winding technique for high temperature superconducting magnet," *Appl. Phys. Lett.*, vol. 103, no. 17, p. 173511, 2013.

[130] S. G. Lee *et al.*, "Development Progress of Metal-Clad No-Isulation All-REBCO Magnet for 400 MHz High Resolution NMR." Andong, Korea: MEM18, 2018.

[131] J. Y. Jang *et al.*, "Reproducibility of the field homogeneity of a metal-clad no-insulation all-REBCO magnet with a multi-layer ferromagnetic shim," *Supercond. Sci. Technol.*, vol. 33, no. 2, p. 025005, 2020.

[132] ——, "Design, construction and 13 K conduction-cooled operation of a 3 T 100 mm stainless steel cladding all-REBCO magnet," *Supercond. Sci. Technol.*, vol. 30, no. 10, p. 105012, 2017.

[133] A. S. Conference, "CONTINUUM," accessed 2018-11-05. [Online]. Available: https://appliedsuperconductivity.org/asc2018/wp-content/uploads/2018/11/ASC18ContinuumMagazine.pdf

[134] J. Lu *et al.*, "Field angular dependence of hysteresis losses of coated conductor for high field magnets," *IEEE Trans. Appl. Supercond.*, vol. 23, no. 3, p. 8200804, 2013.

[135] D. K. Hilton, A. V. Gavrilin, and U. P. Trociewitz, "Practical fit functions for transport critical current versus field magnitude and angle data from (RE)BCO coated conductors at fixed low temperatures and in high magnetic fields," *Supercond. Sci. Technol.*, vol. 28, no. 7, 2015.

[136] J. Rhyner, "Magnetic properties and AC-losses of superconductors with power-law current-voltage characteristics," *Phys. C: Supercond. Appl.*, vol. 212, pp. 292–300, 1993.

[137] S. Wimbush and N. Strickland, "Critical current characterisation of SuNAM SAN04200 2G HTS superconducting wire," accessed 2017-07-07. [Online]. Available: https://doi.org/10.6084/m9.figshare.5182354.v1

[138] S. Hahn, D. K. Park, J. Bascuñán, and Y. Iwasa, "HTS pancake coils without turn-to-turn insulation," *IEEE Trans. Appl. Supercond.*, vol. 21, no. 3, pp. 1592–1595, 2010.

초 록

초전도 자석은 다량의 전류가 흐를 수 있는 한편 발열 손실이 거의 발생하지 않는다는 매력적인 특성을 바탕으로 강한 자석에 대한 엄청난 가능성을 가지고 있다. 그들은 실제로 고성능 및 대용량 응용기기를 위한 전자석에 대하여 혁신적인 기술을 가능하게 했다. 그 중에서도 초전도 자석은 상전도 자석 보다 높은 자기장 강도와 균일성을 제공함으로써 핵자기공명 및 자기공명영상 응용기기에 핵심적인 역할을 수행해 왔다.

지난 몇 년 동안, 저온 초전도 자석은 핵자기공명 및 자기공명 응용기기를 개발하는 데 있어 실로 핵심적인 역할을 했다. 그러나 핵자기공명 및 자기공명영상용 저온 초전도 자석의 최대 자기장 강도의 실질적인 한계에 도달했다. 따라서 고온 초전도 자석은 자기공명 응용기기, 즉 핵자기공명 및 자기공명영상 응용기기에서 저온 초전도 자석의 핵심 역할을 대체하기 위해 긍정적으로 검토되고 있으며 그 이유는 고온 초전도 선재는 저온 초전도 선재 대비 높은 자기장 환경에서 보다 우수한 전류 통전 용량을 가지고 있는 것으로 확인되었기 때문이다.

핵자기공명 및 자기공명영상 응용기기용 고온 초전도 자석을 개발하는 데 있어 중요한 과제는 차폐 전류 및 그 결과적 영향, 즉 차폐 전류 유도 자기장과 차폐 전류 유도 응력이다. 이와 관련하여, 차폐 전류로 인한 고 자기장 고온 초전도 자석의 전자기 및 기계적 고장에 대한 여러 연구가 보고되었다. 차폐 전류 유도 자기장은 공간 자기장 균일성 및 시간 자기장 안정성 측면에서 고온 초전도 자석의 자기 성능을 저하시킨다. 차폐 전류 유도 응력은 자석 작동에서 기계적 안정성을 저하시킨다. 이에 따라 고온 초전도 자석 분야에서는 수치 해석을 통한 차폐 전류의 심층적인 이해와 차폐 전류 및 그에 따른 영향을 완화하기 위한 실용적 기술이 시급한 상황이다.

본 논문에서는 자기공명 응용기기를 위한 고온 초전도 자석의 차폐 전류 문제를 다루는 것을 목표로 한다. 차폐 전류 특성을 모사 할 수 있는 수치 해석 방법이 부족하고 차폐 전류를 실질적으로 완화할 수 있는 실용적 기법이 부족한 것을 현재의 고온 초전도 자석 기술의 문제로 정의한다. 그런 다음 수치 해석과 실질적 기술의 두 가지 측면에서 두 가지 해결책이 제공된다. 각 해결책은 실험 연구를 통해 입증된다. 두가지 해결책에 대한 자세한 설명은 다음과 같다.

첫째, 차폐 전류와 그에 따른 영향을 모사하기 위해 수치 해석 방법을 연구한다. 차폐 전류 유도 효과를 설명하기 위해 여러 해석 방법이 개발된다. 예를 들어, 불균일한 전류 밀도, 고온 초전도 코일의 비선형 유도 전압, 공간 및 시간 자기장 거동 및 과도한 기계적 스트레스에 대한 해석 방법이 개발된다. 그런 다음 고온 초전도 핵자기공명 자석에 대한 분석 연구를 수행하여 차폐 전류와 그 영향을 설명함에 있어 제안된 수치 해석 방법의 유효성을 입증한다. 핵자기공명 응용기기을 위한 3 T 및 9.4 T 전 고온 초전도 자석이 분석 연구에 채택된다. 수치 해석의 계산 결과는 전압, 공간 자기장, 공간 자기장 균일성, 시간 자기장 안정성 및 자석 작동의 기계적 안정성 측면에서 측정된 결과와 비교된다. 그 결과 계산과 측정 결과 사이에 양호한 일치성이 확인되었다. 결론적으로, 비교 결과는 제안된 수치 해석 방법의 사용이 고온 초전도 자석의 차폐 전류에 의해 유도되는 비선형 전자기 거동을 설명하는 데 유효함을 시사한다.

둘째, 고온 초전도 코일의 차폐 전류를 완화하기 위한 실용적인 솔루션으로 최적 설계된 맞춤형 전기 히터를 제안한다. 해당 기술의 핵심 개념은 고온 초전도 코일의 온도 구배를 최적화하는 것이다. 완화 메커니즘은 선별전류의 특성에 따라 임계전류의 크기에 따라 달라지게 되는데 열지우개는 최적의 온도제어로 고온 초전도 코일 내 개별 권선의 임계전류의 크기를 의도적으로 낮추는 것을 목표로 한다. 고온 초전도 코일과 최적 설계된 전기 히터를 포함하는 초전도 모듈은 전도 냉각 설비에서 설계, 제작 및 실험 된다. 본 실험 연구를 통해 히터의 활성화로 인한 차폐 전류 유도 자기장 감소가 포착되었으며, 이는 차폐 전류가 완화됨을 의미한다. 실험 결과는 최적 설계된 전기히터를 사용하여 차폐 전류를 실질적으로 억제할 수 있는지 그 타당성을 검증한다. 비선형 수치 분석 방법으로 실험 후 분석을 수행한다. 그 결과,

온도 구배와 차폐 전류 유도 자기장 감소 측면에서 분석과 측정 결과 간의 양호한 일치성이 확인되었다.

결론적으로, 본 논문은 핵자기공명 및 자기공명이미지 용 저온 초전도 자석의 유망한 대안인 고온 초전도 자석의 문제점을 정의하고 수치해석 및 실용기법 측면에서 솔루션을 제공한다. 수치 및 실험 연구는 솔루션의 유효성을 확인한다. 이 논문의 주요 기여는 다음과 같이 요약된다. 첫째, 수치 해석 방법은 차폐 전류를 “정확하게” 설명하기 위해 제안 및 시연되며 이 연구를 통해 선택된 차폐 전류 문제를 수치 방식으로 해결할 수 있을 것으로 기대 한다. 둘째, 열지우개는 고온 초전도 코일의 차폐 전류를 “실질적으로” 완화하기 위해 제안 및 시연되었으며, 이 연구를 통해 실용적인 방식으로 차폐 전류 문제를 해결할 수 있을 것으로 기대한다. 이 해결책들을 통해 수치 해석 방법과 실용적인 기술의 부족으로 인한 차폐 전류 문제를 해결 할 수 있을 것이다. 따라서 나는 이 논문이 더 높은 자기장 강도와 균일성을 탐구하는 길을 열어줄 것이라고 믿는다. 마지막으로, 이 논문이 차세대 핵자기공명 및 자기공명영상 응용기기를 위한 고자기장 고온 초전도 자석의 새로운 지평을 열 수 있기를 바란다.

주요어: 유한요소법(finite element method), 고온 초전도 자석(HTS magnet), 자기공명 응용기기(MR application), 수치 해석(numerical simulation), 최적 온도 제어(optimal temperature control), 차폐 전류(screening current)

학번: 2017-26332